Development of a Torsion Balance Facility and a search for Temporal Variations in the Newtonian Gravitational Constant.

by

Hasnain Panjwani

A thesis submitted to
The University of Birmingham
for the degree of
DOCTOR OF PHILOSOPHY

Astrophysics and Space Research Group
School of Physics and Astronomy
College of Engineering and Physical Sciences
The University of Birmingham
July 2012

UNIVERSITY OF
BIRMINGHAM

University of Birmingham Research Archive

e-theses repository

This unpublished thesis/dissertation is copyright of the author and/or third parties. The intellectual property rights of the author or third parties in respect of this work are as defined by The Copyright Designs and Patents Act 1988 or as modified by any successor legislation.

Any use made of information contained in this thesis/dissertation must be in accordance with that legislation and must be properly acknowledged. Further distribution or reproduction in any format is prohibited without the permission of the copyright holder.

Abstract

The torsion balance is one of the key pieces of apparatus used in experimental searches for weak forces. In the search for an understanding of a Unified Theory, physicists have suggested a number of signatures that are detectable in laboratory measurements.

This thesis describes the development of a new torsion balance facility, relocated from the BIPM (Bureau International des Poids et Mesures) [1], which has excellent environmental stability and benefits from a new compact interferometric readout for measuring angular motion which has been characterised and installed onto the torsion balance. The interferometer has sensitivities of 5×10^{-11} radians/$\sqrt{\text{Hz}}$ between 10^{-1} Hz and 10 Hz, an angular range of over $\pm 1^{\circ}$ and significantly reduces sensitivity to ground tilt. With the new facility the first experiment searching for temporal variations in the Newtonian gravitational constant has been undertaken with a null result for $\delta G/G_0$ for both sidereal and half sidereal signals at magnitudes greater than 5×10^{-6}. These results have been used to set an upper limit on some of the parameters within the Standard Model Extension framework [2].

The thesis also reports on the design and manufacture of prototype test masses with a high electron-spin density of approximately 10^{24} and negligible external magnetic field $\leq 10^{-4}$T. These test masses can be used within the facility to potentially make it sensitive enough to conduct future spin-coupling experiments.

Acknowledgements

In the name of God the Beneficial the Merciful.

Firstly I would like to thank Professor Clive. C. Speake for giving me the opportunity to undertake this work. His support throughout the project but specifically near the end when things were particularly difficult was much appreciated. I thank him for always giving me his time even when I randomly turned up outside his office. Secondly my thanks to Dr. Ludovico Carbone who I had the pleasure of working with for a couple of years. His knowledge of the apparatus and practicality when undertaking experimental measurements was an inspiration for me. I can't thank Ludovico enough for his continued support and guidance even after his time with this experiment, it will always be remembered. A big thanks also to Dr. Fabian Peña-Arellano who was greatly supportive during the time of the interferometer development. I thoroughly enjoyed working with him and hope our communication will continue into the future. It has also been a pleasure to work with some of the other colleagues within the group, Dr. Chris Collins, Dr Stuart Aston, Mr John Bryant and Mr Dave Hoyland all of whom have contributed to this work whether through discussions or helping with the apparatus. For his help and support during the many computer failures and for always trying his best to meet some of my difficult requests I must thank Mr Dave Stops, our computer systems manager.

Finally I cannot forget my parents who have always guided and supported me during this project and I would like to dedicate this thesis to them - thank you.

Contents

List of Figures

List of Tables

Chapter 1

Introduction

General Relativity (GR) and the Standard Model (SM) are two giants within modern physics. The strong, weak and electromagnetic interactions are described through the exchange of quantum particles while gravity is explained through the classical curvature of spacetime. Independently they have withstood a number of experimental tests. However attempts to combine both theories to explain all interactions have been unsuccessful. It is thought that both are low-energy limits of a more fundamental unified theory which is expected to merge the fundamental forces at the Planck scale, $m_p \approx 10^{19}$ GeV. Although experimentally verifying physics at these scales is currently out of our reach probing some of the low-energy signatures of candidate theories are possible.

This thesis describes the development of an experimental facility benefiting from good environmental stability and which can be used to search for some of the signatures associated with new theories of quantum gravity. The heart of the apparatus is a torsion balance, a device which has been used in a variety of scientific endeavours [10] since its first construction in 1777 and is described in chapter 2. Torsion balances, if well balanced, can be free from serious seismic interference and, due to its orthogonal relationship, the signal of interest is decoupled from the Earth's gravitational force. This makes it very sensitive in detecting small perturbations occurring from new non-Newtonian physics or Lorentz violating effects. In recent years the apparatus has been used in tests of the equivalence

principle, short-range tests of the gravitational inverse-square law and searches for new types of interacting particles [11]. Some of the theoretical motivations for using a torsion balance are described later in this chapter.

Chapter 3 and Chapter 4 outline two novel additions to the apparatus. The first is the development of a test mass containing a large number of aligned electrons. This test mass can be used to probe some of the spin dependent effects predicted by new theories and potentially make the facility sensitive to set new limits on these forces. The second is a new interferometer to measure angles with an immunity to the orthogonal tilt. The interferometer has been assembled, characterised and installed into the facility and subsequently used when undertaking the first experimental campaign looking for temporal changes in the Newtonian gravitational constant.

1.1 Lorentz Violation and the SME

The combination of SM and GR currently provide a highly successful description of nature. However there are some situations where even these theories break down. Both are unable to describe phenomena at high energies such as just after the Big Bang while also not always being compatible. GR is a classical theory which does not describe quantum phenomena but it can be used to predict effects on short length scales, for example, predicting a singularity at the centre of a black hole. The SM is a quantum field theory which should therefore be able to accurately describe short distance physics. However it cannot, in its present form, explain these black hole singularities. It is therefore expected that a more fundamental theory exists incorporating a quantum description of gravity. Some of the more successful candidates are string theory and loop quantum gravity. In 1989 Kostelecký and Samuel [12, 13] showed that natural mechanisms for Lorentz symmetry breaking exist in unified theories at the Planck scale. Lorentz symmetry is a postulate

requiring experimental results to be independent of the orientation or boost velocity of the laboratory through space. This idea, that physics is the same for all observers, is the basis of GR and is a key feature of the Standard Model used to classify certain particles and their interaction within groups. These violations of Lorentz symmetry in the early Universe would manifest today as small relic background fields interacting with elementary particles causing them to have a preferred direction in space. In 1998 Colladay and Kostelecký [14] developed the Standard Model Extension (SME) which aimed to catalogue and predict observable signatures in various types of low-energy experiments. The SME includes all the predictions of the Standard Model and is also observer Lorentz invariant, which means that the laws of physics are the same for all inertial observers. However the SME is not invariant to particle Lorentz symmetry which describes the movement of particles with respect to a fixed inertial frame. This means that the physical properties of a particle, such as its energy and momentum, will change as the motion or spin orientation of the particle changes with respect to the background field. The SME provides a generic framework and formalism for the interpretation and comparison of various types of experiments. Various theoretical and experimental results so far have been published in the Lorentz and CPT violation data tables [15]. To date a large number of different tests have been carried out to search for leading order signals of Lorentz violation. Although there have been no signs of violation these tests have set stringent limits on the SME parameters. For example, in the neutron sector, Brown *et al.* [16] use a K-^{3}He co-magnetometer to look at neutron spin interactions with the background field setting a limit for the equatorial components of $|\tilde{b}^n_\perp| < 3.7 \times 10^{-33}$ GeV at the 68% confidence level. In the photon sector several tests have set limits through Michelson-Morley type experiments. Using a rotating cryogenic sapphire oscillator Hohensee *et al.* [17] have constrained $\tilde{\kappa}_{tr}$ with a precision of 7.4×10^{-9}. Torsion balances have also been used to set limits on parameters within the electron sector. Heckel *et al.* [6] used a novel spin pendulum to search for preferred frame interactions with electron spin. They set stringent limits on the $\tilde{b}$ and $\tilde{d}$ parameters of $\approx$

10^{-31} GeV and 10^{-27} GeV respectively.

1.2 Variation in the Newtonian Gravitational Constant

The SME also provides the framework for a large number of gravitational matter couplings in the presence of Lorentz violation. Kostelecký and Tasson [2] have outlined a general approach to the search for possible signals within a number of scenarios. In the laboratory these signals can take the form of a time variation of the Newtonian gravitational constant, G_N, for measurements of gravitational acceleration, or, time-varying differences in the coefficients associated with different matter when undertaking Weak EP tests. The original aim of our torsion balance apparatus was to conduct precision measurements of G_N which intrinsically lends itself to a search for these Lorentz violating effects. The Lagrangian in the SME includes the conventional Newtonian kinetic and potential terms along with corrections that depend on extra coefficients. In a laboratory the force acting in the z direction on a test particle is given by [2]

$$F_z = -m^T g \left[1 + \frac{2\alpha}{m^T}(\bar{a}^T_{eff})_{\hat{t}} + \frac{2\alpha}{m^S}(\bar{a}^S_{eff})_{\hat{t}}) + (\bar{c}^T)_{\hat{t}\hat{t}} + (\bar{c}^S) + \frac{3}{2}\bar{s}_{\hat{t}\hat{t}} + \frac{1}{2}\bar{z}_{\hat{t}\hat{z}}\right], \qquad (1.1)$$

where $\bar{a}^T_{eff}$ and $\bar{a}^S_{eff}$ are 4-vector coupling to the species of fermion with T and S being the test and sources masses respectively while m is their effective inertial mass. With our experimental apparatus we are only sensitive to the first two corrective terms [18].

The SME uses a standardised Sun-centred co-ordinate system [19]. For a laboratory fixed to the Earth the standard frame (t, x, y, z) is such that the x axis points south, the y axis points east and the z axis points vertically upwards. In the Sun-centred system ($T_\oplus$,X,Y,Z), the X axis points along the direction from the centre of the Earth towards the Sun at the vernal equinox and the Z axis is aligned with the rotation axis of the Earth. The time $T_\oplus$ is taken when the laboratory y axis coincides with the Sun-centred Y axis.

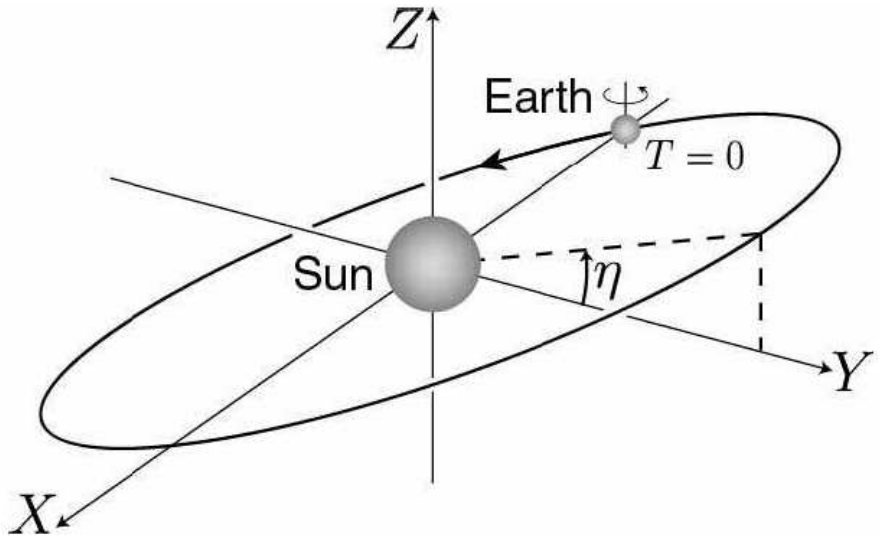

Figure 1.1: Sun-centred reference frame[3]

This introduces a phase shift, Φ, between t_0 of our experiment and $T_\oplus$ which must be taken into account in the analysis. A schematic of this reference frame is shown in figure 1.1. A transformation of equation 1.1 into this reference frame acts as a differential to the orbital position of the Earth around the sun and the position of the lab around the Earth.

$$\vec{\beta} = \beta_\oplus \begin{pmatrix} sin\Omega_\oplus T \\ -cos\eta cos\Omega_\oplus T \\ -sin\eta cos\Omega_\oplus T \end{pmatrix} + \beta_L \begin{pmatrix} -sin\omega_\oplus T_\oplus \\ cos\omega_\oplus T_\oplus \\ 0 \end{pmatrix}, \tag{1.2}$$

where $\Omega_\oplus$ and $\beta_\oplus$ are the angular frequency and speed of the Earth's orbital motion respectively. The Earth sidereal angular frequency is $\omega_\oplus$ while β_L is the speed of the laboratory due to the rotation of the Earth, $\approx r_\oplus \omega_\oplus sin\chi$ with χ being the co-latitude of the laboratory. Finally η is the angle between the XY celestial equatorial plane and the Earth's orbital plane which is $\approx 23.4°$. This transformation produces explicit dependencies on the rotational and orbital velocity of the Earth, leading to a sidereal and yearly bias,

δG in the measurement of the gravitational constant

$$\frac{\delta\vec{G}}{G} \simeq -2\alpha \left(\sum_w \frac{N_w^T \overline{a}_J^w}{M_T} + \sum_w \frac{N_w^S \overline{a}_J^w}{M_S} \right) \left(\vec{\beta} \right), \tag{1.3}$$

where N is the number of fermions and J refers to the spatial coordinates in the Sun-centred frame.

An initial run of our experiment has set the first experimental limits on these parameters [20, 21] and we hope modifications to the apparatus explained in this thesis will improve these results.

1.3 Tests with Polarised Electrons

The SME also provides mechanisms for the interaction between intrinsic electron spin and a Lorentz violating background field which breaks rotational symmetry. This potential is developed in the SME when taking the electron coupling terms in the non-relativistic limit appropriate for torsion-balance experiments as

$$V_e = -\vec{\sigma} \cdot \tilde{\vec{b}^e} \tag{1.4}$$

where σ is the spin of the electron and $\tilde{b^e}$ is the combination of CPT-even and CPT-odd parameters. Torsion balance experiments can be conducted through measuring sidereal torque perturbations on spin test masses. Recently measurements on this interaction have been carried out by Hou *et al.* [22] and Heckel *et al.* [6] with the most stringent limits on the strength of this interaction being set by the latter of 10^{-31} GeV.

There is also a large amount of theoretical work considering the role of spin in gravity, for a review see [23]. A number of experiments have therefore set out to probe some of these

interactions specifically in the electron sector, some of which use torsion balances. Moody and Wilczek [24] discuss the forces produced by the exchange of low-mass spin-0 particles and describe two spin-dependent interactions. Firstly a 'monopole-dipole' interaction between polarised electrons and an unpolarised atom

$$V(r) = \hbar(g_S g_P)\frac{\hat{\sigma}\cdot\hat{r}}{8\pi M_P}\left[\frac{1}{\lambda r}+\frac{1}{r^2}\right]e^{-r/\lambda}, \tag{1.5}$$

where λ is the range of interaction, $\sigma\hbar/2$ is the spin of the electron, g_P and g_S are the coupling constants at the polarised and unpolarised particles respectively, M_p is the mass of the polarised particle and r is the distance between interacting particles. Similarly a second 'dipole-dipole' interaction involving two sets of polarised electrons can be given by

$$\begin{aligned} V(r) = \frac{\hbar(g_P^1 g_P^2)}{16\pi M_P^1 M_P^2}\Bigg[&(\vec{\sigma_1}\cdot\vec{\sigma_2})\left(\frac{1}{\lambda r^2}+\frac{1}{r^3}+\frac{4}{3\pi}\partial^3 r\right) \\ &-(\vec{\sigma_1}\cdot\hat{r})(\vec{\sigma_2}\cdot\hat{r})\left(\frac{1}{\lambda^2 r}+\frac{3}{\lambda r^2}+\frac{3}{r^3}\delta^3 r\right)e^{-r/\lambda}\Bigg], \end{aligned} \tag{1.6}$$

where definitions are the same as before. Recently Dobrescu and Mocioiu [25] have classified the kinds of potentials that might arise from the exchange of low-mass bosons, constrained only by rotational and translational invariance. Experiments already conducted searching for these types of interactions include Ritter *et al.* in 1993 [26], Ni *et al.* in 1999 [27] and Heckel *et al.* in 2008 [6] who used traditional torsion balances while Hammond *et al.* in 2007/2008 modified the apparatus to use a superconducting levitating torsion balance setup [28, 29].

The experimental search for these spin dependent interactions in the electron sector was the motivation towards the development of a new spin-test mass as described in chapter 3.

Chapter 2

Experimental Apparatus

This chapter describes the torsion balance facility set up in order to undertake experimental campaigns and make precision measurements giving insights into some of the suggested theoretical signals. The heart of the facility is the torsion balance itself, particularly the use of a torsion strip which has been used and described in previous measurements. Here, we summarise the main advantages of this setup and the various other items of apparatus used to develop the whole experimental facility. The two main upgrades, the spin test masses and the angular sensor are discussed in detail in chapters 3 and 4 respectively.

2.1 The Torsion Balance

Although the torsion balance concept is now widely used in multiple disciplines with differing designs [10], the setup for this experiment has remained largely similar to the original design. A suspension, usually a round fibre or in this case a strip, is used to support a load and is extremely sensitive to lateral deflections, specifically its torsional mode. The equation of motion for a torsion pendulum can be given as

$$\tau(t) = I\ddot{\theta}(t) + \beta\dot{\theta}(t) + k\theta(t) \tag{2.1}$$

where $\tau(t)$ is an external torque, I is the pendulum moment of inertia, β is any viscous damping constant, k is the torsion constant of the suspension material and θ is the angle of deflection. Usually torsion balance experiments are conducted within a vacuum so as to minimise the gas damping β term, although there are still internal sources of dissipation[30, 31, 32, 33].

The internal dissipation in materials can be approximated as an extension of Hooke's law with a complex spring constant,

$$k_{new} = -k(1 + i\phi) \tag{2.2}$$

where ϕ is a lag term indicating that the response of the material will lag the torque applied. In many cases this lag is frequency independent [33, 34] and by comparing to a viscous effect can be given as the reciprocal of the quality factor, i.e. $\phi = 1/Q$.

We can define the pendulum's transfer function by converting equation 2.1 into the frequency domain

$$\tau(\omega) = \frac{\theta(\omega)}{H(\omega)} \tag{2.3}$$

with $H(\omega)$ being the transfer function given as

$$H(\omega) = (k(1 - (\omega/\omega_0)^2 + i/Q))^{-1} \tag{2.4}$$

where $\omega_0 = 2\pi f_0 = \sqrt{k/I}$ is the pendulum's resonance and Q is the mechanical quality factor. The maximum torque sensitivity of a pendulum is reached when limited by intrinsic thermal noise of the system. This limit can be derived by using the fluctuation dissipation theorem [30]

$$S_{\tau_{th}}^{1/2} = \sqrt{4k_B T \frac{k}{\omega Q}} \tag{2.5}$$

where k_B is the Boltzmann constant and T is the temperature. When designing a torsion pendulum the intrinsic thermal noise can be reduced by increasing the Q and reducing the stiffness, k. However, for example, it is not just a simple case of making the suspension thinner, thus reducing the stiffness, since this also reduces the suspendable load and subsequently the detectable signal. Ultimately the problem lies in the signal to noise ratio where various trade-offs must be considered depending on the type of experiment one wishes to undertake.

The apparatus and torsion pendulum design for this facility was originally developed by Quinn *et al.* for measurements of the gravitational constant, G [35, 36, 1]. The design is based on a torsion strip being the suspension system as opposed to the more common circular cross section fibre. The torsion strip was chosen for two major benefits with detailed descriptions given in [35, 36, 37]. The torsion constant of a strip with width b, thickness t and length L, where $L \gg b \gg t$ is given by

$$k_s = \frac{bt^3 F}{3L} + \frac{Mgb^2}{12L} \tag{2.6}$$

where F is the modulus of rigidity, M the loaded mass and g the local acceleration due to gravity. This is in contrast to the equation for a round fibre given by

$$k_w = \frac{\pi r^4 F}{2L} + \frac{Mgr^2}{2L} \tag{2.7}$$

where r is the radius of the wire. In wide, heavily loaded strips, the torsion constant is dominated by the gravitation term which is not a function of the strip's elastic properties and confirmed to be lossless [37]. This means, strips are not subject to significant anelastic

effects and its associated noise as circular fibres are and thus leads to a higher Q_{pend} of the system since

$$Q_{pend} = Q_{elast}\frac{k_{elast}}{k_{grav} + k_{elast}} \tag{2.8}$$

where subscript '*elast*' signifies the elastic contribution and '*grav*', the gravitational contribution [38]. Secondly the possible load on the strip is a function of its dimensions which can be adjusted such as to increase the load and thus any detection signal without the need to increase the stiffness in the same way as a round fibre. This benefit can be shown by comparing the signal to noise ratios of the strip and wire

$$\frac{sn_{strip}}{sn_{wire}} = \left(\frac{3}{2\pi}\frac{b}{t}\right)^{1/2} \tag{2.9}$$

which in the case of our current torsion strip is over a factor of 6 better. There is also a further benefit in that any experimental modulation can be done at a higher frequency, due to a higher pendulum resonance frequency, thus taking advantage of the lower noise. The increased stiffness does however mean a smaller deflection angle for any equivalent torque. Figure 2.1 shows the theoretical thermal noise angular sensitivity of the balance, obtained by using the transfer function to convert from torque to angle, and its current best sensitivity after carefully mounting the system and ensuring proper experimental conditions, for example; no ground loops, proper levelling of the table and stable vacuum pressure. Also plotted is the intrinsic limit of autocollimator, one of our optical sensors, obtained by placing a fixed mirror infront of the device. Clearly at higher frequencies we are limited by the optical readout and with further environmental control this may also be the case at lower frequencies. In order to therefore take advantage of the torsion strip setup and achieve an overall performance that is closer to the thermal noise limit a higher-resolution detector is required. This is one of the major drives to develop the

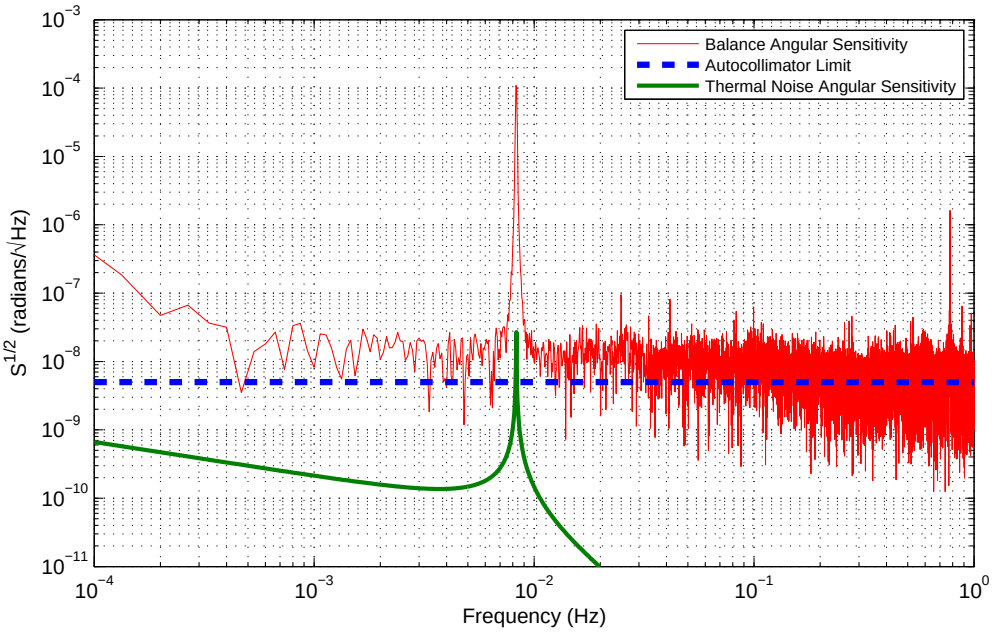

Figure 2.1: Current best angular sensitivity of the balance (red). Also shown (green) thermal noise limit autocollimator intrinsic limit (blue)

interferometric sensor described in chapter 4 with a higher sensitivity than the current optical readout.

Our strip dimensions are the same as that used in the experiment carried out in 2001 to measure the gravitational constant [1]. It is made from Cu-1.8%Be dispersion hardened alloy of thickness $t = 30\mu$m, width $b = 2.5$ mm and length L=160mm. It is loaded to about 80% of its yield strength and has a spring constant of k $\approx 2 \cdot 10^{-4}$Nm/rad, an oscillation period $T_0 \approx 120$s and a pendulum quality factor $Q_{pend} \approx 3 \cdot 10^5$. The strip's ends flare out to allow a large clamping surface area. This reduces losses associated with stick-slip motion between the strip and clamping blocks [37, 39]. At the bottom end the strip is clamped within a BeCu sleeve which is bolted onto an aluminium-alloy disk and a post upon which are mounted four circular mirrors. One of these mirrors is used for detection of the Autocollimator optical detector and one is for use with the Iliad interferometric sensor. The other two mirrors are in place for mechanical symmetry. Upon the disc sit

four 1.2kg Cu-0.7%Te test masses with their diameter of 55mm equal to their height. The top of the strip is clamped to a knife-edge support ensuring it hangs vertically and a magnetic damper system consisting of a copper plate resting in between two magnets which damps the simple pendulum modes of the balance. Some images of these features are shown in figure 2.2. This part of the apparatus is enclosed within a cylindrical vacuum vessel, 365mm in height and 344mm diameter. Outside the vacuum vessel a belt-driven carousel is used to hold up to four 12kg source masses. These source masses produce a maximum torque when rotated approximately $\pm 18.7^\circ$ from the zero torque position, i.e. radially aligned with the test masses. The torsion balance apparatus sits on an optical bench which is mounted with four legs on a granite slab. The granite slab is used for its large thermal time constant to attenuate any temperature fluctuations from the floor.

2.2 Experimental Procedure

To undertake the experiment searching for variations in the Newtonian gravitational constant two source masses were used on the carousel and driven by a stepper motor between positions of maximum torque every 800 seconds. To calibrate these positions the source masses were rotated around the balance in steps 1° with maximum torque equalling the position of maximum angular deflection, approximately $\pm 18.8^\circ$ from the null position as shown in figure 2.5.

2.3 Vacuum System

The torsion balance is covered by a cylindrical vacuum vessel which is connected through a glass adapter to an Edwards^{TM} nEXT240D turbomolecular pump. During the setup of the apparatus pressure spikes were detected indicating sharp leaks within the system. After assessing each flange within the system independently the problem was found to

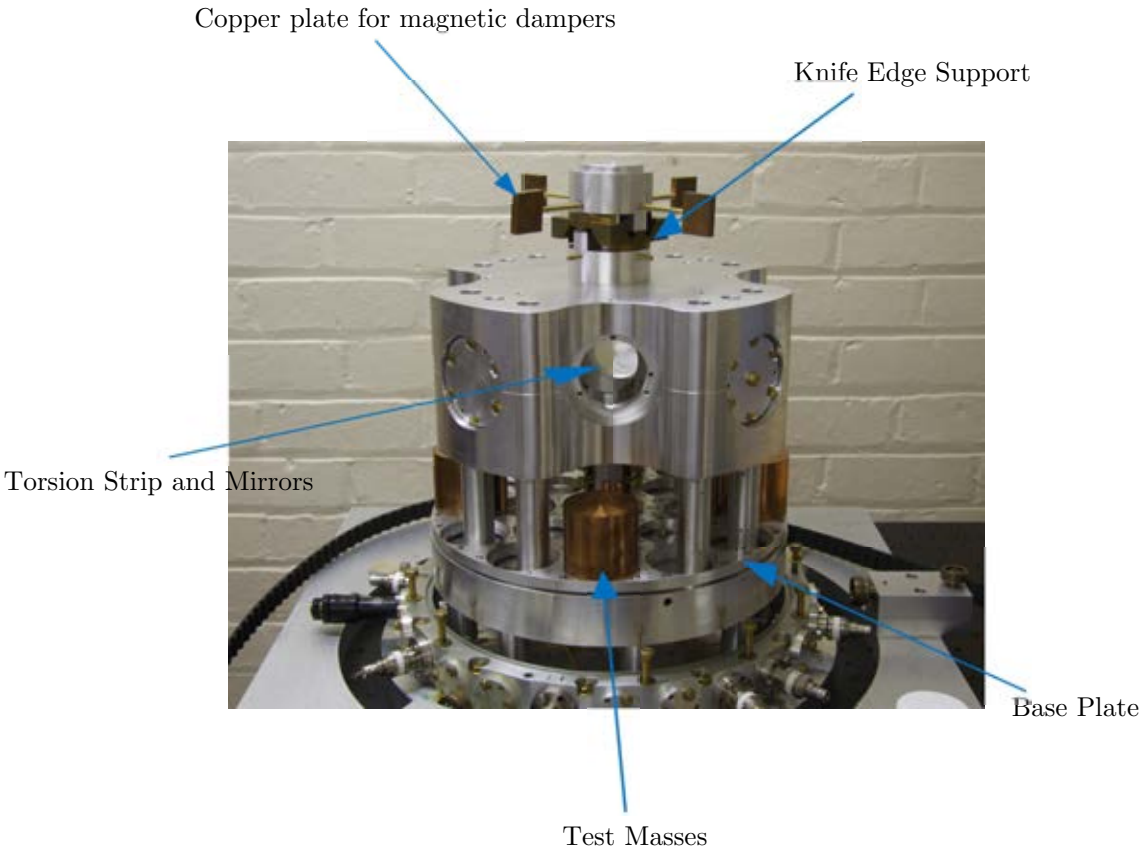

Figure 2.2: Image of core torsion balance apparatus.

Figure 2.3: Image of torsion strip before installation into the apparatus.

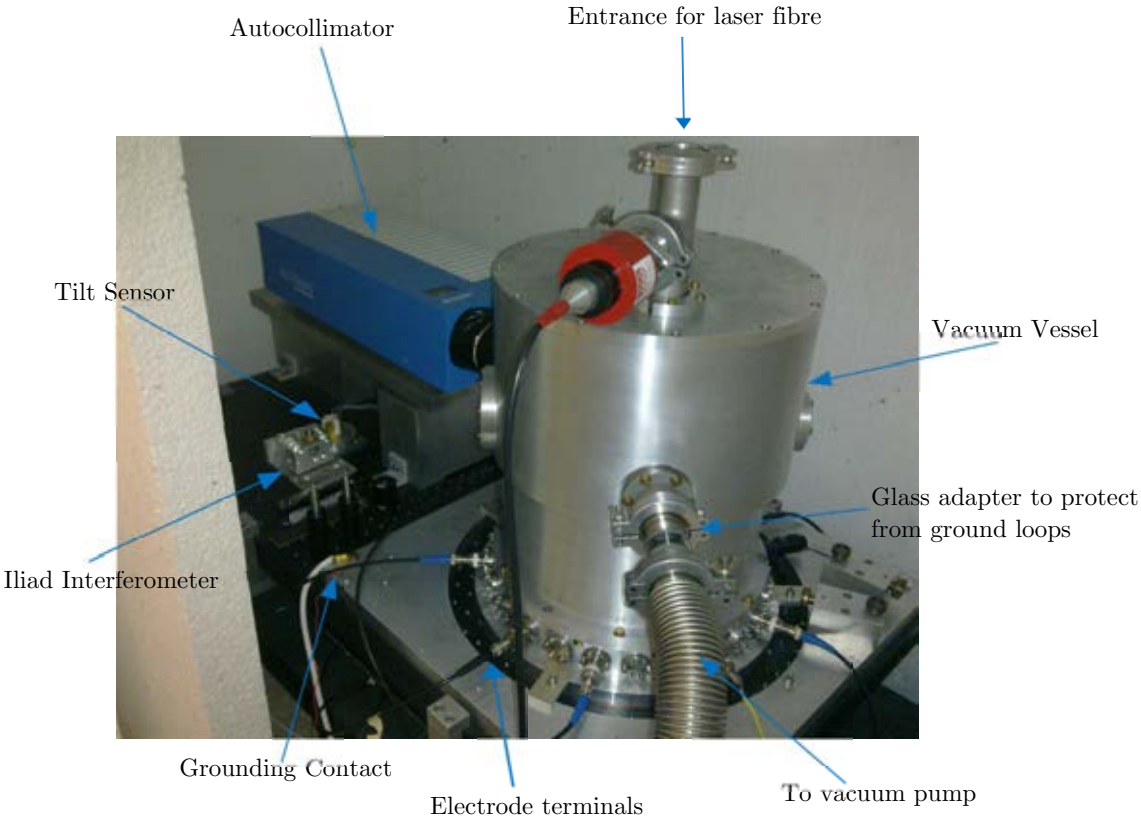

Figure 2.4: Image of Torsion Balance apparatus within the inner foam box. Iliad is currently not installed and on the bench top. Also not shown is the carousel which holds the external source masses and the motor which drives it.

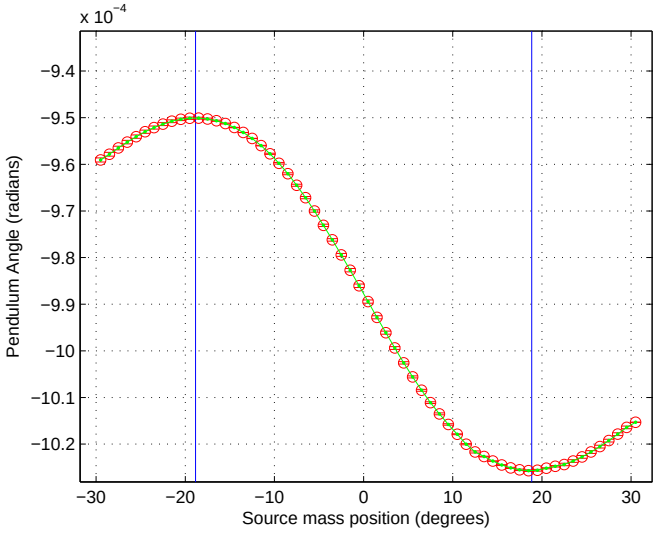

Figure 2.5: Source Mass position calibration showing the pendulum mean angle as a function of source mass position. The two blue lines signify the positions of maximum deflection, $\approx \pm 18.8^{\circ}$.

be from semi-dried vacuum grease, on a flange near the turbo pump, which encompassed small air pockets that seemed to be releasing intermittently. Subsequently each connection was thoroughly cleaned and no further vacuum grease used resulting in a stable pressure within the vessel of 6×10^{-6}mbar. A glass adapter is used to electrically isolate the pump from the apparatus to ensure both are grounded independently thus eliminating ground loops.

2.4 Optical Sensors

The experiment uses two optical sensors used to measure the pendulum motion. The original detector is an Elcomat HR Autocollimator[40]. This device is a calibrated state of the art optical sensor with measurement range of 1.4×10^{-3}radians and a measuring uncertainty of $\pm$ 1.45×10^{-7}radians. The autocollimator sits outside the vacuum vessel on a plate which is kinematically mounted on two aluminium blocks. Adjustment screws in the top mount are used to align the autocollimator with the torsion balance. A foam tube

encloses the air between the autocollimator and the vacuum vessel to reduce noise from air turbulence affecting the detection of the reflected LED light. On a static mirror the autocollimator has a sensitivity limit of $5 \times 10^{-9}\text{rad}/\sqrt{Hz}$ which corresponds to approximately $9 \times 10^{-13}\text{Nm}/\sqrt{Hz}$ when used with our torsion balance system. This is almost four times higher than the thermal noise of the balance. The size of the autocollimator also requires it to be mounted externally to the vacuum vessel and torsion balance setup. This makes it susceptible to differential motion, due to thermal and other effects, which may introduce noise into the data. For both these reasons a second optical readout has been developed and is described in detail in chapter 4.

2.5 Environmental Controls

For any precision measurement it is important to ensure the environment does not introduce sources of noise into the data. Periodic changes in parameters such as the temperature and tilt of the apparatus will be detected as a false signal from the torsion balance. For example a temperature oscillation may change the properties of the strip reducing or increasing its amplitude of deflection. If this temperature change happens at similar frequencies to the signal we are searching for, i.e. daily, it will be very difficult to decouple this environmental effect from any real one. This section describes some of the efforts taken to ensure that these disturbances are measured and minimised, especially on timescales associated with our signal.

2.5.1 Thermal Stability

The temperature is monitored by a number of PT100 resistance temperature detectors (RTD) placed at various points around the laboratory as listed in table 2.5.1. Temperature changes within the system may be detected by the readout originating from two effects.

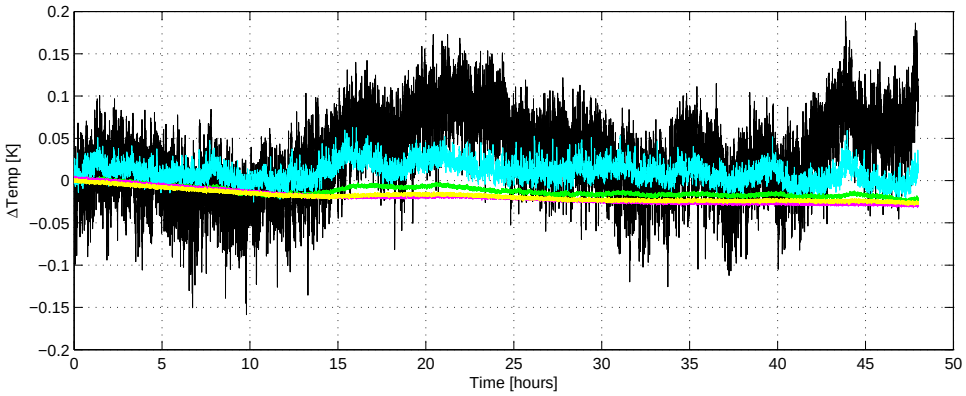

Figure 2.6: Temperature change of experiment over typical 50 hr timescale. Black: Air temperature of laboratory, Cyan: Air temperature of outer foam layer, Green: Air temperature of inner foam layer, Magenta: Temperature of butterfly piece inside vacuum, Yellow: Temperature of autocollimator mount.

An apparent motion will be seen due to a drift in the output caused by physical thermal changes, for example the expansion of the autocollimator mount mimicking a change in the torsion balance equilibrium angle. The other more subtle, but real, effect is due to changes to the properties of the torsion strip which may increase or decrease its deflection angle. To mitigate these effects the apparatus was enclosed in two layers of thermal shielding made of foam panels. A thermally stable water bath [41] pumps water through copper pipes welded to a large copper plate. This thermally controlled plate was initially designed to be heat-sunk to the optical bench to regulate its temperature. However it was found that mechanical noise from the flow of water coupled into the balance. The plate was thus placed onto the granite slab and used to radiatively regulate the air temperature within the inner thermal box. The stabilised water is also pumped in parallel to a heat exchanger located in between the inner and outer thermal boxes. Fans are used to pass the air through the heat exchanger and stabilise the air temperature of the outer box. This system results in an attenuation between any change in the room temperature and the inner box by a factor of almost 10 as shown in figure 2.6 where the temperature inside the vacuum vessel has not fluctuated by more than 0.03K. Over much longer periods we did not notice a change in the temperature of more than a peak-to-peak of 0.1K.

Number	Position	Standard Colour when plotted
1	Middle of optical table	Red
2	Front leg of table	Blue
3	Inner Box air	Green
4	Inside Vacuum	Magenta
5	Room air	Black
6	End leg of table	Orange
7	Copper pipes	Grey
8	Autocollimator stand	Yellow
9	Outer box air	Cyan

Table 2.1: Positions of 9 PT100 RTDs.

2.5.2 Tilt

An Applied Geomechanics 755 miniature tilt sensor mounted on the optical bench measures the tilt, in two orthogonal axis, of the experimental setup. We found that along the long axis of the optical bench there was a daily oscillation in the tilt signal. In the summer months the peak-to-peak oscillation was approximately 4μradian over 24 hours and approximately 1μradian in the winter months. This effect is most likely due to the heating and cooling of the building from the day/night cycles. To compensate for this daily variation which may mimic a gravitational signal a stack of piezo electric discs were fitted in between the optical bench and the granite slab. These piezos were driven by a PID controlled high voltage power supply which adjusted the supplied voltage depending on the tilt monitored by the tilt sensor. A schematic of the control loop is shown in figure 2.7. There are two stages to the control loop. Initially, to ensure the piezo stays within its operating range, the long term drift in the tilt is discarded by high-pass filtering. This is done, as shown in figure 2.8, by averaging over a 24 hour period and subtracting this from the original data. The filtered tilt readings are subsequently sent to the second stage, shown in figure 2.9. Here the input is compared to the setpoint, in our case zero, and the error logged in an integrator buffer. The time constant is given by the parameter T, set for 700 seconds, while the gain for conversion to voltage is given by K. Data from the

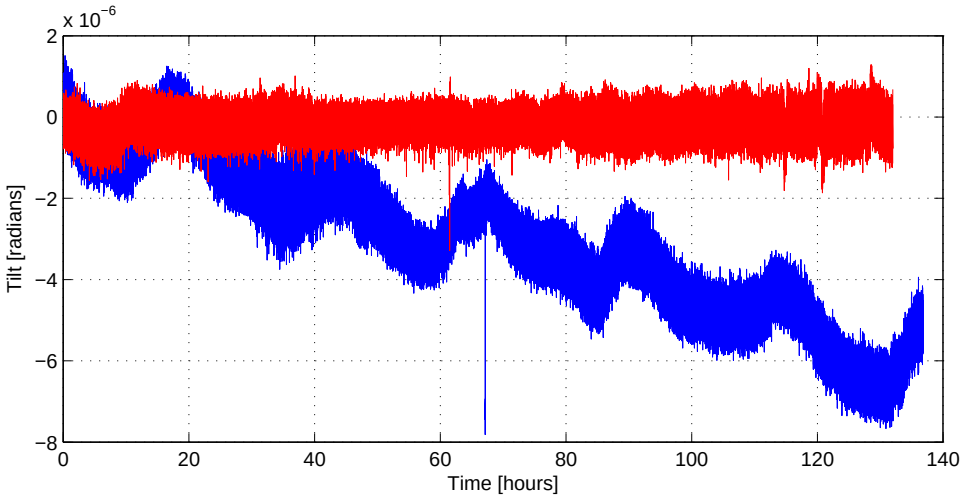

Figure 2.7: Tilt output before control (blue), after control (red)

tilt sensor over a few days is shown in figure 2.7 before and after the control loop was operational.

2.6 Data Acquisition

Three independent computers were used to run the experiment. One was dedicated to data acquisition where the autocollimator data through RS232, the tilt data through an internal 16 bit ADC card and the temperature data through a Keithley multimeter were logged. A separate computer was used to drive the motor which modulated the source masses and the third computer used to run the high voltage power supply for controlling the tilt. The new interferometer, Iliad, was logged through a self contained data acquisition module which converted from photodiode voltage to displacement output. This is explained in more detail in chapter 4. All computers used Labview routines which were interlinked through the network sharing a single time stamp and any other required data, for example the filtered tilt to be sent from the data taking computer to the piezo controlling computer.

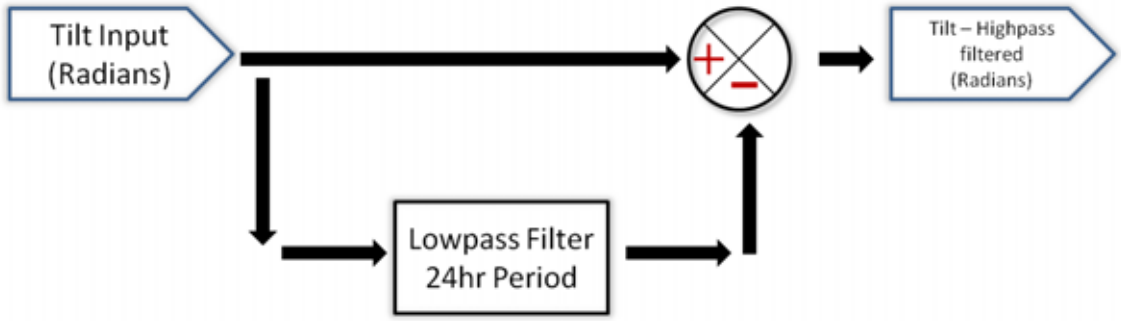

Figure 2.8: High Pass Filter.

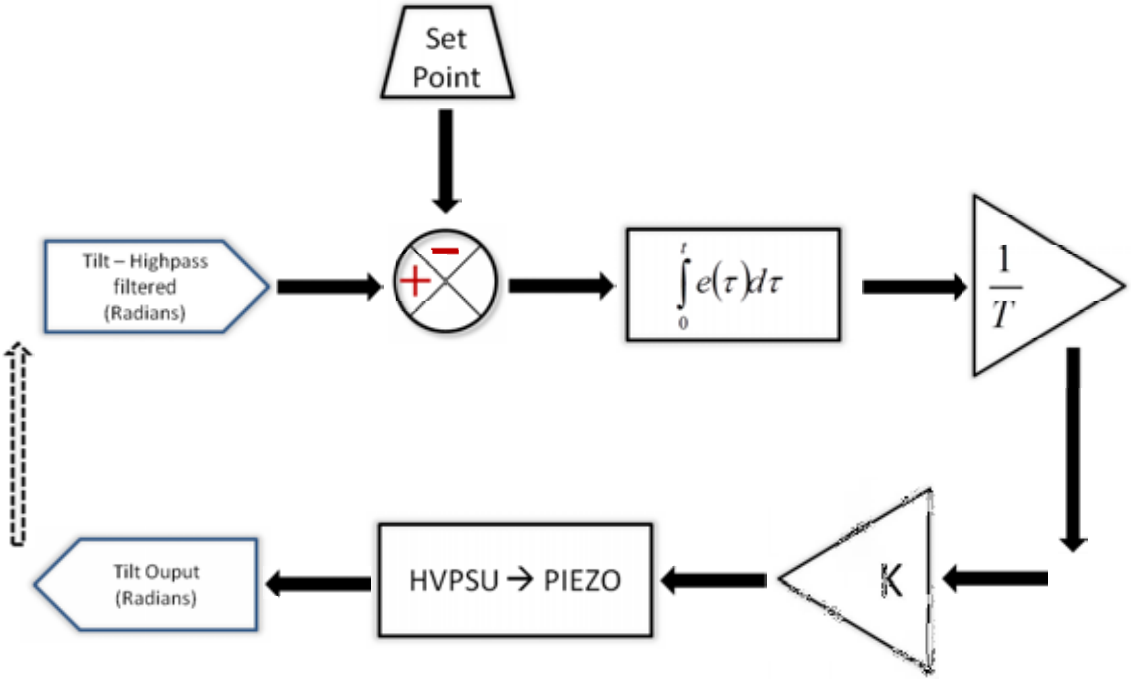

Figure 2.9: Integrator Control Loop.

Chapter 3

Spin Test Masses

One of the development upgrades required to enable sensitivity to interactions with electron spin, such as those described in chapter 1, is a test mass with a high number of polarised electrons giving a large macroscopic spin moment. This chapter describes the development, from design to manufacture, of a new concentric arrangement of permanent magnets with a high number of polarised electrons and low external magnetic moment specifically for use in high loading torsion balances like ours. We first give a summary of the required magnetic notation and then briefly describe other 'spin test mass' designs. This is followed by our theoretical framework and assessment of its validity by comparing simulations and experimental measurements. Finally we choose materials and dimensions for a real test mass and collaborate with a company to manufacture them.

3.1 Magnetism - A brief introduction

Previous experiments, some of which were described in chapter 1, have employed a number of designs to ensure the test masses have a large spin moment. The material used is always magnetic since this is the direct consequence of aligning spinning electrons. It would thus be prudent to summarise the key concepts involved in understanding the atomic origin of magnetic moments and how that will effect any test mass design.

A quantum mechanical treatment of atoms leads to information on the energy levels associated with the electrons that are characterised by four quantum numbers, n, l, m_l, m_s. The principal quantum number, n, determines the electron shell and defines its energy. The orbital angular momentum, l, describes the angular momentum of the orbital motion and equals $\hbar\sqrt{l(l+1)}$. The final two numbers describe the orbital angular momentum and spin angular momentum of one component of the total. According to the Pauli exclusion principle the states of two electrons are characterised by different sets of quantum number.

The magnetic moment of an individual electron from its angular momentum around the nucleus, μ_L, can be derived as the product of a circular current, I, around a closed area δA, $\vec{\mu_L} = I \cdot \delta\vec{A}$. The current is a function of electron velocity, v, and radius from the nucleus, r, such that $I = \frac{-ep \cdot r}{2m_e r^2}$. The moment is therefore

$$\vec{\mu_L} = \frac{-e}{2m_e}\vec{L}, \tag{3.1}$$

where e is the charge on an electron and m_e is the electron mass. The value $\frac{-e}{2m_e}\hbar$ is known as the Bohr magneton, the natural unit for electronic magnetism, μ_B. A constant can be defined called the gyromagnetic ratio

$$\gamma = \frac{e}{2m_e} = g_e\frac{\mu_B}{\hbar}, \tag{3.2}$$

where g_e is known as the Landé g-factor associated with the quantum nature of the electron. The gyromagnetic ratio defines the angular velocity for Larmour precession where the magnetic moment will precess around an homogeneous magnetic field as $\vec{\omega} = \gamma\vec{B}$. The moment in the z-component can therefore be written as

$$\mu_{lz} = -\gamma m_l\hbar = -g_l\mu_B m_l, \tag{3.3}$$

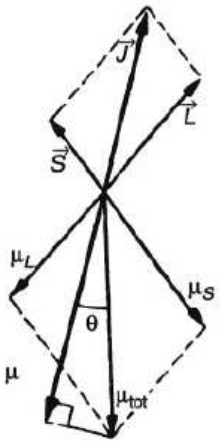

Figure 3.1: Spin-Orbit interaction vector model[4]

where the value m_l can take up to $(2l + 1)$ integral values. For the orbital moment the value of the g-factor is equivalent to 1. A further magnetic moment also exists and is associated with the intrinsic spin angular momentum of the electron with quantum number $m_s = \pm 1/2$.

$$\mu_{sz} = g_s \mu_B m_s \hbar. \tag{3.4}$$

The g-factor for spin, g_s, is approximately equal to 2 [42] and has been extensively measured. It is associated with the quantum nature of the electron and is predicted very accurately by quantum electrodynamics (QED). A vector model of this is shown in figure 3.1.

Both the orbital and spin motions of the electrons can be taken together to form a resultant total angular momentum vector. This type of coupling is known as the Russell-Saunders interaction and has been proved to be applicable to most magnetic atoms [43]

$$\vec{J} = \vec{L} + \vec{S}, \tag{3.5}$$

where the $\vec{L}$ and $\vec{S}$ are the total contributions from all electrons within an atom. Note that the contribution from the summation over a full shell is zero and only incomplete shells contribute to the moment. The vectors associated with orbital and spin angular momentum precess around the total $\vec{J}$ due to this interaction which leads to the corresponding magnetic moments to do the same. However since the spin moment has a g-factor approximately twice that of the orbital moment the total magnetic moment is not parallel to the total angular momentum vector. Since the precession frequency is usually quite high only the component of $\vec{\mu}_{tot}$ along $\vec{J}$ is observed while the others average to zero. This magnetic moment is therefore

$$\vec{\mu} = \vec{\mu}_{tot} \cos\theta = -g_j \mu_B J, \tag{3.6}$$

where g_j, the g-factor associated with the total moment, can be derived through the cosine rule as

$$g_j = 1 + \frac{J(J+1) + S(S+1) - L(L+1)}{2J(J+1)}. \tag{3.7}$$

A well known set of rules can be used to predict values of L, S and J for an atom in its ground state for which the number of free electrons are known. These are called Hund's rules formulated by Friedreich Hund in 1927 [5] and are given as

- First maximise S for the configuration.
- Then maximise L consistent with S.
- Finally couple L and S to form J. $J = L - S$ is the shell is less than half full, and $J = L + S$ if the shell is more than half full. When the shell is exactly half full, $L = 0$ and $J = S$.

The first rule is due to electrons wanting to be in the minimum energy state and thus avoid

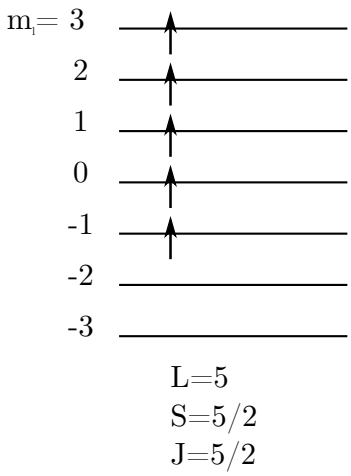

Figure 3.2: Application of Hund's rule to find the ground state multiplet of Sm^{3++} ion

each other. The best way to do this is to occupy different orbitals. The second rule means the electron orbits in the same sense whenever possible and the third rule is a consequence of the sign of the spin-orbit coupling. As an example we take a Samarium ion, an element which is used in some of the test mass designs. Sm^{3++} has an incomplete 4f shell with 5 free electrons (table 2.2.1 in [4]). The f shell determines the quantum number l=3 thus m_l can take 7 different levels. Schematically assign an electron to each level as per the first rule until the need to assign two electrons per level but in opposite spin as shown in figure 3.2. The value L is just given as the sum of m_l and thus $L = 5$, $S = 5/2$ and since the shell is not more than half full $J = L - S$ therefore $J = 5/2$. The spectroscopic notation for this is

$$^6H_{5/2} \tag{3.8}$$

Equations 3.6 and equation 3.7 can be used along with Hund's Rules to determine the ground state magnetic moment from various elements and estimate the spin content of a magnet. Although experimental results will be used to better describe the moment of various materials it is nevertheless a good starting point.

The interaction between many atoms in a solid gives rise to different magnetic effects. One of these effects is a persistent magnetic field which keeps an ordering within the materials' electrons. These materials are called permanent magnets and include iron, nickel, cobalt and alloys of rare-earth metals. We will briefly give here a description of the mechanism and established nomenclature associated with permanent magnets since they will be of use in the later sections.

A good description of the various types of modern permanent magnets can be found in [43, 44, 45]. Principal materials used today are AlNiCo (which are a family of ferromagnetic alloys composed mainly of Aluminium, Nickel and Cobalt), Ferrites, chemical compounds consisting of ceramic materials with iron(III) oxide (Fe_2O_3) as their principal component and rare-earth alloys mixing with cobalt or iron base. These permanent magnets are usually described by their hysteresis curves as shown in figure 3.3. When a permanent magnet is subjected to a large external field its domains, regions within a magnetic material where individual magnetic moments are aligned, will orientate such that they align with the field reaching point A on the curve. Once the external field is removed the magnet retains its own field called the remanence, B_r. The second quadrant of the loop is called the demagnetisation curve and describes normal operation of permanent magnets. A demagnetisation curve for bonded $Nd_2Fe_{14}B$ MPQ-14-12 is shown in figure 3.4. The blue line is the B-H curve while the green line is the M-H curve. In normal conditions the magnet sits somewhere along the curves known as its operating point. This point is the equilibrium between its own magnetic strength and the reverse field created by other parts of the magnet, thus it is a function of magnet shape. A thin disc would sit low down the curve due to the field from the outer edges reducing the field at the centre while a long thin magnet will sit higher up the slope. The magnetisation of the magnet, as given in the M-H curve, is calculated through the well known equation

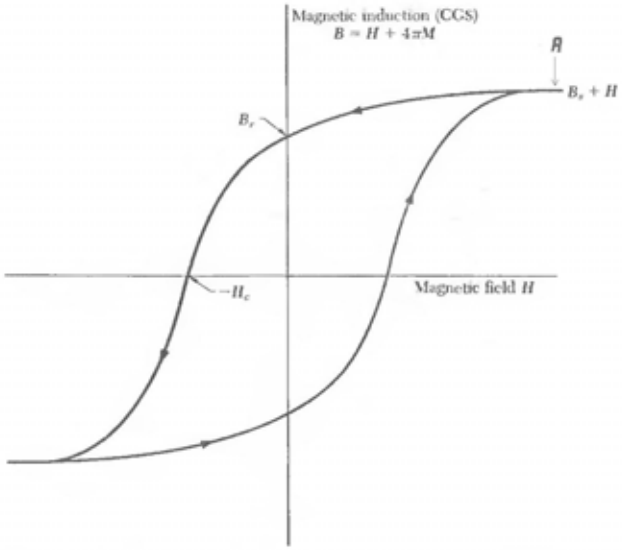

Figure 3.3: Typical permenant magnet hysteresis curve, image from [5]

$$\vec{B} = \mu_0(\vec{H} + \vec{M}). \tag{3.9}$$

The point the B-H curve crosses the x-axis is known as the coercivity of the magnet, the reverse field required to render its magnetic flux, B, to zero. However this is just a mere cancellation of the two fields and does not affect the internal magnetisation properties. The point the M-H curve crosses the x-axis is more important and is known as its intrinsic coercivity, H_{ci}. This is the reverse field necessary to intrinsically demagnetise the material after which it will not return to a previous state. The intrinsic coercivity is important when choosing a magnetic material as it will define the maximum field the outer magnet in our design can withstand and guides the choice of both internal and external magnet size.

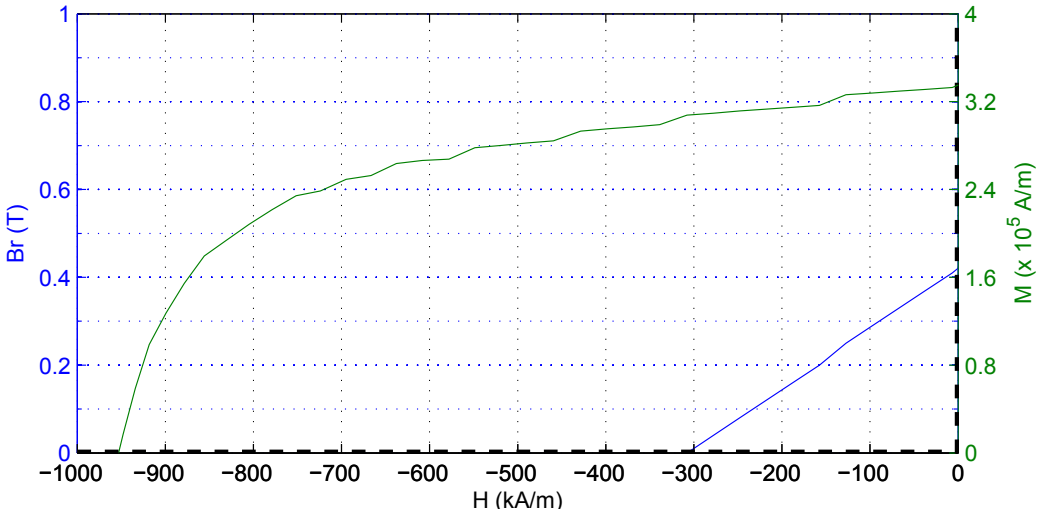

Figure 3.4: Demagnetisation curve for bonded $Nd_2Fe_{14}B$ MPQ-14-12. Data obtained from Magnequench [46]. Blue curve is the B-H while green curve is M-H.

3.2 Previous Test Mass Designs

In the late 1960s and 1980s Phillips [47, 48] searched for any spatial anisotropy which couples to intrinsic electron spin at room temperature and cryogenic temperatures respectively. His spin test mass was just a rectangular magnet embedded within a solenoid at room temperature and superconducting shielding at cryogenic temperatures to reduce the effects of magnetic fields. The next development was in the 1990s when Ritter and colleagues [26, 22], used Dysprosium Iron as the material for their test mass. At room temperature Dy-Fe compounds are ferrimagnetic. This is because the differing strengths of the exchange interactions in Dy and Fe causes different temperature dependencies on the effective ordering of the lattice. Thus at room temperature the magnetisations from Dy and Fe become equal and opposite cancelling out any magnetic moment. Dysprosium is a rare earth element with quantum numbers $L = 5$ and $S = -5/2$ where at room temperature approximately half the magnetisation comes from the orbitals and the other half from the spin. Most of the magnetisation in Iron comes from spin and therefore there is

a net spin moment. Their test mass was approximately 29g in mass and contained about 9×10^{22} spins.

More recently Heckel and collegues at the University of Washington [6, 49] undertook experiments using a spin test mass that used shape as a method of removing an external field. Their 107g mass consisted of a stack of 4 octagonal 'pucks' each of which was made of 8 trapezoidal magnets. In each puck 4 of the magnets were Alnico, while the other 4 were made of the rare-earth alloy $SmCo_5$. A schematic of the pendulum is shown in figure 3.5. This configuration placed the effective spin dipole at the centre of the pendulum and also mitigated other effects which may reduce the sensitivity of the experiment.

Alnico alloys are ferromagnetic and highly coercive, can with stand large opposing magnetic fields without losing their intrinsic magnetisation. Most of the magnetisation from Alnico occurs from the spin of the unpaired 3d electrons. In many ferromagnetic materials the orbital moment is usually small due to orbital quenching [5]. $SmCo_5$ is also a ferromagnetic composed of the rare-earth element Samarium and Cobalt, both of which have their own magnetic moments. Various experimental studies were used to estimate the contribution to the overall magnetic moment arising from orbital and spin components concluding in a total of approximately 9.6×10^{22} spins. This number was confirmed when they undertook a gyrocompass experiment with their spin pendulum which gave similar results.

Table 3.5.3 summarises these results along with our potential new design.

3.3 New Test Mass Design

To exploit the torsion strip apparatus which can hold up to 5kg of mass a new design of test mass was developed. This design published in 2009 [50] was based on two key concepts. A concentric assembly of permanent magnets to cancel out any macroscopic

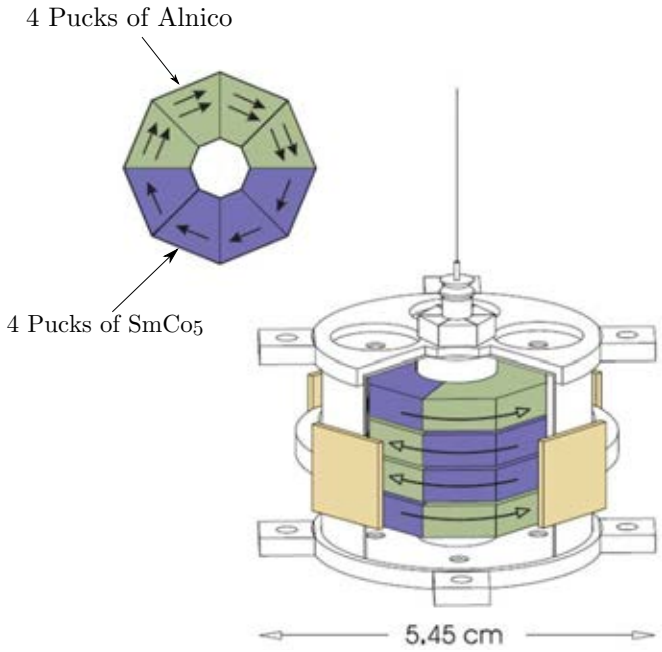

Figure 3.5: University of Washington spin pendulum [6]. Upper Left: top view of single 'puck', arrows signify the relative densities and direction of magnetisation. The net spin moment points to the right. Lower right: assembled pendulum of 4 pucks. Arrows show direction of **B** field.

magnetic moment and the use of different materials with varying ratios of orbital and spin contribution. This section will describe the steps undertaken to confirm such a design while the next section will explain the manufacturing process.

3.3.1 Test Mass Geometry

The need to neutralise any external magnetic field drove the idea of superposing two magnetic moments which are equal and opposite in direction. Physically this is possible by enclosing the magnets in a concentric assembly which can be designed using the multipole moment expansion method based on spherical harmonics [51, 52, 53].

The magnetic multipole expansion can be used to solve magnetostatic problems through the use of the scalar potential such that $\vec{H} = -\vec{\nabla}\Phi_M$. Where there is a fixed magnetisation, $\vec{M}$, this becomes $\nabla^2\Phi_M = -4\pi\rho_M$ with an effective charge density $\rho_M = -\vec{\nabla}\cdot\vec{M}$. For a permanent magnet with a magnetic discontinuity at its surface, application of the divergence theorem to ρ_M shows also an effective surface charge density $\sigma_M = \vec{n}\cdot\vec{M}$. The solution of the potential is then divided into a volume term and a surface term as

$$\Phi(\vec{r}) = -\int_V \frac{\vec{\nabla}'\cdot\vec{M}(\vec{r}')}{|\vec{r}-\vec{r}'|}dV + \oint_s \frac{\vec{M}(\vec{r})\cdot\vec{n}'(\vec{r}')}{|\vec{r}-\vec{r}'|}dS. \tag{3.10}$$

Here $\vec{M}$ is the magnetisation contained within volume V, S is the external surface of the volume, $\vec{n}$ is the normal vector to the surface and $\vec{r}'$ is within the magnetisation distribution. Whenever $\vec{\nabla}\cdot\vec{M} = 0$ the first term vanishes and only the surface integral remains. A permanent magnet can be described by a set of multipole moments m_{lm}, with the indexes l and m are functions of their geometry and magnetisation. For $|\vec{r}| > |\vec{r_0}| > |\vec{r}'|$, where $|\vec{r_0}|$ is the radius of the smallest sphere encompassing the whole magnetisation distribution and the origin, the term $|\vec{r}-\vec{r}'|^{-1}$ can be expanded using the addition theorem for spherical harmonics [51]. Here the scalar potential $\Phi(\vec{r})$ can be written as

$$\Phi(r,\theta,\phi) = \sum_{l=0}^{\infty} \sum_{m=-l}^{l} \frac{4\pi}{2l+1} m_{lm} \frac{Y_{lm}(\theta,\phi)}{r^{l+1}}, \tag{3.11}$$

where $Y_{lm}(\theta,\phi)$ is the spherical harmonic function of order l and m and (r,θ,ϕ) are spherical coordinates. The magnetic multipole moment m_{lm} of order l and m is defined as

$$m_{lm} = \oint_S (r')^l Y^*_{lm}(\theta',\phi') \vec{M} \cdot d\vec{S}. \tag{3.12}$$

The magnetic field in the surrounding space is derived from equation 3.11 through $\vec{B} = -\mu_0 \vec{\nabla}\Phi$ resulting in a linear combination of terms $\vec{B}_{lm} = -\mu_0 m_{lm} \vec{\nabla}(Y_{lm}(\theta,\phi) r^{-(l+1)})$ whose amplitude decays with distance as $r^{-(l+2)}$. Magnetic multipole moments are additive, so, by making the m_{lm} of the individual elements equal and opposite nulls the resulting magnetic field.

The multipole expansion is particularly appropriate for simple geometries for example the sphere and cylinder. The simplest nested geometry is that of a sphere contained within a concentric spherical shell, both with uniform magnetisation but in opposite direction. For such spheres and spherical shells the only non-vanishing moment is m_{10}, which is proportional to their respective volumes and magnetisations. Referring to the drawing in figure 3.6, a proper choice of materials and volumes such that $m_{10}(in) + m_{10}(out) = 0$. i.e.

$$M_0 R_0^3 - M_2 \left[R_2^3 - (R_0 + d)^3 \right] = 0, \tag{3.13}$$

allows the overall magnetic moment of the test mass to be zero leading to the magnetic field vanishing in the outer regions. Another configuration, while slightly more complex to describe mathematically but easier to manufacture, are concentric cylinders. A solid

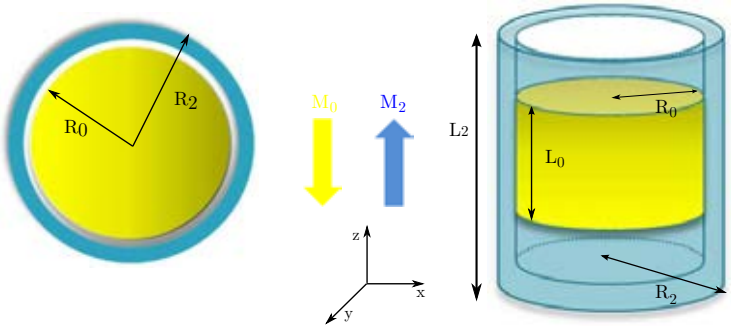

Figure 3.6: Left: Nested arrangement of a uniformly magnetised sphere within a spherical shell. Right: nested arrangement of two cylinders. In both drawings, M is the magnitude of the magnetisation, R is the radius to outer edge of sphere/cylinder, L is the height of the cylinder. Subscript 0 relates to the inner magnet while subscript 2 is for the outer one. There is a gap d between the inner and outer magnets for practical assembly reasons and to reduce the demagnetisation effects from the inner to outer magnet. We assume conventionally that the magnetisation of the inner magnet is negative while the one on the outer is positive, as shown by the two arrows.

cylinder nested inside a hollow cylinder with their individual magnetisation in opposite directions. The only non-vanishing terms in the cylindrical configuration are an infinite number of l odd and $m = 0$ terms. It is however only algebraically possible to null the first two terms corresponding to m_{10} and m_{30} and while higher terms still exist their magnetic fields drop off as $r^{-7}, r^{-9} \ldots$. The first two terms can be cancelled through the equations

$$M_0 R_0^2 L_0 - M_2 (R_2^2 - (R_0 + d)^2) L_2 = 0 \tag{3.14}$$

$$M_0 R_0^2 L_0 (L_0^2 - 3R_0^2) - M_2 [R_2^2 L_2 (L_2^2 - 3R_2^2) - (R_0 + d)^2 L_2 (L_2^2 - 3(R_0 + d)^2)] = 0. \tag{3.15}$$

It is important to note that this method is limited and can only establish nominal values of dimensions to null the overall moment. The expansion is based on the mathematical assumption that within the magnet the magnetisation is uniform, i.e. $\vec{\nabla} \cdot \vec{M} = 0$, which in a realistic permanent magnet is clearly not true. Nevertheless the simplicity of the approach allows a nominal assessment of compensating dimensions and further calibration can be done through more complex analysis.

3.3.2 Magnetic Materials

There are two requirements that drive the choice of material to be used in a concentric test mass arrangement, a high net spin content and an ability to withstand large magnetic fields, or 'hardness'. Firstly in order to have a net spin moment the magnetisation of the two materials should develop from differing ratios of spin and orbital components. In the perfect scenario one material's magnetic moment should occur entirely from spin while the other entirely from orbitals. The second requirement however restricts the type of material to those with high coercivities. The coercivity is a measure of the ability of a magnet to withstand an opposing magnetic field. In any concentric assembly in which each magnet is oppositely aligned, their respective fields will interact with the other magnet. If the magnets have low coercivities these opposing fields will tend to assert a torque on the polarised electrons and thus demagnetise the magnet. The usefulness and accuracy of the multipole expansion will then start to diminish. We have chosen rare-earth magnets as the basis of the design since they satisfy both these requirements. The well known and readily available rare-earth magnets of Samarium Cobalt, $SmCo_5$ and Neodymium Iron Boron, $Nd_2Fe_{14}B$, provided two of the best solutions. Both are permanent magnets and thus are intrinsically difficult to demagnetise. Secondly most of the magnetic moment in the $Nd_2Fe_{14}B$ comes from the spin in Fe_{14} while the $SmCo_5$ owes most of its magnetisation to the spin and orbitals in the Co_5. Further analysis of the specific magnetic content of each of these materials will be discussed in a subsequent section.

3.4 Magnetostatic Analysis

The feasibility study of the design described in the previous section was undertaken in two parts. Firstly a suitable finite element analysis software was chosen and its effectiveness checked against measurements of real magnets. Secondly a test cylindrical assembly was

Type	R_{in}[mm]	R_{out}[mm]	L[mm]	Grade	B_r[T]	$H_c \left[10^3 \frac{\mathrm{A}}{\mathrm{m}}\right]$	Supplier
Solid	-	5.0	10.0	N42	1.30	836	[55]
Hollow	5.2	10.1	10.9	N33	1.15	915	[56]

Table 3.1: General properties of the cylindrical magnets used for testing experimentally the nested cylinder configuration.

defined and manufactured to assess the accuracy of the method. The results of both these studies led to a design and manufacture of our final test mass.

3.4.1 FEA Software and Preliminary Studies

For most of this study a simple 2-dimensional finite element analysis software called FEMM 4.2[54] was used. The FEMM software can solve problems in the planar and axis-symmetric domain and so is ideal for symmetric shapes likes spheres and cylinders. An assessment of the accuracy of the software was done by purchasing two off the shelf $Nd_2Fe_{14}B$ magnets, one a hollow cylinder while the other a solid cylinder. The magnitude of the field in the z direction was measured for each magnet independently and in their nested configuration using a Hirst-GM04 Hall probe. The magnet properties, reported in table 3.4.1, were also inputted into FEMM and the coherent magnetic field results obtained.

Figure 3.7 shows the comparison of data collected from the measurements and FEMM. The results are in good agreement with differences of a few mT close to the magnet dropping to $<$ 1mT at greater distances. These discrepancies can easily be accounted for by non-homogeneous magnetisation of the real magnets and edge effects, differing properties from those inputted in FEMM and errors in the position of the hall probe. For example a 5% adjustment on the input remanence can cause a change in the field of a few mT close to the magnet while an error of 2mm in the position of the measuring Hall probe can also account for approximately 1-2mT uncertainty.

Several considerations can be inferred from these results. The agreement between measured individual fields of the magnets and the simulated ones show that the simulations provided realistic results. This is furthermore confirmed by the comparison between measured data of the nested cylinders. Finally, the fact that the measured field of the nested cylinders can be described as a bare sum of the individual magnet fields with very good approximation, as plotted in figure 3.8, shows that no relevant demagnetization occurred in the assembly process. The agreement between measurements and finite element analysis results proves the reliability of this study and the feasibility of further pursuing the spin test mass designs presented here.

Finally estimates can be made of the forces involved when assembling a nested configuration of magnets. As shown in figure 3.9 as a spherical magnet is moved closer to its required position it initially feels a repulsive force which switches to be attractive below approximately 13mm. As the second shell is brought closer it also is initially repelled but changes to being attracted with a final force of approximately 120N once in its final position. Within the spherical shell theoretically there is zero field however self demagnetisation effects show that the field is anti-aligned to the magnetisation direction. This means the inner sphere will naturally tend to align in an opposing sense to the outer shell which is a benefit during the final assembly.

3.4.2 Analysis of test compensated masses

The successful outcome of the preliminary investigation drove the design of a first set of compensated test masses. The $Nd_2Fe_{14}B$ magnets used in the previous study were off the shelf sintered magnets. Sintering is the process of creating a solid object by combining its powder through heat and pressure treatment. The initial NdFeB powder prepared from melted alloy is usually aligned via a magnetic field so that the easy axis of magnetisation of the particles are parallel and subsequently sintered at approximately 1200^oC [44]. This

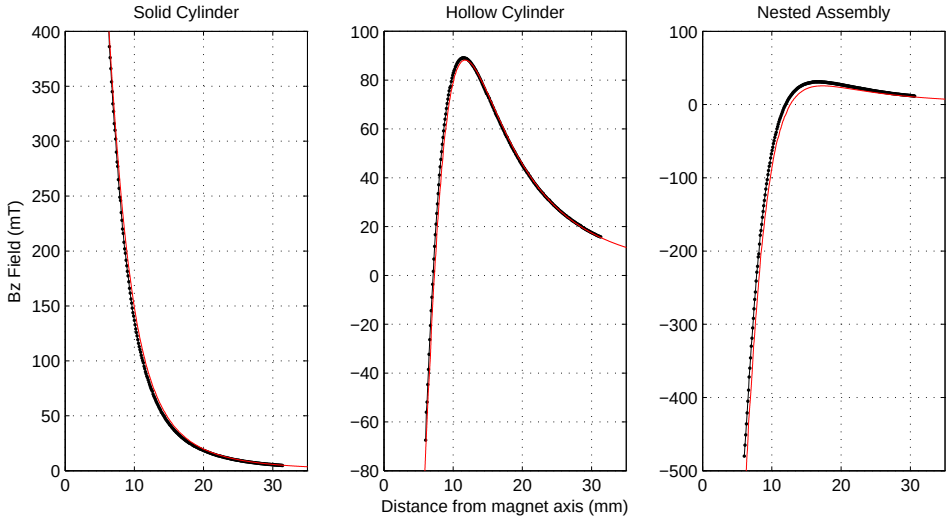

Figure 3.7: Field measurements in z direction (black dots) at varying distances along magnet symmetry axis compared with results from FEMM software (red)

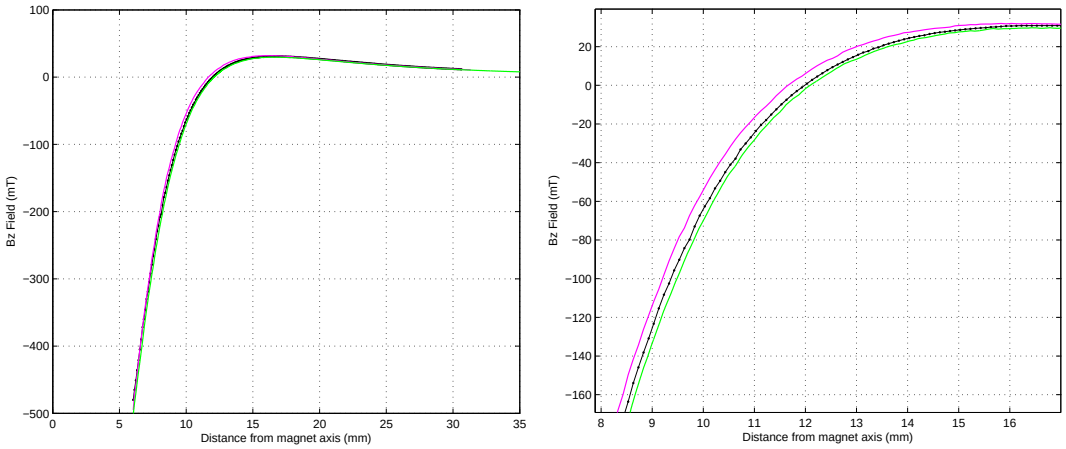

Figure 3.8: (Left)Field measurements in z direction (black dots) at varying distances along nested assembly symmetry axis compared with linear sum of individual field measurements (magenta) and FEMM estimates (green). (Right)Zoom in of previous plot at its knee.

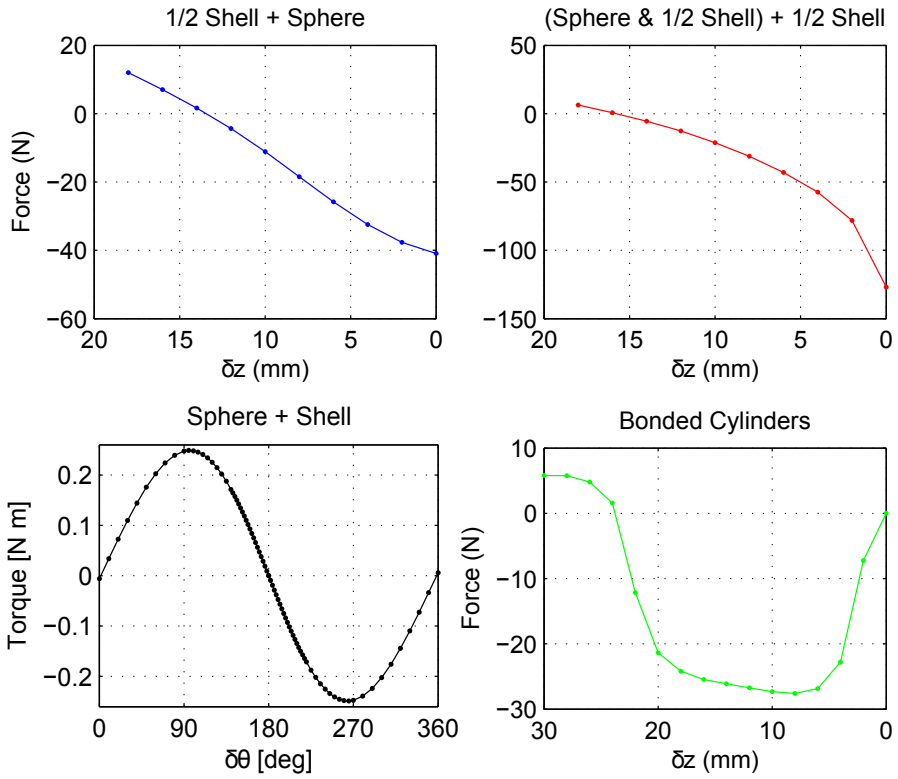

Figure 3.9: Plot of forces (as a function of axial distance between centres) and torques acting on the magnets. Top left: force acting on the solid inner sphere as it is brought towards the bottom hemisphere of the shell (final design dimensions). Top right: force on the top hemisphere as it is brought towards the assembled inner sphere + bottom hemisphere (final design dimensions). Bottom left: torque on the sphere, surrounded by the spherical shell, as function of the angle between the magnetic moments. (This data has been obtained using the software ANSYS$^{(\mathrm{TM})}$ [7] for a smaller compensated sphere than the final design). Bottom right: force on inner solid cylinder as it is brought towards hollow one (m_{10} bonded cylinder test dimensions.

Type	R_{in}[mm]	R_{out}[mm]	L[mm]	Grade	B_r[T]	$H_c\left[10^3\frac{\mathrm{A}}{\mathrm{m}}\right]$
$\mathrm{Solid}_{m_{10}}$	-	13.0	19.5	N10	0.68	440
$\mathrm{Hollow}_{m_{10}}$	13.2	17.5	25.0	N10	0.68	440
$\mathrm{Solid}_{m_{30}}$	-	10.0	12.5	N10	0.68	440
$\mathrm{Hollow}_{m_{30}}$	10.2	12.2	25.8	N10	0.68	440

Table 3.2: Dimensions of m_{10} and m_{30} compensated bonded magnets.

process allows the final magnet to be high in purity and thus have a high magnetisation however it also causes the magnet to be extremely brittle and difficult to machine. Since our study required specific dimensions of magnet to ensure compensation which are not readily available by off the shelf suppliers we purchased a number of cylindrical bonded, as opposed to sintered, NdFeB magnets from Magnet Applications Ltd. [57]. Bonded magnets use, as their name suggests, a resin to bind the particles together. Although this process makes it much easier to machine it also reduces the magnetisation since there are less particles per unit volume than in the sintered method. Ultimately for the final design, a trade off will have to be made depending on the complexity of design and thus machining requirements and the number of polarised electrons which is based on the magnetisation.

Two nested assemblies of the NdFeB magnets were machined. Initially, to determine the type of machining required, the outer magnet was kept to its original dimensions and only the m_{10} dipole moment matched for the inner and outer pieces as per equation 3.13. Since both magnets were of the same material this was equivalent to matching their volumes. The second set of magnets were matched for both their m_{10} and m_{30} moments as per equations 3.14 and 3.15. Table 3.4.2 includes the dimensions obtained from this moment matching process along with properties of the bonded magnet material.

Figure 3.11 once again confirms the reliability of the FEMM estimates. Using typical bonded NdFeB data from the manufacturer the FEMM results closely match the measured data to within a few mT. Simple adjustment of the material properties in FEMM by 5% can reduce the difference to within measurement errors.

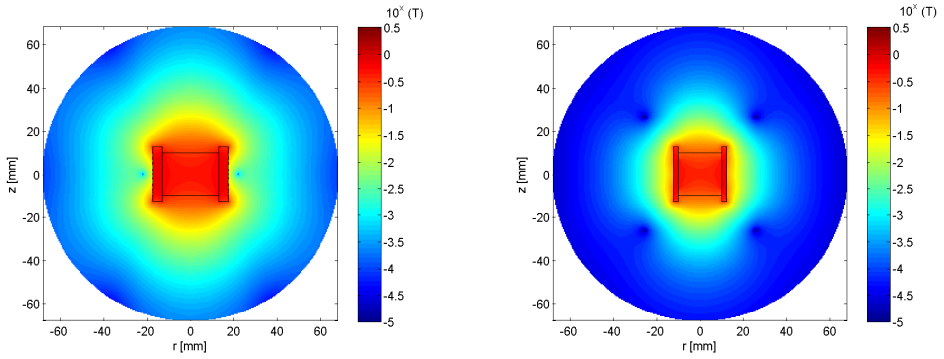

(a) m_{10} compensated assembly (b) m_{30} compensated assembly

Figure 3.10: FEMM estimates of B_z field around final test mass assembly. Colourmap is an order of magnitude value in units of Tesla.

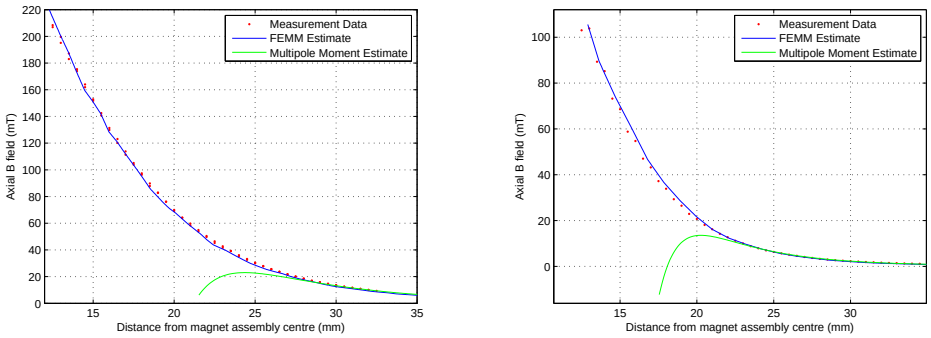

(a) m_{10} compensated assembly (b) m_{30} compensated assembly

Figure 3.11: Comparison of measurements and theoretical estimates from FEMM simulations and multipole moment expansion of axial B_z field.

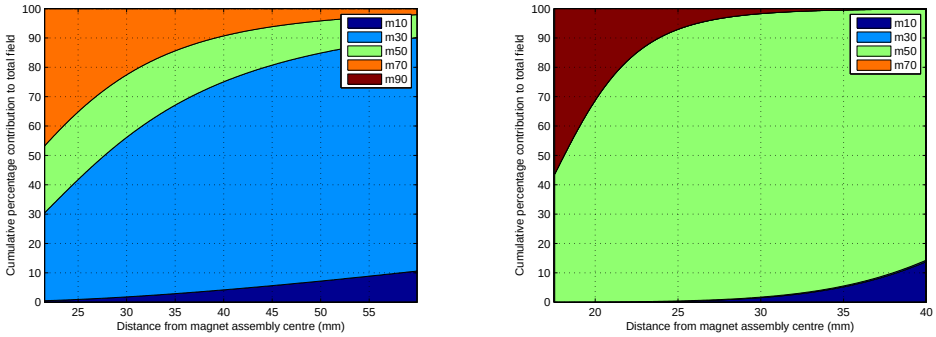

(a) m_{10} compensated assembly (b) m_{30} compensated assembly

Figure 3.12: Cumulative plot showing contribution of multipole moments to total axial B_z field.

Also plotted are the results obtained from using the multipole expansion approach to determine the field. It is however limited only to points outside sphere of convergence and as can be seen does not estimate correctly at distances close to this sphere. Figure 3.12 is a cumulative area plot showing the fraction of each multipole contribution to the total field. For the m_{10} and m_{30} the field from the first and first two terms respectively, as designed for, are very small confirming the success of this approach.

3.5 Final Design and manufacture

The investigation on smaller nested assemblies and the success of the methodology established the feasibility of a final design. Four major parameters guided this design;

- a higher spin per mass ratio than previous designs,
- a low net magnetic moment,
- dimensions which fitted within the current apparatus setup and
- a choice of materials that would allow for known machining techniques.

The first decision taken was to make use of spheres instead of cylinders due to their simpler magnetic moment makeup, theoretically only having a dipole moment. Secondly our current gravitational test masses are being held within small cups, 55mm in diameter, machined into the base plate attached to the torsion strip. The plate contained 12 of these cups around its diameter however only 8 are free for use. The new spin test masses would replace the gravitational masses in these same cups and therefore the overall dimension of the spin test mass is constrained to <55mm.

The acceptable residual magnetic field is limited by eddy currents created in the surrounding vacuum vessel which will cause damping on the torsion balance. The Lorentz force on an electron with charge,e, moving through a magnetic field, B, with velocity, v is given

as $\vec{F} = e(\vec{v} \times \vec{B})$ inducing an effective current density in the metal $\vec{J} = \sigma(\vec{v} \times \vec{B})$, where σ is the metals electrical conductivity. Since the magnetic field is perpendicular to the velocity term this leads to a volume integral for the force which can be approximated to

$$F \approx (B^2 \sigma t A)v, \tag{3.16}$$

where t is the thickness of penetration of the magnetic field and A is the effective area. For an oscillating torsion pendulum the term inside the brackets is a velocity dependent damping term and can be related to the pendulum quality factor, $Q = I\omega_o/bR^2$, where I is the pendulum moment of inertia, ω_0, is its resonant angular frequency, R is the arm length to the test masses and b the damping term. For any damping to be smaller than our pendulum quality factor of $3{\times}10^5$ the magnetic field at the aluminium vessel, which is 4mm away from the edge of the test mass, should be

$$B \leq \frac{I\omega_0}{QR^2\sigma t A}, \tag{3.17}$$

which is approximately $1.7{\times}10^{-4}$ Tesla. Thus providing the test masses can be calibrated such that at 4mm away from its edge the field is less than this value we will not be limited by eddy current damping.

For the manufacture of the test masses we collaborated with Quadrant Magnetics[58] based in The United States and agreed the following steps in the manufacturing process:

1. The University of Birmingham (UofB) chooses and designs the diameter of the inner Samarium Cobalt sphere.

2. Quadrant-Kentucky (QM) purchases two large isostatically-pressed SmCo5 ingots.

3. Ship ingots to Quadrant-California (QT) for cutting into cubes.

4. Ship cubes to Maine for grinding into spheres.

5. Ship spheres to Indiana for identification of poles, magnetisation and measurement of magnetisation by Magnet Physiks-Indiana[9] (MPUSA).

6. MPUSA provides magnetisation-measurement data to UofB.

7. (QM) provide UofB with unit properties of the bonded NdFeB material that will be injection molded into hollow spheres.

8. UofB provides dimensions of the bonded NdFeB hollow spheres to QM.

9. Quadrant-China molds hollow 1/2 spheres.

10. Hollow 1/2 spheres are shipped to QM. QM magnetizes each sphere.

11. UofB sends spacers springs to QM.

12. QM assembles magnetized SmCo spheres, spacers and springs inside the bonded NdFeB shells.

13. QM ships the fully-magnetized assemblies to MPUSA.

14. MPUSA calibrates the assemblies $\approx 2\%$; until 0 total field is measured outside the assembly.

15. MPUSA ships calibrated assemblies to MP-Cologne. MP-Cologne maps the magnetic field with a Hall probe at distances of: 1, 2.5 and 4mm in the zone of interest as expressed by UofB. Each measurement will consist of a 360 degree rotation with approximately 1 degree rotation step at the equator of the sphere and 3 additional latitudes, 12 total scans per sphere.

16. MP-Cologne sends data and finished assemblies to UofB.

3.5.1 Material determination

The most important aspect was the selection of appropriate magnetic materials. The choice of material has an effect on three of the four initial design parameters thus making it a critical step in the design. A low grade $SmCo_5$ was chosen as the material for the inner sphere. Although other exotic materials [59, 60, 61] exist which have a larger contribution from their orbital moment the practicality of producing large enough quantities and subsequently machining this into a spherical shape was beyond the resources of this project. As for the outer spherical shell the difficulty in machining led to the choice of bonded Neodymium, similar to that used in the preliminary studies. Quadrant Magnetics guided us to a supplier of bonded Neodymium, Magnequench [46], who produce a number of different grades of bonded material. The powders are produced by a process known as melt spinning. Magnequench describe the process as follows; an ingot of RE-Fe-B alloy is first melted, then the molten metal is ejected under pressure from a nozzle onto the surface of a water cooled rotating metal wheel. The material solidifies into a thin metal ribbon which is approximately 35μm thick and 1-3 mm wide. By carefully controlling process variables such as the metal flow rate and speed of the rotating wheel, the quench rate (and hence microstructure) can be controlled to achieve optimum magnetic properties. The ribbon is collected and then milled into a platelet or flake-shaped metal powder, which is heat treated to obtain the desired magnetic properties. This rapid solidification results in a material which has an extremely fine (typically 30-50 nm) metallurgical grain structure. Because the consequent grain size is smaller than the critical size for a single magnetic domain, these materials are magnetically isotropic. To produce the magnets the powder is mixed with a binder, in our case PPS (PolyPhenylene Sulfide), and then injection moulded into the desired shape.

Since the final assembly will be calibrated by finely adjusting the magnetisation of the Neodymium shell it is better to use an isotropic powder. An anisotropic material has

most domains with similar coercivity pointed in the same direction. When the calibrating field is applied, there is only a small difference between demagnetising one domain and demagnetising a great number of domains and it can be very easy to over-shoot the desired magnetisation value. Isotropic magnets have different particles with many different easy directions of magnetisation. When the material is moulded, the flakes within the powder are pointed in all directions. Thus although isotropic materials are harder to magnetise and demagnetise to saturation they are easier to finely tune [62].

The second consideration in the choice of the outer magnet material is a high B_r and high intrinsic coercivity H_{ci}. The reason for a higher B_r is straightforward in that it is the product of a larger magnetic moment thus the possibility of a higher spin content. The intrinsic coercivity, as described before, gives the limit of reverse field intensity. The outer shell will be subjected to a reverse field from the inner sphere and a low coercivity will cause demagnetisation thus inducing higher order moments. Referring to figure 3.4 the maximum H field experienced on the bonded magnet by the $SmCo_5$ should be lower than the knee of its demagnetisation curve. At a distance of 3mm away from the inner sphere the H field from the inner sphere is 315kA/m in addition to the Neodymiums own demagnetising field of 282kA/m gives a total of approximately 600kA/m. The MQP-14-12 grade was selected for its relatively high B_r but more importantly the position of its knee in the M-H curve is a lot higher than this value of 600kA/m thus although there will be some demagnetisation in the outer shell it will be small. The properties of MQP-14-12 powder can be found in appendix A.

3.5.2 Dimension Design

The first step in the manufacturing process was to decide on a diameter for the inner $SmCo_5$ sphere. To reduce the effect of demagnetisation on the outer shell a 3mm gap was left between the inner sphere and the inner radius of the shell. This information along

with the magnetic properties was inputted into the multipole expansion method which provided a set of nominal dimensions. A radius of 17mm was determined to be the best size for the inner sphere giving a nominal overal assembly diameter of just under 55mm. The $SmCo_5$ sphere was subsequently machined and its overall magnetic moment measured through the use of Helmholtz coils and a fluxmeter at MPUSA. The $SmCo_5$ properties sheet and data from MPUSA can be found in appendix A. The measured value of the magnetic moment was 15.90 ± 0.32 Am^2 while the average moment determined through FEMM via integrating equation 3.9 over the FEMM estimates of B and H was 15.83 Am^2. This result confirms that the $SmCo_5$ sphere can be adequately described by FEMM using the properties obtained from the manufacturer data sheet.

The next phase was to determine the dimensions of the outer shell. Nominal results had already been obtained and any demagnetisation effects were taking into account in the calculation by iteratively increasing the radius of the NdFeB shell until the external field was cancelled. Figure 3.13(a) shows a plot of the field amplitude around the assembly with best dimensions to within 2 decimal places. Clearly the higher order moments induced due to demagnetisation can now be seen close to the assembly however at a distance of 10mm from the test mass the field is already $< 10^{-4}$T. When including a 1mm thick spherical mu-metal shield 2mm away from the edge of the test mass as shown in figure 3.13(b) the external field is much less than 10^{-7}T. This is below the residual field produced by objects within the apparatus for example brass screws and much lower than our eddy current damping limit.

Since there will be some tuning through the use of knock-down fields to finely demagnetise the outer NdFeB shell, the outer radius was increased by 0.13mm to compensate for any machining tolerances and allow more control over the calibration process. The final design dimensions and average magnetic properties are listed in table 3.5.2.

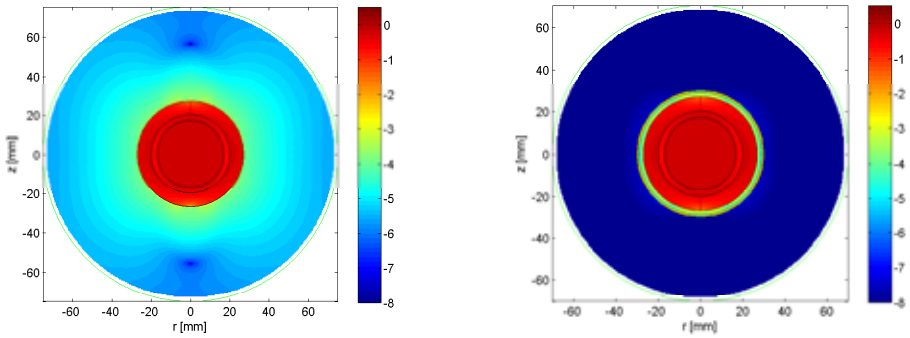

(a) No shield (b) Including a mu-metal shield

Figure 3.13: FEMM estimates of B_z field around final test mass assembly, Outer radius is 26.98mm. Colourmap is an order of magnitude value in units of Tesla.

Type	Grade	B_r[T]	$H_c \left[10^3 \frac{\mathrm{A}}{\mathrm{m}}\right]$
$SmCo_5$	22	0.970	762
$Nd_2Fe_{14}B$	MPQ-14-12	0.446	311

Table 3.3: Nominal magnetic properties of final test mass materials. In the FEMM designs a non-linear B-H profile was used.

Type	R_{in}[mm]	R_{out}[mm]	Density $\left[10^{-3} \frac{\mathrm{g}}{\mathrm{mm}^3}\right]$	Volume $[10^4 \mathrm{mm}^3]$	Mass[g]
$SmCo_5$	-	17.0	8.5	2.06	171
$Nd_2Fe_{14}B$	20.0	27.1	5	4.99	249

Table 3.4: Dimensions of final test mass design.

3.5.3 Spin Content

The final parameter to be discussed, however probably the most important in terms of scientific value, is the net spin density within these newly designed magnets. To successfully estimate the proportions of spin and orbit contribution to the overall magnetisation of each of the materials it will be required to assess previous experimental data on these materials. The net spin densities Σ can be estimated through

$$\Sigma = \frac{\alpha_{in}\mu_{in} + \alpha_{out}\mu_{out}}{\mu_B m_t}, \tag{3.18}$$

where m_t is the total mass, α is the spin contribution to the magnetic moment, μ, of each magnet, which can be estimated to good accuracy via FEMM and through measurements.

$SmCo_5$

RCo_5 materials, where R is a rare-earth element, were developed due to the complicated range of stoichometric compounds that are made when mixed with a transition metal, in this case Cobalt [44]. This interaction causes a strong magnetic anisotropy in both atoms thus giving a strong permanent magnetism. $SmCo_5$ has been extensively studied using a number of techniques including neutron scattering and nuclear magnetic resonance [63, 64, 65]. The crystal structure of $SmCo_5$, shown in figure 3.14, is that of $CaCu_5$ and the cobalt sites are separated into two sets of inequivalent atoms, 2 atoms in the 2c site and 3 atoms in the 3g site [8, 66, 67, 68]. Polarised neutron studies [66] have determined that the cobalt in YCo_5 exhibits large differences in the moment densities between the two localised crystallographic sites. This study determined that the Co_{2c} site has a localised moment of $1.77\mu_B$ while the Co_{3g} site has a moment of $1.72\mu_B$ with a spin proportion of 0.74 and 0.85 respectively. In a second study [65] reported for $SmCo_5$ the cobalt moments are shown to be $1.86\mu_B$ and $1.75\mu_B$ at the respective sites. As for the spin fraction,

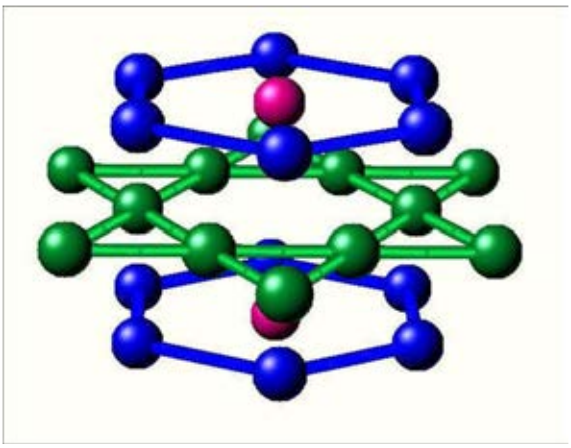

Figure 3.14: Crystal structure $SmCo_5$ (Image from [8]). Two layers of the Co(2c) site atoms (blue) sandwich the Co(3g) atoms (green). The Sm atoms lie in the middle of the hexagons (red)

measurements using nuclear magnetic resonance [69], investigated $CeCo_5$ for which there is negligible contribution from the rare-earth spins. Their results are close to the neutron study with the spin fraction being 0.76 and 0.90 at the two respective cobalt sites.

On the other hand Sm as a rare-earth with its 5 free electrons in the 4f energy level has a spectroscopic notation of $^6H_{5/2}$. Using Hund's rules one can determine its magnetic properties in its ground state as $0.72\mu_B$ total moment with μ_{spin} = -3.57μ_B and μ_{orbit} = $4.29\mu_B$. Experiments [64, 65] however have determined that the spin moment is considerably smaller due to a higher population in excited states at room temperature for Sm. Koizumi et al. [64] using X-ray magnetic Compton-profile measurements report 1:-0.23 $\pm$ 0.04 as the ratio of Co to Sm spin moments at room temperature while Givord et al.[65] have also found a value for the total moment of Sm^{3+} of $0.04\mu_B$ at 300K as opposed to $0.38\mu_B$ at 4.2K.

Since the results of measurements and various calculations are not conclusive we can use the same method, as done by [49, 6], of taking the central value between the experiments with error bars encompassing all sets. Thus for the cobalt we take a total moment of

$$\mu_{Tot}, Co = 2\mu(Co_i) + 3\mu(Co_{ii}) = (-8.97 \pm 0.10)\mu_B \tag{3.19}$$

$$\mu_S, Co = 2\mu_S(Co_i) + 3\mu_S(Co_{ii}) = (-7.14 \pm 0.39)\mu_B, \tag{3.20}$$

and for Samarium using the ratio determined by Koizumi [64] the spin moment would be

$$\mu_S, Sm = (-7.14 \pm 0.39) \times (-0.23 \pm 0.04) = (+1.64 \pm 0.37).. \tag{3.21}$$

Heckel [6] also makes a calculation of the Sm spin moment at room temperature as μ_S,Sm $= +3.56\mu_B$. We can once again take an average with error bars encompassing both values as

$$\mu_S, Sm(av) = +2.60 \pm 0.96\mu_B. \tag{3.22}$$

With this value the total spin fraction in $SmCo_5$ is estimated to be

$$\mu_{S\,frac}, SmCo_5 = \frac{\mu_S, SmCo_5}{\mu_{Tot}, SmCo_5} = \frac{(-7.14 + 2.6)}{(-8.97 + 0.04)} = 0.51 \pm 0.05. \tag{3.23}$$

$Nd_2Fe_{14}B$

There is a similar amount of literature detailing efforts on understanding the makeup and magnetic properties of $Nd_2Fe_{14}B$ as a whole and its constituents individually. However due to discrepancies in experimental data there is considerable doubt in the exact effects of exchange interactions between Nd and Fe at room temperature. Initially it was assumed that by studying Yttrium, which is non magnetic, in place of neodymium the Fe moment could be determined. Givord et al. [70] reports that at 4.2K the value of the spontaneous magnetisation of $Y_2Fe_{14}B$ corresponds to $2.10\mu_B$/Fe atom. On the other hand measurements by Tokuhara [71] determine a total magnetisation of $31.1\mu_B$/fu giving $2.22\mu_B$/Fe atom, very close to $2.20\mu_B$ measured in pure iron. Accordingly using this value in $Nd_2Fe_{14}B$ results in a Nd moment of $3.40\mu_B$/atom which is close to that of Nd^{3+} obtained from Hund's

rules but lower than $3.75\mu_B$ from Givords measurement. However Givord et al.[72] carried out a subsequent measurement using polarised neutrons and reports a $Nd_2Fe_{14}B$ moment at 4.2K of $37.90\mu_B$/fu with Nd contributing $2.20\mu_B$/atom, well below the ground state value [73]. This corresponds to an iron moment of $2.40\mu_B$. The study also measures a drop in the moment of $Y_2Fe_{14}B$ from $29.50\mu_B$/fu at 4.2K to $28.20\mu_B$/fu at 300K. This is in good agreement with Koon [74] who mentioned a similar 12% drop in the moment between the two temperatures. We can assume [75] that the relative variation in Fe for $Nd_2Fe_{14}B$ should be very similar and thus taking the Givord value of $Nd_2Fe_{14}B$ at 4.2K and removing the Nd moment gives $33.50\mu_B$ for the iron moment. A 12% reduction at room temperature results in an Fe moment of $2.11\mu_B$. The average moment of a number of room temperature measurements on $Nd_2Fe_{14}B$ [74, 76, 77, 78, 79] is $32.50\mu_B$ resulting in a 300K Nd moment of $1.55\mu_B$.

Finally we must assess the spin and orbital contribution to these moments. A small orbital moment has been reported for iron [80, 81] and we take here a conservative estimate of $0.1\mu_B$/Fe atom. We also assume [82] that the ratio of orbital and spin contribution to the total moment for Nd remains constant over the temperature range [75]. Since the spins in Nd are antiparallel to the Fe this gives a final spin ratio for $Nd_2Fe_{14}B$ of $\alpha_N = 0.79 \pm 0.04$ [1]. Table 3.5 summarises the results for both materials.

$$\mu_{Sfrac}, Nd_2Fe_{14}B = \frac{\mu_S, Nd_2Fe_{14}B}{\mu_{Tot}, Nd_2Fe_{14}B} = \frac{(28.00 - 2.34)}{(29.48 + 3.10)} = 0.79 \pm 0.04. \tag{3.24}$$

Total Spin Content

The total number of spins can be estimated by using the moment measurement of the $SmCo_5$ sphere of $15.90 \pm 0.32 Am^2$. In the perfect scenario the outer $Nd_2Fe_{14}B$ shell should

[1] We assign a 5% error to this result as reported in Garcia for experimental measurements

		$\mu_{\text{spin}}\,[\mu_B]$	$\mu_{\text{tot}}\,[\mu_B]$	Total Spin Fraction
$Nd_2Fe_{14}B$:	$\rightarrow Nd_2$	-2.34	+3.10	0.79±0.04
	$\rightarrow Fe_{14}$	+28.00	+29.40	
$SmCo_5$:	$\rightarrow Sm$	+2.60	+0.04	0.51±0.05
	$\rightarrow Co_5$	-7.14	-8.97	

Table 3.5: Summary of moment contributions for each material.

have the same moment but directed in the opposite sense. Thus using the fractions estimated in table 3.5 and equation 3.18 the number of spins are

$$\Sigma = \frac{0.79(15.90) - 0.51(15.90)}{\mu_B(420g)} = 9.80 \times 10^{23} spins/kg \tag{3.25}$$

	Reported Spins	Active Mass[kg]	Spins/kg
Ritter [26]	8.95×10^{22}	0.029	3.10×10^{24}
Heckel[6]	9.7×10^{22}	0.107	9.10×10^{23}
Bham	4.70×10^{24}	4.8	9.80×10^{23}

Table 3.6: Summary of spin content for different pendulum designs. Our torsion balance can hold up to 4.8kg thus reported is the upper limit.

3.5.4 Manufactured Prototype

At the time of writing the final prototype had not yet been assembled and calibrated however figure 3.15 shows a few pictures of the parts before assembly.

(a) Bonded NdFeB shells

(b) Bonded NdFeB shells

(c) SmCo inner sphere

(d) PEEK cup which holds the SmCo sphere within the NdFeB shell

Figure 3.15: Images of final test mass pieces.

Chapter 4

Iliad - Angle Interferometric Device

As discussed in chapter 2 the torsion strip balance can provide a better signal to noise ratio than round fibres due to its ability to hang a larger mass and the higher mechanical quality factor. However, in order to fully take advantage of these two features a sensor that is able to detect the smaller angular deflection produced for the equivalent torque from a round fibre is required. Our current readout, the autocollimator, has a sensitivity limit of $5 \times 10^{-9}\text{rad}/\sqrt{Hz}$ which corresponds to a torque of few $10^{-12}\text{Nm}/\sqrt{Hz}$ at $10^{-3}Hz$. This level makes it difficult for our experimental setup to be competitive with other experiments searching for weak interactions. For example the University of Washington spin coupling experiment achieved results equivalent to a torque of approximately 1×10^{-15}Nm at $10^{-3}Hz$ [1]. Another restriction of the Autocollimator is that due to its size it needs to be mounted externally on a large platform. This platform can be very susceptible to environmental factors like temperature which would shift the autocollimator position with respect to the Torsion Balance giving false signals. A small integrated readout device would improve the experimental facility greatly.

[1] Using values given in [6]

4.1 Basics of Optical Interferometry

Optical interferometers are widely used to measure displacements with high resolution and accuracy. In a standard Michelson interferometric configuration monochromatic light of wavelength λ, usually from a stable laser source, is sent through beam splitting optics which divide the beam into two arms of the interferometer, a reference arm and a measurement arm. The electromagnetic waves propagating in the two arms can be represented as

$$E_{ref} = A_1 \exp i(\omega t - \phi_1) \tag{4.1}$$

$$E_{meas} = A_2 \exp i(\omega t - \phi_2) \tag{4.2}$$

where A_n is the amplitude, ω is the angular frequency, t is the time and ϕ_n is the phase given by $2\pi/\lambda x_n$; $n = 1, 2$. The beams travel to their respective mirrors and reflect back to the splitting optics where they are recombined and detected as an interference pattern with intensity

$$I(\Delta\phi) = |(E_{ref} + E_{meas})|^2 = A_1 + A_2 + 2A_1A_2cos(\Delta\phi) \tag{4.3}$$

Here $\Delta\phi = 2\pi/\lambda\delta x$ with δx being the difference in path lengths travelled in each arm. It can be seen that $I(\Delta\phi)$ varies sinusoidally with ϕ and goes through a complete cycle (maximum - minimum - maximum) every time $\Delta\phi$ changes by 2π. Each one of these cycles is called a fringe and accurately counting fringes, or fractions of the fringe, can determine the distance displaced by the mirror. If Δl is the displacement of the measurement mirror, i.e. the difference in length between the two arms, then

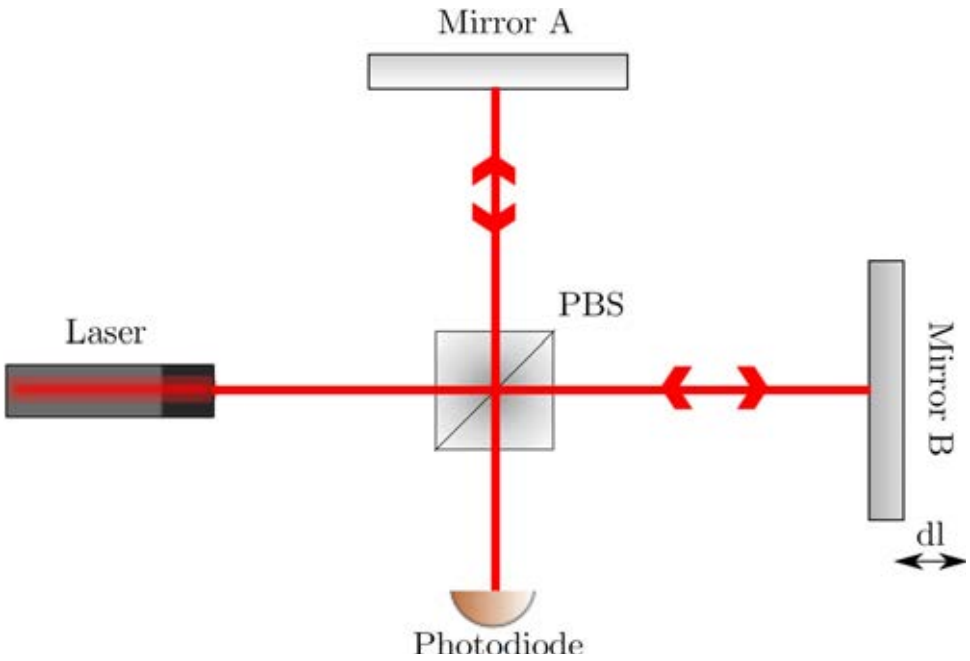

Figure 4.1: Michelson Interferometer Schematic

$$\Delta l = \frac{\lambda}{2} \times \frac{\Delta\phi}{2\pi} \tag{4.4}$$

since the beam travels Δl twice the phase change must be divided by 2. Figure 4.1 shows a simple schematic of the Michelson configuration. The limitation with using one interference pattern is that there is no way of reconstructing the direction of motion of the mirror, since the only information given at the output is either increasing intensity to a maximum or decreasing intensity to a minimum. This problem can be solved by using a second interferogram produced through a phase lag [83, 84]. Since both outputs are sinusoids of varying phase, plotting the two signals against each other produces an elliptical Lissajous pattern which, if the phase difference is exactly π forms a circle. This method is not immune to errors including differing DC offsets of the output intensities and errors from non-exact phase shifts[85].

4.2 Mirror Tilt Immunity and the Cat's Eye Retroreflector

For fringes to be detected the beams from each of the arms of the interferometer must be coaxial at the detector. In laser based interferometers this makes them very sensitive to misalignments both in the mirrors and the input beam angle. This narrow window of accuracy can be expanded through the use of retroreflectors which by definition reflect the light parallel to the incoming beam. Cube corners and cats eyes are two types of commonly used retroreflectors [86, 87, 88]. The cube corner has been extensively studied [86, 89, 90] and is the most commonly used retroreflector. However, when the polarisation state of light is important for the user, cube corners should be avoided since reflection on its internal faces can change the polarisation [91]. Peña-Arellano and Speake [92] introduce the idea of a double pass interferometer using a cat's eye retroreflector for mirror tilt immunity. They discuss how, through proper optimisation of the lens and mirror, a 'sweet plane' can be found for the target mirror which maximises its tilt immunity and minimises aberration errors.

4.3 ILIAD - Innovative Laser Interferometric Angular Device

The main disadvantage of using interferometers for quickly and easily measuring displacement is their sensitivity to misalignments [93]. Lengthy and precise techniques are usually required to adequately set up an interferometer to measure to the required precision while all this effort in ensuring alignment of the reflected beams can be easily compromised upon non-linear displacement of the target mirror. New challenges are posed when developing a device to measure angular rotation as opposed to displacement. Clearly, rotation of the target mirror causes a tilt in the reflected beam which affects sensitivity to interference. Furthermore, rotation of the target mirror will cause the interferometer beam to fall on

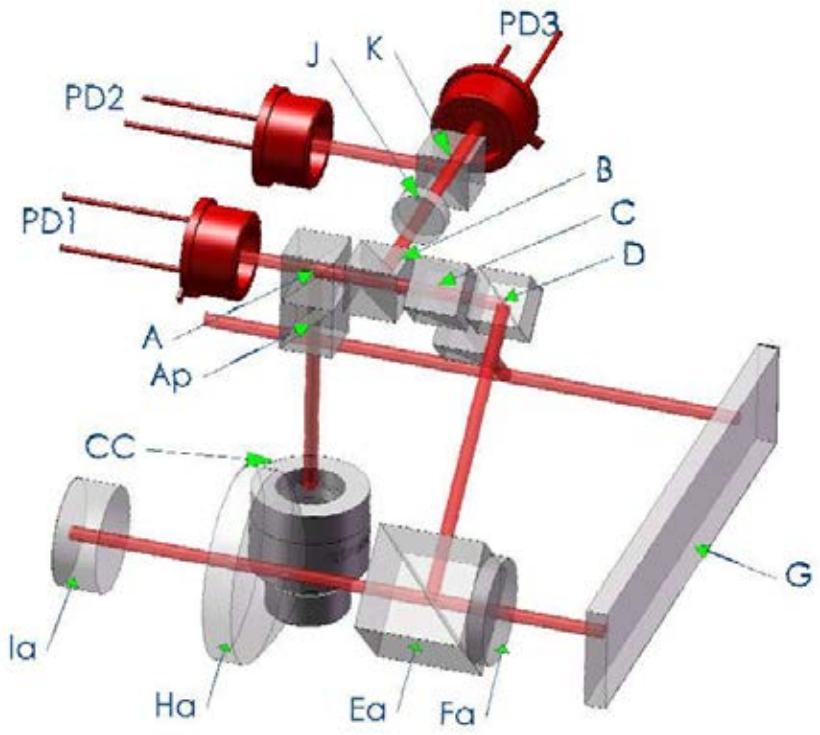

Figure 4.2: Iliad Optical Layout (The image is inverted to its operational orientation. The second arm of the layout has also been visually removed.)

slightly different parts of the mirror. Therefore, mirror flatness and associated errors must also be considered. These conditions contribute to the absence of a standard interferometric device to measure angular motion [94]. Iliad, the name given to our interferometer, is a device based on a linear displacement sensor by the name of Euclid [95] also developed at The University of Birmingham. Its optical configuration developed at The University of Birmingham uses the techniques described in the previous section to minimise errors and maximise tilt immunity [96, 94]. This is especially important when using the device for precision measurements in a torsion balance which maybe susceptible to oscillation modes other than the measurement one.

The optical configuration of Iliad is shown in figure 4.2. A DFB laser, A1905LMI [97],

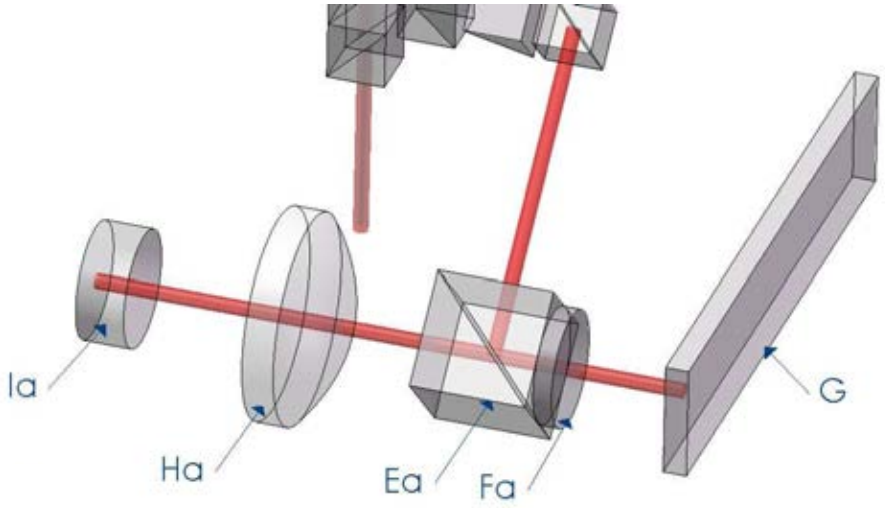

Figure 4.3: One arm of Iliad optical layout

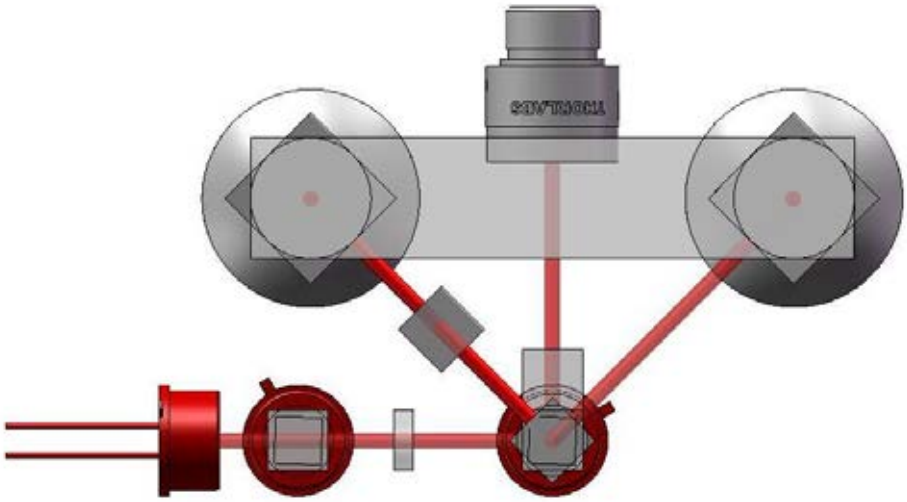

Figure 4.4: Iliad optical layout front

producing 1550nm wavelength light is sent through a pigtail fibre into an optical collimator (CC). This collimated beam enters the interferometer encountering two polarising beam splitters, Ap and A. The light whose electric field is parallel to the plane of incidence (P-polarisation) is transmitted and lost (not shown in the diagram), and the light whose electric field is perpendicular to the same plane (S-polarisation) is reflected into the rest of the interferometer. The next element in the path is non-polarising beam splitter B. This time the reflected beam is lost and the transmitted beam propagates further into two 45° polarising beam splitters which divide the light into the two arms of the interferometer. Polarising beam splitter C reflects the light whose electric field is oriented at $-45°$, with respect to the initial plane of incidence at A, into one of the arms, and transmits the remaining light whose field is at $+45°$ onto polarising beam splitter D. The latter component reflects the whole beam into the second arm and ideally no light is transmitted. Figure 4.3 shows a diagram of one of the arms of the interferometer. The light entering both arms are perpendicular to their respective planes of incidence and thus ideally all the light is then reflected at polarising beam splitter E towards the target mirror. On the way they pass through a $\frac{\lambda}{4}$ waveplate which converts their polarisation into circularly polarised light. The light is reflected off the target mirror and heads back through the quarter-wave plate which converts it back into linearly polarised light however this time parallel to their plane of incidence. This change of π in polarisation allows the light to propagate through the PBS, rather than reflecting as it did upon entering the arms, and encounter the cat's eye. The cat's eye reflects the beam back towards the target mirror at the same angle as its incident angle. This means the beam, once it has travelled twice through the quarter-wave, will reach the polarising beam splitter at the same angle with which it exited originally.

The two beams propagate back to the interfering optics where they recombine and the single beam is split twice, first at beam splitter B and secondly after going through a quarter-wave plate (J) at polarising beam splitter K. Photodiode PD_3 detects intensity

I_3, photodiode PD_2 detects I_1 and photodiode PD_1 detects I_2. This method of sensing three signals can be used to remove common fluctuations such as laser power drift and phase errors.

4.4 Experimental Realisation

A pair of threaded holes drilled either side of a large opening within the butterfly piece of the torsion balance apparatus guided the mechanical dimensions of the interferometer. This 50mm diameter opening faced one of the mirrors of the torsion balance at a distance of 59mm and provided the perfect position with which to fix the interferometer. The cat's eye was optimised by Peña-Arellano for this mirror distance and the mechanical holder was also designed to fit within these space constraints. Figures 4.5-4.8 shows some photos of the mechanical holder and an image of the real device aligned and mounted on the optical bench. The holder consisted of two main pieces, the front part which screwed directly onto the torsion balance butterfly piece, housed the two 45 degree beam splitters along with the arms of the interferometer. These components were placed in v-grooves with small markers indicating their optimum theoretical position. The rest of the optics were placed within a template fixed to a second piece that also held the photodiodes. Having two independent pieces allowed easy access to the main interfering optics which otherwise would be difficult to manipulate due to being directly under the cats-eye arms. Holes were drilled in several places to allow redundant light to escape rather than reflecting off the metallic surfaces and interfering with the output. The entire device measures 58mm x 54mm x 48mm and fits well onto the original torsion balance apparatus with no adjustments necessary. The mechanical holder, made of aluminium, was fabricated in our in-house workshop to standard 0.1mm tolerances.

Alignment of the interferometer was carried out in three main steps. Initially the optics

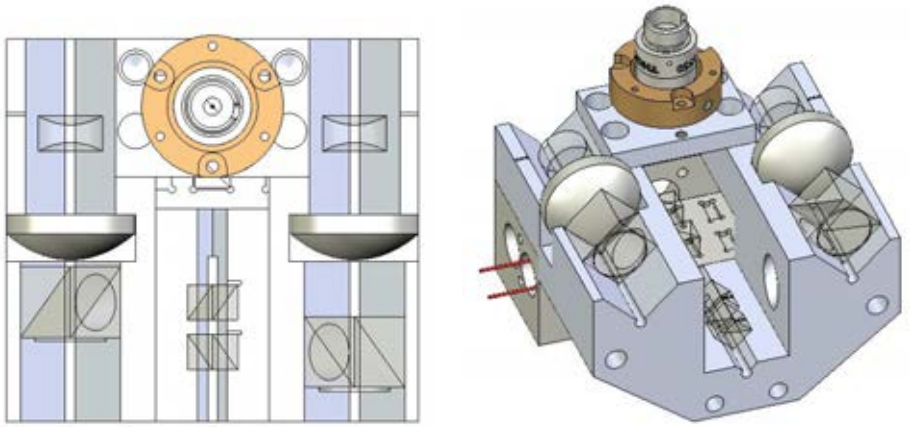

Figure 4.5: CAD images of Iliad assembly

(standard Thorlabs [98] components), excluding waveplate J, were placed with a small amount of Norland 65 [99] UV curing adhesive within the holder at their nominal positions, as shown by the machined markers on the mount. A critical part of the apparatus was the collimator which sat in a kinematically mounted ring. This allowed the incoming beam angle to be finely adjusted and along with small changes in the position of the 45 degree beam splitters the output beams exiting the arms at the top of the interferometer were made to be parallel. This was determined by using a visible 633nm He-Ne laser as the source and measuring the distance between the two beams exiting the arms at a position far from the interferometer. Once this was achieved the 1550nm infrared laser was re-attached. The second step was to place the test mirror at the sweet plane allowing the light to enter the cat's eye and again to finely adjust the positions of the cat's eye components until optimum interference was seen. This was determined when the visibility of the fringes $V = (I_{max} - I_{min})/(I_{max} + I_{min})$ was at a maximum. Finally the quarter waveplate was inserted and rotated to circularise Lissajous pattern before curing the adhesive and fixing the components. CAD drawings of the holder pieces can be found in Appendix B.

The interferometer produces three signals which vary sinusoidally with optical phase which can be modelled as

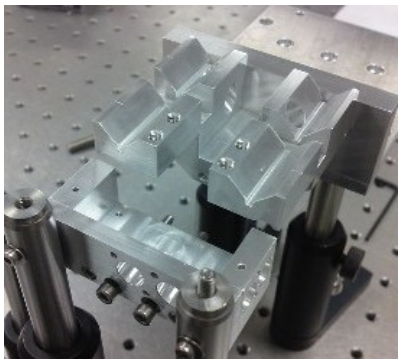

(a) Front and back parts

(b) Back part optical template

Figure 4.6: Photographs of machined mechanical holder pieces

$$I_1 = b_1 + a_1 \cos(\phi) \tag{4.5}$$

$$I_2 = b_2 + a_2 \sin(\phi) \tag{4.6}$$

$$I_3 = b_3 - a_3 \cos(\phi) \tag{4.7}$$

where ϕ is the optical phase, a_i and b_i represent the amplitude and offsets of the different signals. The signal at I_3 is 180° out of phase from I_1. Mathematically $I_1 + I_3 = c$, where c is a constant input intensity to the polarising beam splitter. For any interference pattern, if $I_1 = (c/2)(1 + \cos(\phi)$ then due to conservation of energy, $I_3 = (c/2)(1 - \cos(\phi)) = (c/2) + (c/2)\cos(\phi + \pi)$. These received signals are passed through a simple transimpedence amplifier stage converting the current output of the photodiodes into voltage detectable by a computer via an analogue-to-digital converter. The signals $I_1 - I_2$ and $I_3 - I_2$ are ideally in phase quadrature and, provided a suitable gain is applied to each photodiode such that $G_i a_i$ and $G_i b_i$ are equal, the outputs will form the co-ordinates of a point on a circle centred on the origin. As the optical path length changes, the point moves around the Lissajous pattern and the displacement can be calculated according to the formula

$$d = \frac{1}{4}\left(\frac{\lambda}{2\pi}\right) \arctan\left(\frac{x_1 y_2 - x_2 y_1}{x_1 x_2 + y_1 y_2}\right) \tag{4.8}$$

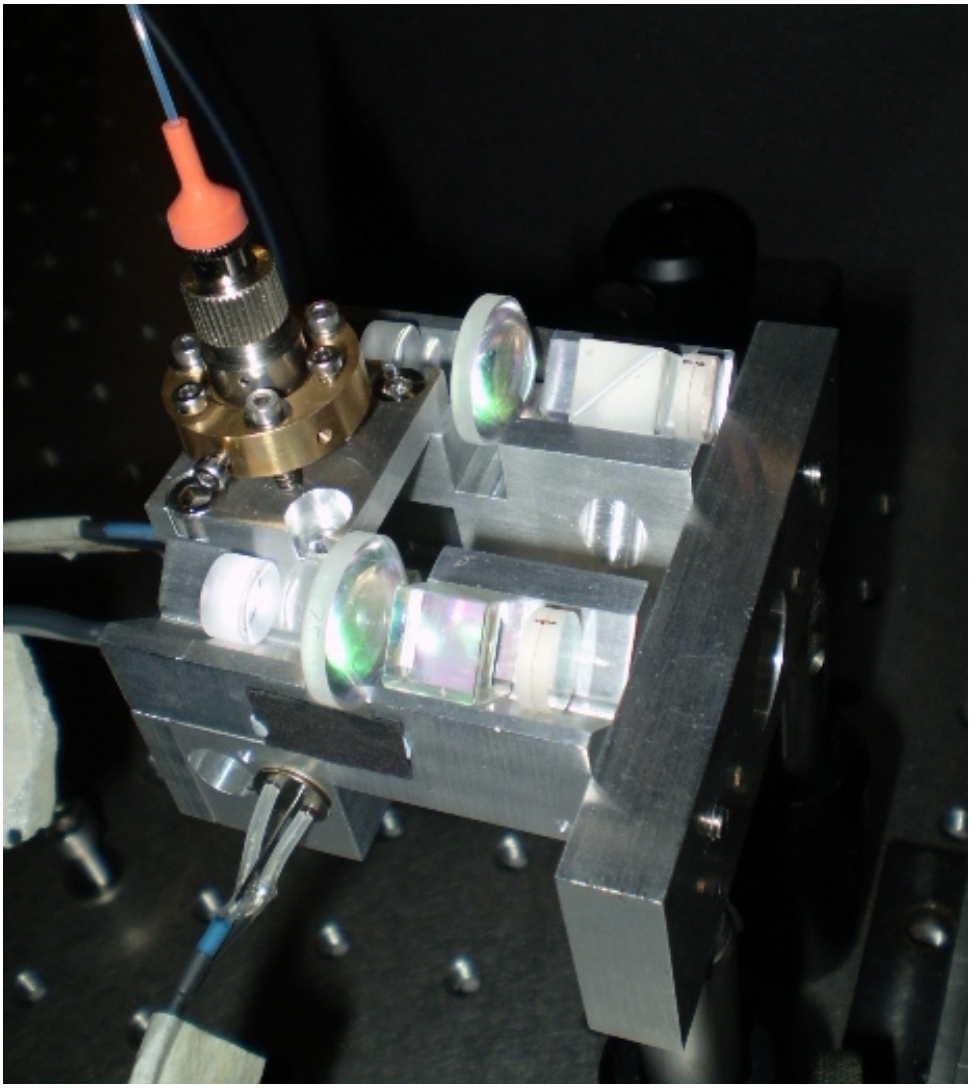

Figure 4.7: Image of aligned device on bench top during performance tests.

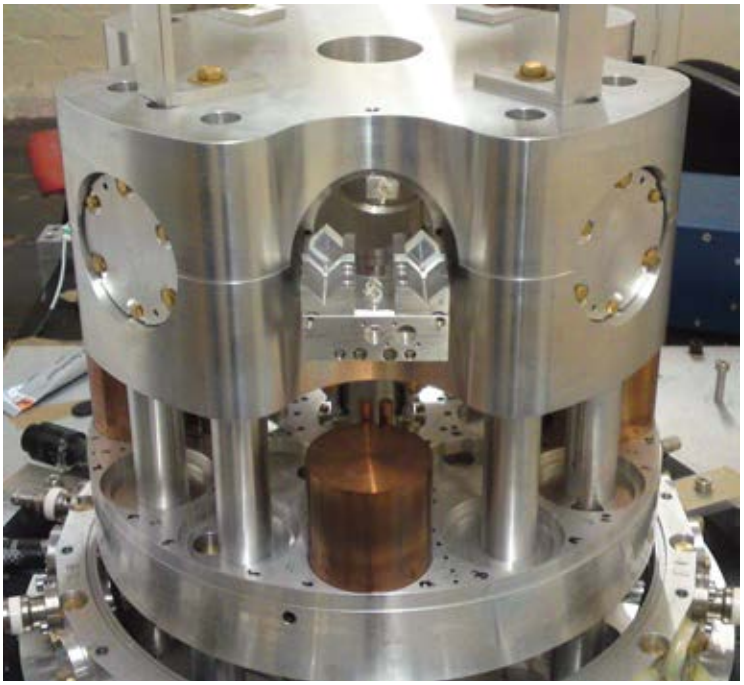

Figure 4.8: Iliad mechanical holder installed into the torsion balance apparatus (centre). Image taken before all optics aligned.

where (x_1, y_1) and (x_2, y_2) are the coordinates of the two points. This can be converted to an angle by dividing by the appropriate distance between the two measuring beams, 0.04m.

4.5 Performance Characterisation

To set a benchmark performance for the device, several experimental tests were performed.

1. The first measurement set was to characterise the device's range of operation in terms of measurement angle.

2. The second measurement set was to calibrate the device in order to determine the extent to which our conversion from voltage to angle is valid.

3. The third set of measurements involved testing the effect a displacement and large rotation of the test mirror would have on the calibration. This would inform us of the level of linearity of the device.

4. Finally the angular sensitivity is tested in various regimes.

Unless otherwise stated these tests were carried out using a Thorlabs Inc. [98] LDC201 current source providing 20mA to the laser and the raw photodiode outputs being logged via a USB ADC card and a Labview data capture programme. For each measurement run any conversion to angle or processing was done offline via Matlab.

4.5.1 Dynamical Angular Range

To measure its dynamical range Iliad was mounted on an optical bench with a mirror placed on a rotating platform also attached to a linear translation stage. A secondary mirror was attached to the back of the primary one which allowed a He-Ne laser to be used as an optical lever to independently measure the approximate angle of rotation of the mirror. The setup is shown in figure 4.9. Initially the mirror was placed at the sweet spot and then rotated to various positions within a $\pm 1.5^\circ$ range. At each position the mirror was slightly vibrated in order to produce a minimum of one full fringe and the absolute angle recorded by the optical lever setup. Figure 4.10 shows a plot of the normalised size of the Lissajous pattern, determined by Pythagorean sum of ellipse radii, as a function of mirror rotation angle. This was repeated at various positions of the mirror from the sweet spot. As reported for the linear displacement device Euclid [100] a figure of merit of 50% of the maximum fringe visibility can be used to determine the best operating conditions. At this level the range of the device is just under $\pm 1^\circ$, however motion of the mirror can still be resolved well below this figure and intrinsic errors due to non-linearity are of more concern at higher angles. Zeemax[2] simulations conducted [94] of the theoretical

[2]Optical Design Software, Radiant Zeemax LLC

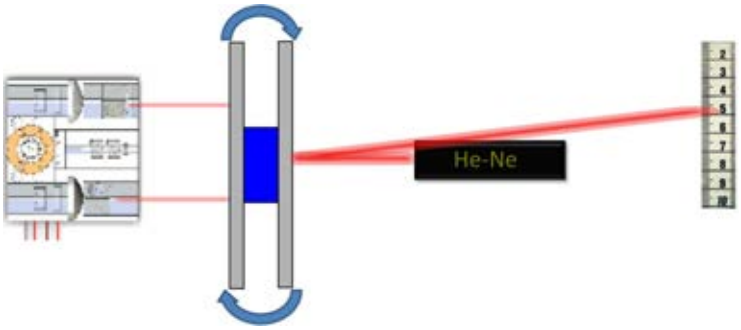

Figure 4.9: Setup for measuring dynamic range of Iliad. Central mirror is rotated out to the limits of Iliad sensitivity and the angle is independently measured by an optical level using a He-Ne laser.

fringe amplitude as a function of rotation angle show that small misalignments of the optical components in the cat's eye can cause large drops in the fringe visibility out to larger angles. It would be beneficial in future work to characterise the tolerances to these misalignments however it must be noted that even with this 'trial and test' method of alignment the interferometer still works to within a large angular range.

4.5.2 Device Calibration

To calibrate the Iliad device the optical lever used in the previous test was replaced by the autocollimator described in chapter 2. The mirror was rotated by $\pm$1.5mrad and once again raw photodiode data was obtained through a USB ADC card using a Labview data capture programme. As discussed in section 4.4 in order to translate the photodiode outputs into a rotation angle the amplitudes and offsets of each channel need to be equalised. This circular Lissajous pattern can be obtained by multiplying each photodiode output by a suitable gain. However this would only be robust if, from equation 4.7, the ratio of a_i's for PD_1 and PD_3 is equal to the ratio of respective b_i's. In the real system where optical alignment was not rigorously assessed it is quite likely that this is not the case. Tests confirmed that a change in intensity would cause a movement of the centre of the Lissajous pattern. A second method of circularising the Lissajous pattern is by fitting

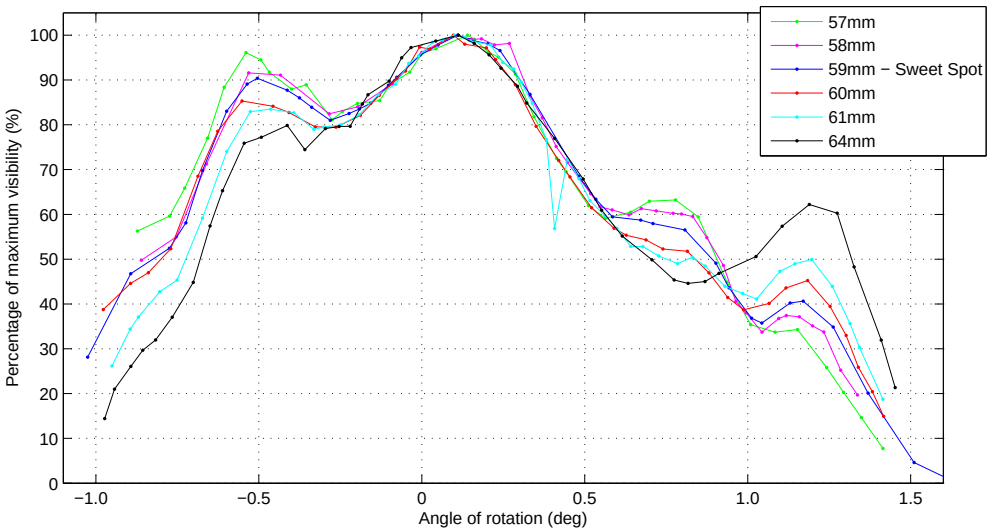

Figure 4.10: Visibility of Iliad output as a function of mirror rotation angle.

ellipses. Subsequent tests were carried out using this as the preferred method for converting to angle data. The ellipse coefficients were obtained through the technique described by Halir and Flusser[101] and used to centre and circularise the pattern. Data from both Iliad, from the centred Lissajous pattern, and the autocollimator were logged. For each run the Iliad data was down-converted from its original 10kHz sampling frequency to the autocollimator sampling frequency of 12.5Hz. Both data sets were then interpolated and fitted using a standard linear least squares fitting function. Figure 4.5.2 shows the outputs from each stage of this procedure.

The largest source of uncertainty within the conversion formula 4.8 is from the wavelength of light and the width between the two interferometer arms at the mirror. These are systematic errors which would cause an offset in the measured angle. Figure 4.14 is a plot of the linear fit coefficients of Iliad and autocollimator for 14 repeated measurements of mirror rotation. The systematic uncertainty in the wavelength and arm width is given by the offset in calibration away from unity. The spread in the measurements can be attributed to mechanical vibrations induced by manually rotating the mirror on its rotation

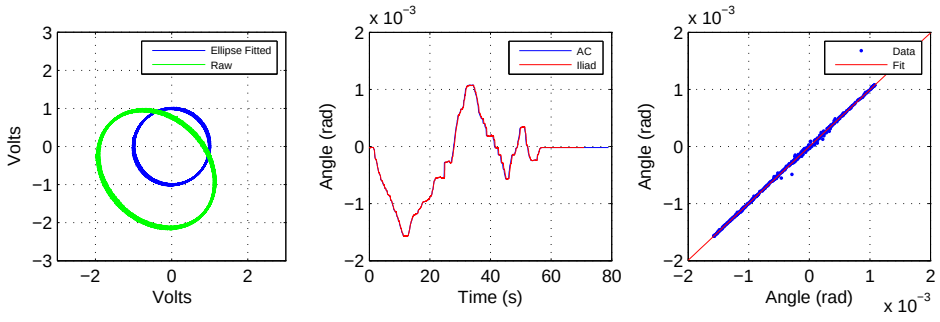

Figure 4.11: Method of assessing linearity. Left: Plot of raw and corrected Lissajous pattern. Centre: Typical mirror movement tracked by autocollimator and Iliad. Right: Data from autocollimator plotted against Iliad and the fit.

stage. This standard deviation of 1.3×10^{-3} is the minimum uncertainty associated with the subsequent set of linearity tests.

4.5.3 Linearity Tests

The next set of characterisation studies conducted on the interferometer were to test how the previously measured calibration would change when the test mirror was displaced from its sweet spot and when the mirror was rotated to larger angles. In the first regime the setup was the same as the initial calibration. The test mirror, initially set at the sweet spot, was rotated manually back and forth within the range of the autocollimator which was approximately ±1.5mrad. The data was then analysed in the same way as the previous test to obtain least square fit coefficients. Both the quadratic coefficients and the constants averaged to zero. The results shown in figure 4.15 confirm that within our measurement accuracy, of 1.3×10^{-3}, there is no observable change in the linearity for different positions of the target mirror. The actual calibration coefficient in these results is slightly different from the previous test since the optics had subsequently been fixed to the holder using UV curing adhesive. Although this would change the calibration coefficient slightly, due to a possible change in the width of the arms, the measurement error which is solely due to the experimental setup still holds.

The second set of measurements were taken as the mirror rotates to larger angles. The errors in terms of defocus and spherical aberrations have been analysed by F.E. Peña-Arellano [92] and presented in our paper [94]. Quoting from the paper the total optical path length measured by Iliad as the mirror rotated is given by

$$L_{H'I'} - L_{HI} = l_s[4 - (\tan 2\theta)^2] \tan\theta, \tag{4.9}$$

where $L_{H'I'}$ andL_{HI} are the path lengths from each arm, l_s is the distance between the two arms and θ is the real angle of rotation. The common effect of spherical aberrations cancel out and the measured angle can be written as

$$\theta_m = \frac{L_{H'I'} - L_{HI}}{4l_s} \approx \theta - \frac{2}{3}\theta^3. \tag{4.10}$$

This formula provides the accumulated error in the estimate of theta when, at the beginning of the measurement the mirror is aligned. In the case in which the mirror is not initially aligned but tilted by an angle θ_0, the measured angle $\Delta\theta$ becomes

$$\Delta\theta_m = \Delta\theta - \frac{2}{3}(\theta^3 - \theta_0^3) \tag{4.11}$$

where $\Delta\theta = \theta - \theta_0$.

Due to the limited angular range of the autocollimator, one of the factors which drove the development of Iliad, the experimental setup needed to be adjusted. This time Iliad was mounted on a plate which could be rotated independently around the test mirror as shown in figure 4.12. The position of Iliad with respect to the mirror was determined through an optical lever sensing a mirror also attached to the rotating plate. For each measurement Iliad would be rotated to the measurement position, the test mirror once again manually rotated within the range of the autocollimator and the data from each device fitted. This

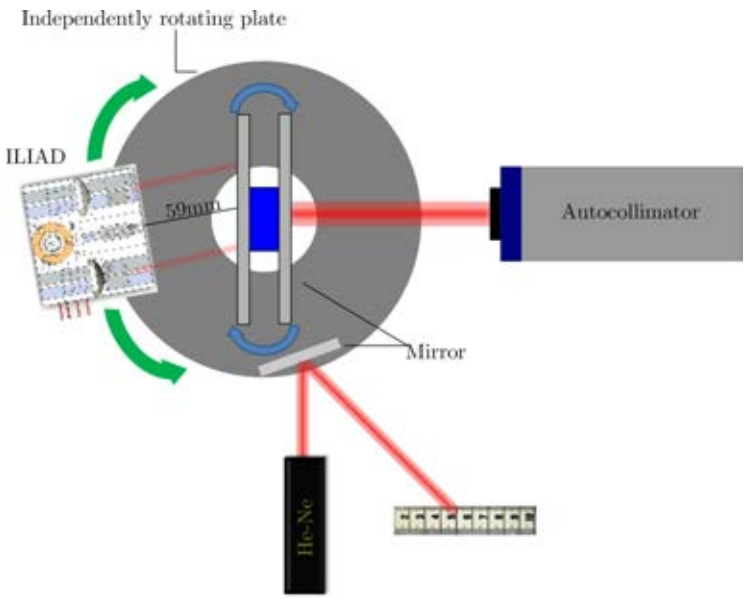

Figure 4.12: Setup for measuring linearity at large rotation angles. Size of angle between Iliad and test mirror exaggerated for visual purposes. He-Ne laser, via optical lever method, used to measure this angle.

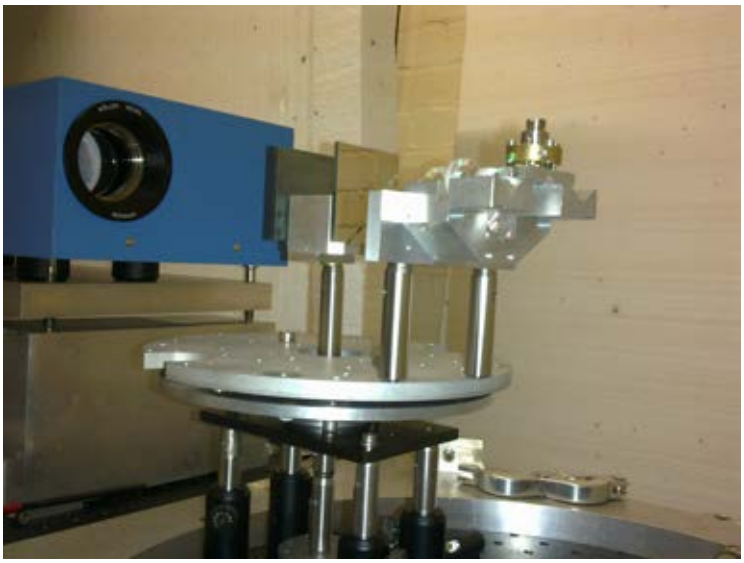

Figure 4.13: Photo of setup for measuring linearity at large rotation angles. The mirror and He-Ne laser used to independently measure the Iliad angle is not shown here.

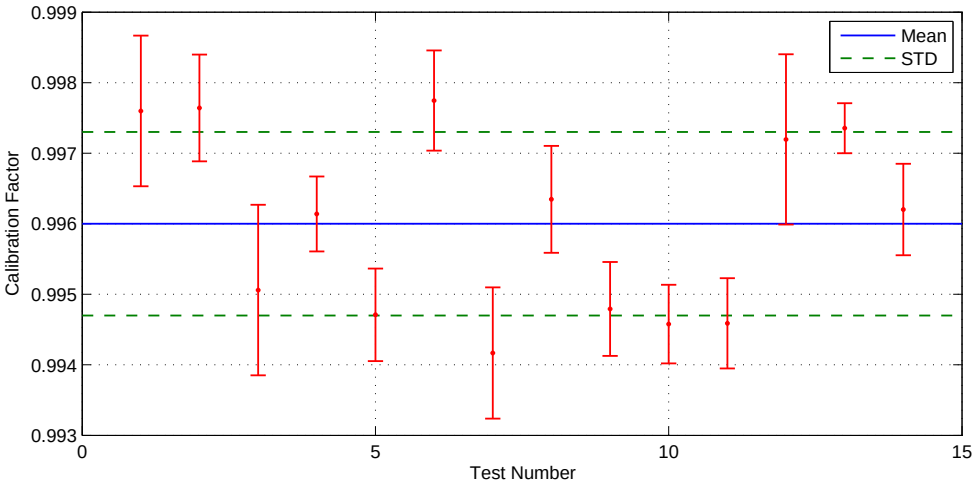

Figure 4.14: Calibration factor of Iliad repeated 14 times at the sweet spot. Mean = 0.9960, Std = 1.3×10^{-3}

procedure was carried out at various angles within the range of Iliad and the calibration factors plotted in figure 4.16. Unfortunately, the resolution of the measurements were not good enough to detect the deviations predicted by simulations, a few parts in 10^4 for the largest of rotation angles. However once again the results show no deviations within this resolution of 1.3×10^{-3}, which is remarkable considering that the device was aligned without precision tools and techniques such as shearing interferometers.

4.5.4 Angular Sensitivity

The ultimate sensitivity of the Iliad device is limited by the intrinsic noise sources within the system. At higher frequencies of >100 Hz the majority of the noise comes from shot and digitisation noise. At lower frequencies $1/f$ electronics noise and environmental effects play a bigger role. Shot noise is the fundamental effect of current travelling in discrete packets rather than as a continuous stream [102]. Similarly photons incident on a photodiode will not be continuous producing fluctuations. This power spectrum shot

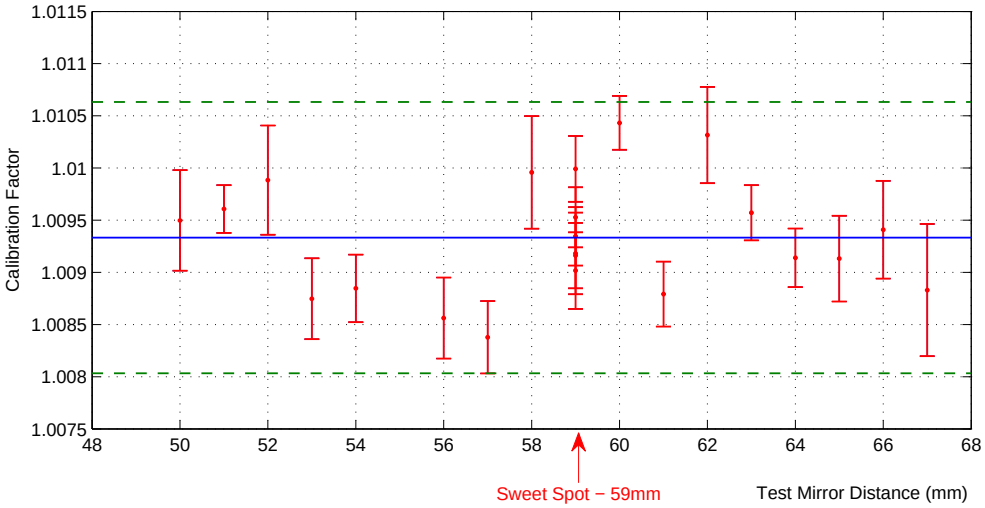

Figure 4.15: Calibration factor as a function of mirror distance. Sweet spot is at 59mm

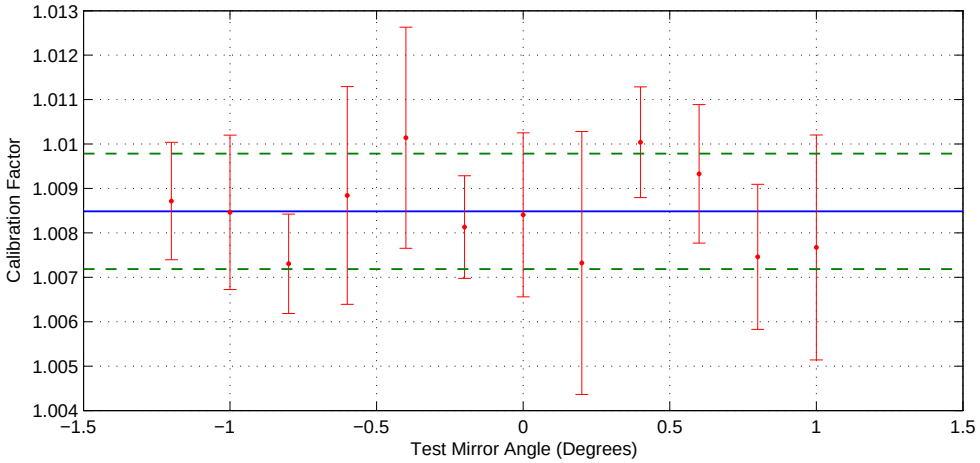

Figure 4.16: Calibration factor as a function of mirror angle.

noise of the photocurrent, I_c, is given by

$$S_{shot}^{1/2}(f) = \sqrt{2eI_c} \times Rf \tag{4.12}$$

in units of $V/\sqrt{Hz}$, where e is the charge on the electron and Rf is the feedback resistor within the transimpedence amplifier stage. Noise also occurs from the digitisation of the signal through the ADC card. This is given by

$$S_{ADC}^{1/2}(f) = L_{rms} \times \frac{V_{range}}{2^N} \times \sqrt{\frac{1}{(fs/2)}} \tag{4.13}$$

where L_{rms} is the least significant bit RMS of the ADC, V_{range} is the voltage range, N is the number of bits and fs is the sampling rate. Most data described were logged through a transimpedence stage which used an Rf of 69kΩ, with 8 times gain, and the 16 bit ADC card previously mentioned. A typical photocurrent produced when the laser was set to an intensity of 20mA was 2μA. This gives a shot noise level of $10^{-6}V/\sqrt{Hz}$. The limiting factor is the ADC board which if using a voltage range of ±5V and a sampling rate of 990Hz, higher sampling rates produced files sizes which were very large to analyse, gave a noise limit of $1 \times 10^{-5}V/\sqrt{Hz}$. Initial measurements of Iliad with a static mirror showed noise levels higher than this limit and causes of these errors were investigated.

Laser Frequency Fluctuations

Instabilities in the frequency of the laser due to spontaneous emission into the resonator modes will propagate through the interferometer as a phase delay if the arms of the device are unequal. Intrinsically the design of Iliad creates unequal path lengths between the arms due to the requirement of one of the beams to travel through an extra beam splitter. A further optical component of the same material and dimension as this extra beam splitter

was therefore added in the path of that arm. In our case we used a polarising beam splitter of the same kind as PBS A placed in the optical line connecting PBS C and PBS Eb. The effect of these fluctuations can be determined by first considering the path length difference, equation 4.4. The phase measured for a mirror displacement, d, is given by

$$\Delta\phi = \frac{8\pi d}{\lambda} \tag{4.14}$$

Any erroneous displacement at this distance can be interpreted as an extra phase change

$$\delta x = \delta\phi \frac{\lambda}{8\pi} \tag{4.15}$$

which can be brought about by a change in the laser wavelength

$$d(\Delta\phi) = -\frac{-8\pi d}{\lambda}\frac{d\lambda}{\lambda} \tag{4.16}$$

$$\delta x = -\frac{d}{\lambda}\delta\lambda \tag{4.17}$$

The spectrum of the intrinsic frequency fluctuations is given by Owens [103] as

$$\delta f^2(\nu) = \frac{D}{\pi} \tag{4.18}$$

$$\frac{\delta f}{f} = -\frac{\delta\lambda}{\lambda} \tag{4.19}$$

where D is the intrinsic linewidth of the laser. The coherence length of a laser is given as

$$L \approx \frac{\lambda^2}{\Delta\lambda} = \frac{c}{D} \tag{4.20}$$

where $\delta\lambda$ is the linewidth in terms of wavelength. These can be substituted into equation (4.15) to give the spectrum of displacement errors due to frequency fluctuations.

$$\delta x = \lambda d \sqrt{\frac{1}{cL\pi}} \tag{4.21}$$

with units of $m/\sqrt{Hz}$. It has been reported[3] that the coherence length of our 1550nm DFB laser is given as being between 6m - 10m. This gives an upper limit of $\delta x \approx d \cdot 2 \times 10^{-11} m/\sqrt{Hz}$. Thus even for large angles up to the maximum range of Iliad of $\pm 1.5^\circ$ the displacement noise due to frequency fluctuations is less than $1 \times 10^{-14} rad/\sqrt{Hz}$, well below the other limiting factors within the system.

Laser Intensity Noise

The laser may also experience fluctuations in its output intensity due to thermal and acoustic effects along with fundamental quantum properties [102]. This may also propagate into displacement noise through the differing properties of the photodiodes. A more accurate model than those of equations 4.7 can be given for the signal on the photodiodes

$$I_1 = \alpha(\gamma b_1 + a_1 \beta \cos(\phi)) \tag{4.22}$$

$$I_2 = \alpha(\gamma b_2 + a_2 \beta \sin(\phi)) \tag{4.23}$$

$$I_3 = \alpha(\gamma b_3 - a_3 \beta \cos(\phi)) \tag{4.24}$$

where the addition of β and γ are effects due to mirror rotation and α are intensity fluctuations from the laser. Since alignment of beams on each photodiode are not identical a change in laser intensity, α, will cause a different change in each photodiode. The ellipse fitting method described earlier fits an ellipse to the data as a whole. If over longer timescales temperature fluctuations caused intensity changes these would manifest themselves as a shift in the centre of the Lissajous pattern causing the initial ellipse fit parameters to be wrong. Real time ellipse fitting could be used however when sensing

[3]Reported in Distributed-feedback (DFB) Laser Coherence and Linewidth Broadening - http://dspace.dsto.defence.gov.au/dspace/bitstream/1947/3355/1/DSTO-RR-0263%20PR.pdf

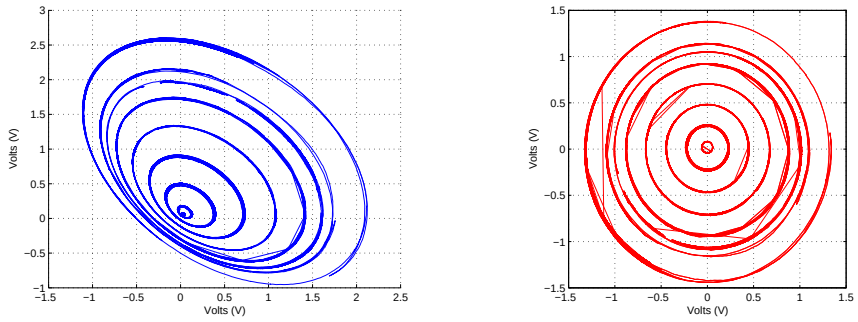

(a) Lissajous Pattern using original subtraction formula 4.7

(b) Lissajous pattern using new formula 4.25

Figure 4.17: Lissajous patterns for differing input intensity using the old photodiode subtraction method and the new intensity rejection method

angles smaller than $\lambda/8$ i.e. less than a fringe for example on the torsion balance not enough data is available to accurately fit ellipses continuously. We solved the above three equations to reject the common intensity fluctuations giving

$$\tan\phi = \frac{1}{a_2}\left[\frac{I_2(a_1b_2 + a_3b_1) - b_2(I_1a_3 + I_3a_1)}{I_1b_3 - I_3b_1}\right]. \tag{4.25}$$

All the common fluctuations cancel leaving a centred circular Lissajous pattern whose radius changes as a function of laser intensity. Figure 4.17 shows the effect of intensity changes on the Lissajous pattern for different methods of plotting and proves the stability of formula 4.25. This method of converting to angular displacement was used for noise measurements, since a rigid mirror does not provide enough points to fit an ellipse, and also for realtime analysis during the final experimental run.

Final Angular Sensitivity

The Iliad angular interferometer was initially developed to be used in Torsion Balance type experiments whose signal of interest is usually at lower frequencies $< 10^{-2}Hz$. Here the noise is dominated by 1/f noise from the electronics. A new electronics module has been

developed in-house by Mr. Dave Hoyland which takes advantage of low-noise amplifiers and high data sampling rates of up to 1MHz. It has incorporated field programmable gate arrays (FPGA) which can perform the various operations required to convert the voltage signal into a displacement output. The first version of this module did not include the intensity rejection formula 4.25 rather using gains to equalise the photodiodes and only outputs to the computer the final displacement value. Therefore in order to make use of the intensity rejection formula, data needed to be obtained through the USB ADC card. A number of measurements were made to characterise the noise within the system and are as follows:

1. To assess the limits of the electronics a set of resistors were placed at the input which resembled a real interference signal. Data were obtained directly from the new electronics module and via the USB ADC at a sampling rate of 4990Hz.

2. To assess the noise inherent in electronics and the photodiodes the laser was setup to shine directly onto the photodiodes without the interferometer in place. Two beam splitters and a neutral density filter were used to vary the intensity on each photodiode such as to mimic a real interference signal similar to the resistors in the previous test. Data were again obtained via both outputs.

3. To assess the interferometer sensitivity Iliad was replaced and a rigid mirror positioned at the sweet spot. The setup was shielded to reduce effects of air turbulence. Data from the USB ADC card were taken at 990Hz.

The results of these three measurements are shown in figure 4.18. The higher sensitivity of the new electronics module is evident, at 1Hz its noise is approximately $6\times10^{-13}\text{rad}/\sqrt{Hz}$ while the intrinsic noise of the USB ADC matches that obtained by using formula 4.13 of $1\times10^{-11}\text{rad}/\sqrt{Hz}$. The photodiode test using the new module (brown) shows an excess of noise with respect to the bare electronics (purple). Shot noise is expected to be at $1.5\times10^{-12}\text{rad}/\sqrt{Hz}$ which does not account entirely for this excess. One of the candidates

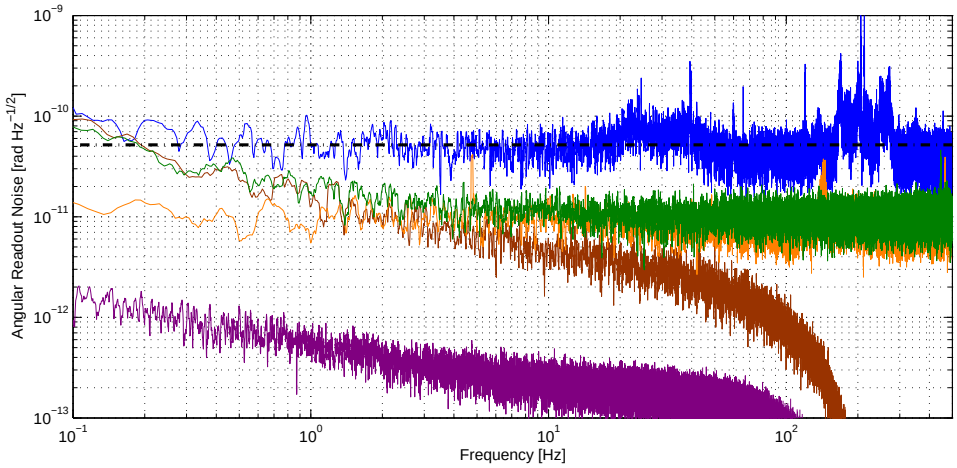

Figure 4.18: Sensitivity of Iliad and its components. Blue - Iliad Device with rigid mirror, Green - Laser and photodiode setup through USB ADC, Brown - Laser and photodiode setup through new module box, Orange - Intrinsic electronic noise of USB ADC, Purple - Intrinsic electronic noise of new module box. Note: New electronics module has internal filter producing the roll off above 50Hz.

at lower frequencies could be air turbulence however the origin of the noise above 1Hz is still unknown. Finally the blue curve shows the sensitivity of the Iliad device on an optical bench in air. In the range between $10^{-1}Hz$ and $10Hz$ the noise spectrum is almost flat, and is about 5×10^{-11} radians/$\sqrt{Hz}$. Below $10^{-1}Hz$ the signal is most likely limited by effects induced by thermal drifts and air currents, whereas at higher frequencies ($\approx 10Hz$ and above) the features indicate it is limited by mechanical vibration in the measurement apparatus. The exact source of the broadband excess noise seen between the measurements of the intereferometer and photodiodes alone is not fully understood. It is quite possible that mechanical vibrations are the only cause of this and a better assembly within a vacuum environment may produce better results. However it is important to note that these measurements confirm an upper limit on the Iliad device angular sensitivity of 5×10^{-11} radians/$\sqrt{Hz}$ between $10^{-1}Hz$ and $10Hz$.

4.6 Iliad on the Torsion Balance

Once the characterisation studies were complete, Iliad was installed onto the torsion balance apparatus. The smooth oscillatory motion of the torsion balance also provided a good platform to further test the device linearity. Data from Iliad and the autocollimator was logged for a number of oscillations and subsequently split into small 140 second windows. Each section was fitted with the same procedure as previously employed. The results, plotted in figure 4.19, show that the standard deviation of fit coefficients in this setup was 2×10^{-4}, small enough to compare to the theoretical predictions. Since the range of the autocollimator is smaller than our testing parameters, these measurements were slightly more complicated to perform. To rotate the torsion balance with respect to Iliad one set of damping electrodes were used to bias the equilibrium position of the balance. The autocollimator was then rotated manually to the necessary position and then the second set of electrodes were used to damp the oscillations down to the range of the autocollimator $\pm$1.5mrad. At each angle the torsion balance was allowed to oscillate a number of times and the same data procedure described previously was used to assess the linearity coefficients. The results, shown in figure 4.20, are surprising due to the assymetry of the coefficients. Indeed the amplitude error agrees with the theoretical results, also plotted in blue, however since there was no quantifiable assessment of the alignment of the device it is difficult to predict a reason for these results. Further discussion and analysis is required although it is only of concern to users who require a relative error of better than 1×10^{-3} and measuring angles out to the limit of the device.

4.7 Conclusions

The development and characterisation of the first prototype Iliad device has been a substantial part of the overall project. The increased sensitivity over the current state of the

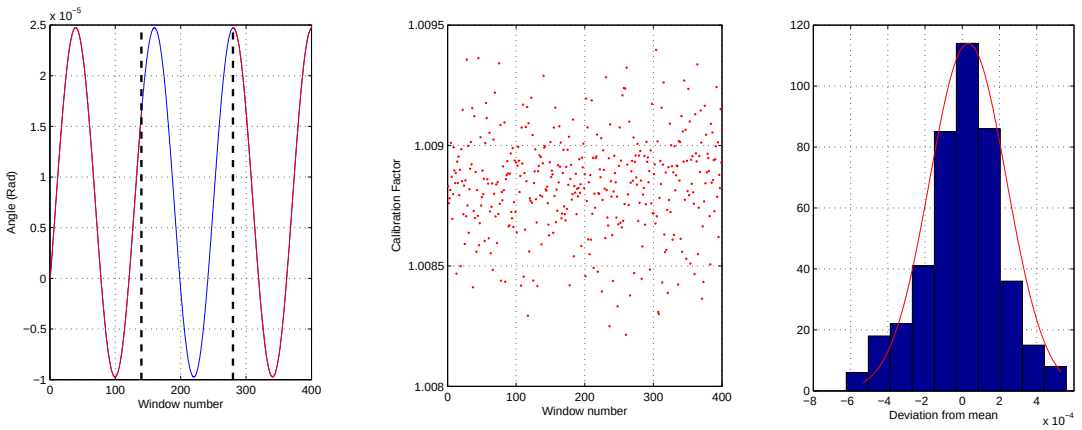

Figure 4.19: Calibration on Torsion Balance. Left: Example of windowing of time series data. Centre: Linear Calibration coefficients for each window. Right: Histogram of residuals from mean calibration coefficient and Gaussian fit.

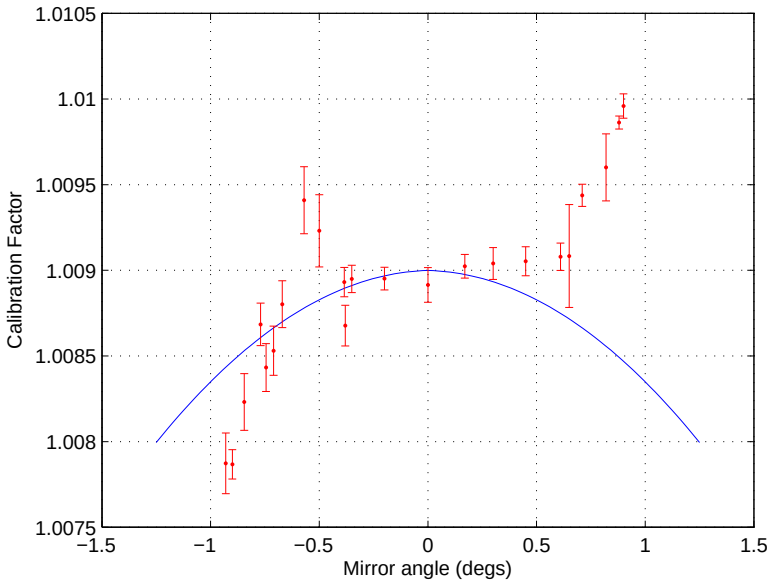

Figure 4.20: Calibration factor with respect to Iliad angle on Torsion Balance. Red: Torsion Balance Data. Blue: Theoretical using eq 4.11

art autocollimator allows the benefits of using torsion strip balance to be fully exploited. Its compact design also makes it less sensitive to environmental effects for example thermal drifts which couple into the autocollimator signal due to its large size and mounting requirements. The device also has a great degree of tilt immunity both in its assembly and operational alignment which makes it ideal for use in these types of experiments. Although the drive to develop this instrument was for the use in our torsion balance experiment its application is much wider. Our studies showed that even through a non quantitative alignment process the device showed remarkable properties, having a large dynamical range of over $\pm 1^{\circ}$ and still being linear to within 1 part in 10^3 out to large rotational angles. Further tests should however be carried out to understand the origin of some of the differences from simulations, for example the 'wings' seen in figure 4.10. This effect could be due to back reflection into the laser and can be tested by checking for any erroneous displacement signal with only one arm sensing the mirror. Also a thorough investigation into the alignment process should be carried out using proper techniques such as shearing interferometers so that theory and experiment can be quantitatively compared.

Chapter 5

Data Analysis and Systematics

As described previously two source masses were modulated every 800 seconds between positions of maximum torque on the torsion balance. This section describes the analysis procedure to convert from the measured angle to a torque signal and systematic effects which may interfere with the detection of a real signal.

5.1 Data Collection and Conversion

Each of the five sets of experimental and environmental data; autocollimator detected angle θ_{ac}, Iliad detected angle θ_{il}, temperature, tilt and motor position were logged to separate files every 12 hours. Although the sampling rate varied for each set the reference time was equivalent for all the data.

The autocollimator senses the position of the reflected beam in both X and Y co-ordinates and thus gives information on the rotation and tilt of the balance. However, since the autocollimator is not positioned exactly parallel to the base plate of the torsion balance there will be some mixing between the two signals depending on offset angle θ. A schematic of this is shown in figure 5.1. To remove this effect the data was subjected to a rotation

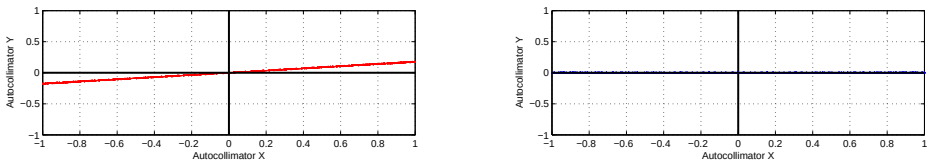

Figure 5.1: Schematic example of autocollimator output before and after adjusting for rotation.

matrix 5.1 for varying values of θ until any frequency component of the 800s modulation signal on the Y data was minimised.

$$\begin{bmatrix} X \\ Y \end{bmatrix} = \begin{bmatrix} \cos(\theta) & -\sin(\theta) \\ \sin(\theta) & \cos(\theta) \end{bmatrix} \begin{bmatrix} x \\ y \end{bmatrix}. \tag{5.1}$$

For each 12 hour data set the the torsion balance angular position data is first low-pass filtered to avoid down conversion of readout noise. Secondly this angle is converted to instantaneous torque via the use of quadratic fitting[104, 105] to 15 consecutive data points

$$X = X_0 + \dot{X}t + \ddot{X}\frac{t^2}{2}, \tag{5.2}$$

where X_0, $\dot{X}$ and $\ddot{X}$ are estimates of the position, velocity and acceleration given in the equation of motion 2.1. All other environmental parameters are then linearly interpolated to match this torque time series.

For each oscillation of the source masses the mean torque was obtained by averaging data over the time the source masses were stationary. This time was determined through the analysis of the motor position data. It must be noted that this data is the expected position of the source masses given by the commands sent by the computer. There is no absolute reference on the source mass positions. Each movement of the source masses between positions of maximum torque takes approximately 170 seconds leaving about 230 seconds of time while they are stationary. The first 25 seconds worth of data was discarded

at the beginning of each of these 230 seconds sets to allow the damping of the pendulum and a further 5 seconds of data discarded at the end of the set to ensure fluctuations in the starting time of the motor were ignored. For each set the coherent torque and environmental data were saved and averaged to output a single point associated with each movement of the source masses. Figure 5.2 shows an example of this process.

5.2 Least Squares Fit

The torque model and any systematics can be fitted using a general least squares fitting procedure which minimises the squared error between the observed data and a number of fit parameters [106]. For example

$$Y = f(X) + \epsilon, \tag{5.3}$$

where Y is our observed variable, $f(X)$ is a function of our correlation variables and ϵ the excess noise. For y_i data points each with σ_i standard deviation and b_j variables with $x_{j,i}$ points we attempt to minimise the χ-*square* function

$$\chi^2 = \sum_{i=1}^{n} \frac{(y_i - f_i(x_{j,i}))^2}{\sigma_i}^2 . \tag{5.4}$$

We can rewrite this equation in matrix notation. Consider our N observables as a vector $\mathbf{y} = (y_1, ..., y_N)$ and let $\mathbf{X}$ be an $N \times P$ matrix of

$$\mathbf{X} = \begin{bmatrix} x_{1,1} & x_{1,2} & . & . & x_{1,P} \\ x_{2,1}. & x_{2,2} & . & . & . \\ . & . & . & . & . \\ x_{N,1} & x_{N,2} & . & . & x_{N,P} \end{bmatrix} . \tag{5.5}$$

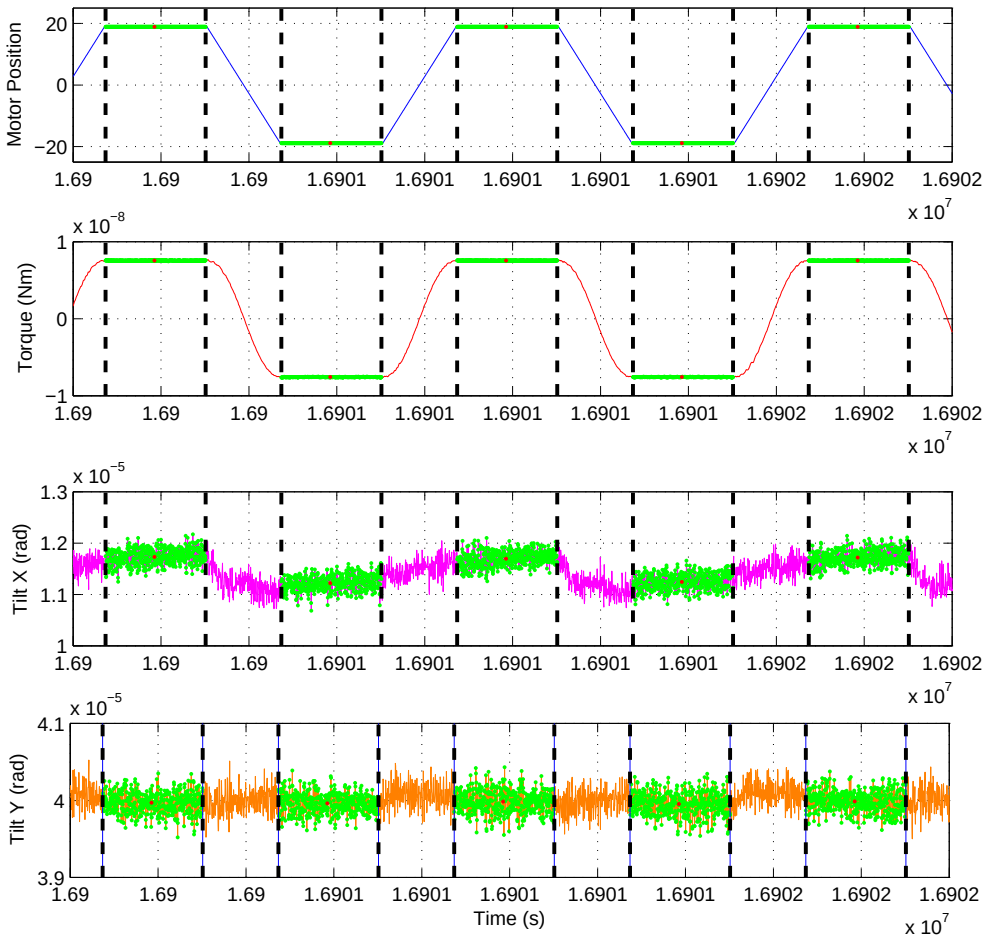

Figure 5.2: Experimental data from top, motor position, pendulum torque, tilt X reading, tilt Y reading. All data have been interpolated to the same timebase. Green points signify the time while the source masses are stationary. Red dots are the average of these points (excluding 25 seconds from the start and 5 seconds from the end.)

Each of the columns in $\mathbf{X}$ represents our parameters and rows are the data points. We also define a vector, $\mathbf{A} = (a_1, ..., a_P)$ which are the coefficients to be fitted. The minimum occurs by differentiating with respect to each coefficient obtaining a set of P equations

$$\sum_{i=1}^{N} \frac{y_i X_k x_i}{\sigma_i^2} - \sum_{j=1}^{P} \frac{a_j X_j(x_i) X_k(x_i)}{\sigma_i^2} = 0, \tag{5.6}$$

where $k = 1, ..., P$. In matrix form this is given as

$$\mathbf{X}^T \mathbf{V}_y^{-1} \mathbf{y} = (\mathbf{X}^T \mathbf{V}_y^{-1} \mathbf{X}) \mathbf{A}, \tag{5.7}$$

where $\mathbf{V}_y^{-1}$ is a diagonal matrix of the errors associated with the data points. The standard uncertainties related to the fitted parameters can be given by

$$\sigma^2(a_j) = \sum_{i=1}^{N} \sigma_i^2 \left(\frac{\delta a_j}{\delta y_i} \right)^2, \tag{5.8}$$

which leads to

$$\sigma^2(a_j) = (X^T V_y^{-1} X)_{jj}^{-1}. \tag{5.9}$$

The inverse matrix $(\mathbf{X}^T \ \mathbf{V}_y{}^{-1} \ \mathbf{X})^{-1}$ is known as the covariance matrix and its diagonal components are the standard errors on the fit parameters which are intrinsically linked to the original data variance. For each of our data points we allocate an error, σ_i as the mean standard error associated with the averaging procedure. Thus the *reduced chi-square* statistic, equation 5.4 divided by the degrees of freedom, gives a measure of the goodness of fit. A value of 1 indicates a good match since the variance of the residuals matches the variance given in the fit. This indicator can be used when fitting for various systematics.

5.3 Expected Torque Model

Any temporal signatures in the Newtonian constant will manifest as an amplitude change in the detected torque on the balance which is an uncalibrated measurement of G, the gravitational constant. We can model the torque as

$$\tau_M = \tau_N + \sigma, \tag{5.10}$$

where τ_M is the measured torque, τ_N is the Newtonian torque and σ are any real sources of fluctuations or systematic effects. Modulating the source masses can separate out amplitude signals with drift signals reducing the sources of noise within the experiment. Referring to our analysis technique, each torque point can be described as

$$\tau_{M_i} = \alpha + (\pm)(\tau_N + \sigma_{signal} + \sigma_{systematic}) + \gamma(\theta) + \epsilon, \tag{5.11}$$

where α is an offset, σ_{signal} and $\sigma_{systematic}$ are the additions associated with any signal and systematic event and ϵ is the statistical uncertainty on each point. The $\pm$ refers to each change in the source mass position defining the amplitude of the torque signal. Any signal or systematic that couples to the torque amplitude must also be allocated a $\pm$ to their data points. The final term is the mean pendulum angle where γ would be equal to the torsional coefficient of the pendulum and is included to account for any drifts. A least squares fit is used to obtain values of α, τ_N and γ and once subtracted gives the $\delta G/G$ residuals.

5.4 Temperature Systematic

The first source of systematic errors are temperature changes and gradients that can cause unknown changes in the apparatus. Although as described in chapter 2 efforts have been taken to ensure temperature fluctuations within the laboratory are minimised it is still nonetheless important to assess its impact. To establish a calibration coefficient the temperature was oscillated by manually adjusting the set point of the Julabo stabilised water tank by ±1K every 10 hours. A second measurement at a different frequency, 9 hour oscillation, and a smaller amplitude, ±0.15K, was conducted by heating a length of copper pipe in which the water passed through before going into the two thermal boxes via the control of current through a thin wire wrapped around the pipe. The small amplitude was due to the limitation of the current source output power. The torque output data was fitted against the temperature for both these two measurements and longer 5 and 25 day runs. In all cases the coefficient associated with the vacuum temperature lay within the bounds 5×10^{-12} to 8×10^{-13}. The fact that the coefficient was the same for both Iliad and the autocollimator suggests that, at this level, the temperature is directly affecting the torsion balance as opposed to an artefact from the autocollimator mounting. An estimate into systematic error associated with the temperature can be determined by fitting the full temperature profile over the experimental run to a sidereal sinusoid. The obtained amplitude was $4.4\pm2\times10^{-4}$. When using the upper limit for the coefficient this amplitude relates to a signal in $\delta G/G$ of $3\pm1\times10^{-7}$, an order of magnitude smaller than our current noise levels.

5.5 Tilt Systematic

Although the tilt in the long axis (Y axis) of the optical bench is stabilised via the controlled piezo as described in chapter 2 there are still a number of tilt effects which may

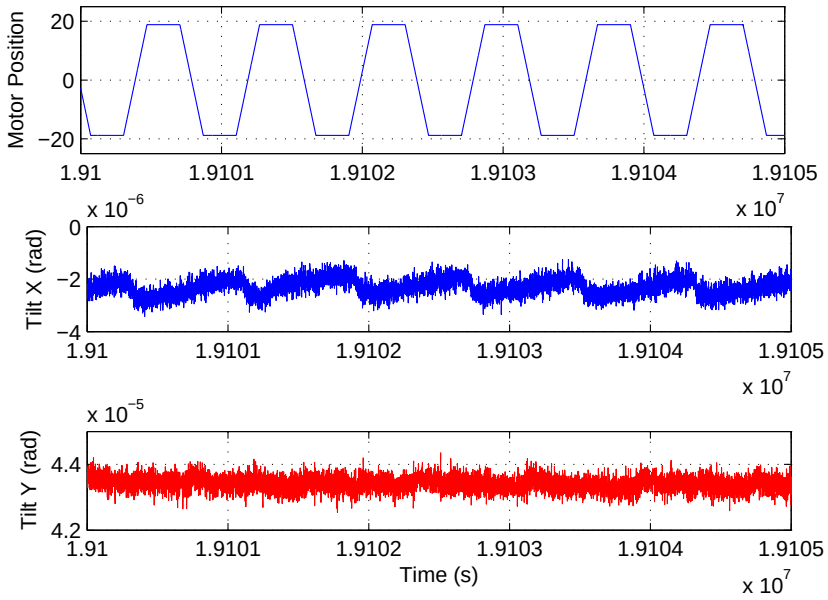

Figure 5.3: Tilt readings showing the impulse felt by the table, particularly noticeable in the tilt X, when the motor moves.

produce a false signal. Firstly, the tilt in the short axis of the table (X axis) has not been stabilised and thus could be a source of a false signal. Secondly, each time the motor moves the source masses a small tilt is induced on the table, mainly in its X axis as shown in figure 5.3. As the torsion strip bends to compensate for the tilt there will be an induced twist due to the clamping of the fibre. If the amplitude of these motor driven tilts change over day like timescales the amplitude excess caused by an induced twist can be a source of false signals. A previous test on the first development of the BIPM torsion balance[36] determined a rotation produced by a tilt contribution of 0.4%± 0.2% in one axis of the setup. It is expected that any tilt-rotation effect will be much lower than this level since our torsion strip is supported via a knife edge gimball as described in chapter 2. However using this value as an upper limit for our setup, if the tilt amplitude oscillates by 0.5μrad it will induce approximately 1nrad of twist in the fibre, equivalent to a torque of 0.2pNm or $\delta G/G$ of 2×10^{-5}.

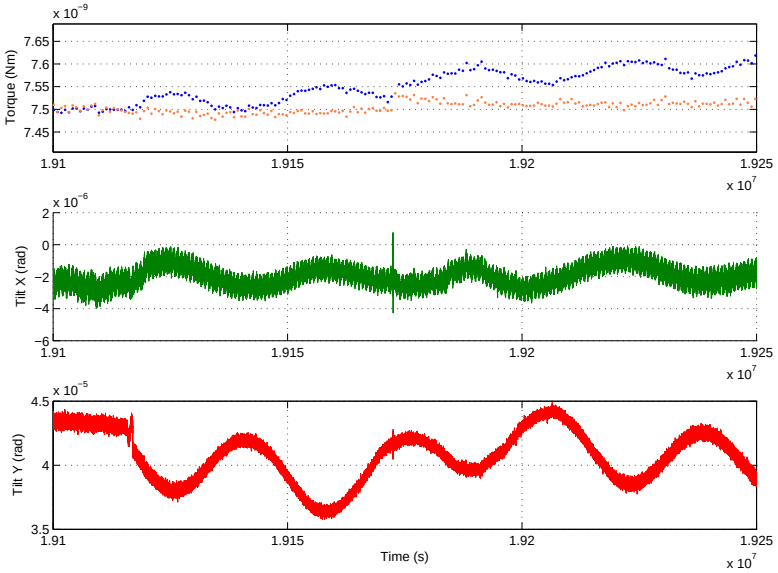

Figure 5.4: Tilt calibration run. Top: output data of torque points from the autocollimaotr (blue) and Iliad (orange), middle: tilt X readings, bottom: tilt Y readings.

To estimate the effect of tilt on the torque amplitude the piezo was used to oscillate the tilt Y with a period of 20 hours and 9 hours. During this time the temperature in the inner box did not fluctuate by more than 0.04K. Figure 5.4 shows the tilt during the 9 hour calibration run and the equivalent torque data from Iliad and the autocollimator. The autocollimator data shows a drift not seen in the Iliad data which can be accounted for by the autocollimator mounting. We remove this drift by fitting to the mean pendulum angle as sensed by each readout. The systematic error associated with the tilt can be expanded to four tilt parameters

$$\sigma_{tilt} \approx a_0 + a_1\theta_x + a_2\theta_y + a_3\Delta\theta_x + a_4\Delta\theta_y, \tag{5.12}$$

where θ represents the average tilt position, referenced to the initial state at the start of the run in both X and Y, and $\Delta\theta$ is the amplitude of the small motor induced kick in both

Parameter	Coefficient Error	Estimated Sidereal Amplitude	$\delta G/G$ signal
a1	$5.8\times10^{-}8$	$4.6\times10^{-}8$	$3.5\times10^{-}7$
a2	$6.9\times10^{-}9$	$4.7\times10^{-}8$	$4.2\times10^{-}8$
a3	$1.6\times10^{-}6$	$3.5\times10^{-}9$	$7.3\times10^{-}7$
a4	$6.4\times10^{-}6$	$3.6\times10^{-}10$	$3.0\times10^{-}7$

Table 5.1: Estimated systematic effects from to apparatus tilt. Parameters as per equation 5.12. Coefficient errors are obtained from the calibration test run oscillating the Y axis tilt every 20 hours. Estimated sidereal amplitudes obtained by fitting sidereal sinusoid to full experimental data set.

X and Y. For both calibration tests the output from Iliad showed no conclusive correlation between the tilt and the torque. For all parameters the standard errors were larger than the associated coefficients suggesting that any effect is smaller than our statistical uncertainty. To set an upper limit on the effect of these tilt parameters we fit them to a sidereal sinusoid to estimate the amplitude over the whole data set and use the obtained coefficient errors obtained in the 20 hour calibration run to convert to an effect on $\delta G/G$. These results are shown in table 5.1. Regarding the autocollimator data the calibration results were inconclusive. Different coefficients were obtained for different tilt amplitudes and similarly for the differing tilt oscillation periods, probably due to effects on the autocollimator mounting system. We therefore ignore the autocollimator data since we cannot adequately estimate the tilt contribution. This was one of the major driving factors for the development of Iliad.

Chapter 6

Results

Two sets of experimental data were used, approximately 30 days from mid December 2011 to mid January 2011 and another 25 days in February 2012. Each set was initially individually analysed to obtain the $\delta G/G_0$ residuals, as per the procedure described previously, and any spurious data points removed. Both sets were then combined with the correct phase to give approximately 50 days worth of torque data points each providing an uncalibrated measurement of G_0, shown in figure 6.1. As can be seen in the figure the February set of measurements is a factor 2 times noisier than the first set which was obtained during the University holiday period. This excess noise is therefore most likely caused by human activity in and around the building.

The data was initially assessed through a plot of residuals and a frequency spectrum, shown in figure 6.2. The first noticeable artefact in the spectrum, seen in both the autocollimator readout data and Iliad, was two clear peaks at frequencies around 10^{-5}Hz. It was expected that this spurious signal was due to environmental coupling however no correlation was found at this frequency with either the tilt data or temperature. We fit the $\delta G/G_0$ amplitudes to a sidereal and half-sidereal sinusoid

$$\frac{\delta G}{G_0} \approx \epsilon + B\sin(\omega_{24}t) + C\cos(\omega_{24}t) + D\sin(\omega_{12}t) + E\cos(\omega_{12}t), \tag{6.1}$$

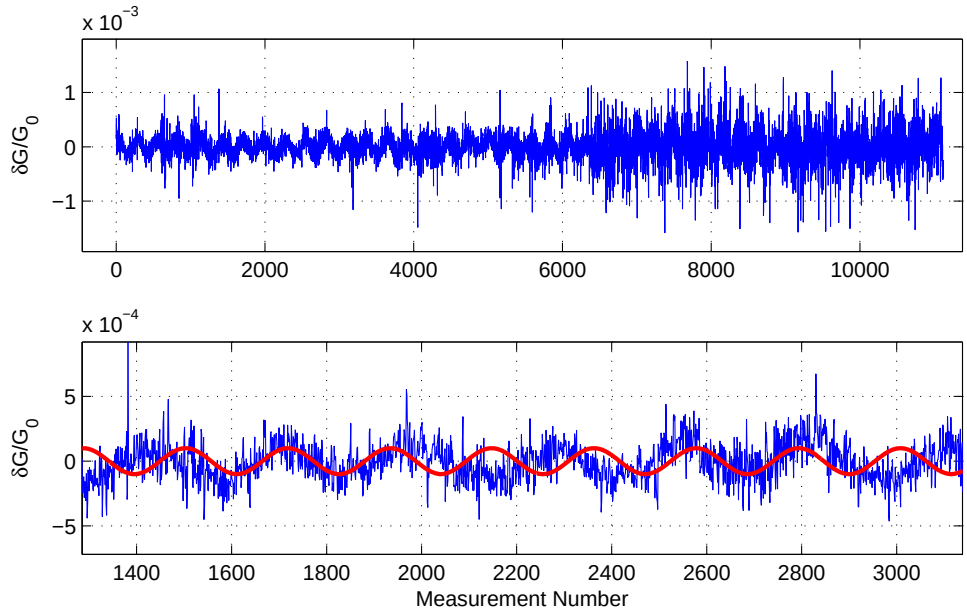

Figure 6.1: $\delta G/G_0$ amplitudes of autocollimator data. Top: full 55 day data set, bottom: Approximately 1500 data points and a dummy sidereal fit (red) for comparison. Error bars removed for visual purposes.

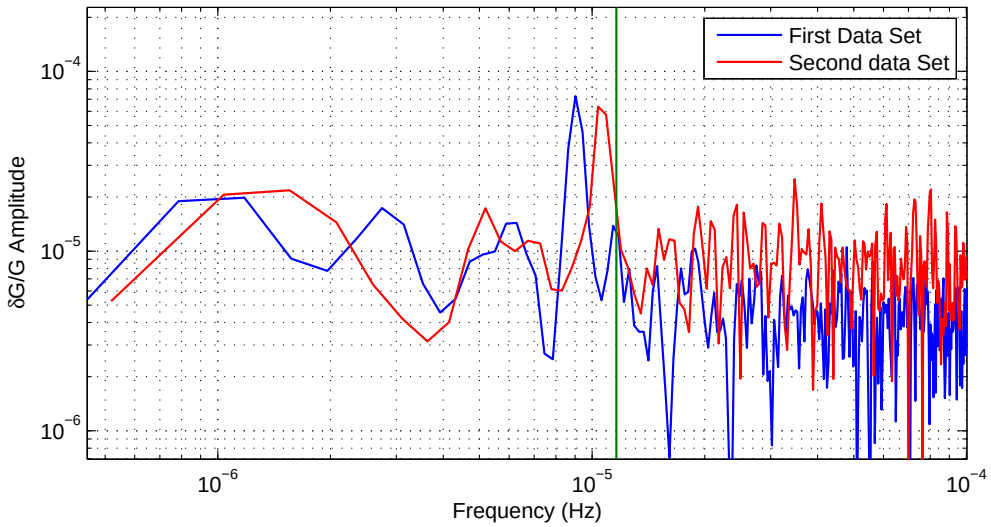

Figure 6.2: Spectrum of torque amplitude for each data set individually. Green line is the position of the sidereal frequency.

Parameter	Result
$\frac{\delta G}{G_0} \approx \epsilon$	-0.0005 ± 3.8 $\times 10^{-6}$
$\frac{\delta G_{24}(sin)}{G_0} \approx$ B	-1.0 ± 5.4 $\times 10^{-6}$
$\frac{\delta G_{24}(cos)}{G_0} \approx$ C	3.3 ± 5.4 $\times 10^{-6}$
$\frac{\delta G_{12}(cos)}{G_0} \approx$ D	1.7 ± 5.4 $\times 10^{-6}$
$\frac{\delta G_{12}(cos)}{G_0} \approx$ E	2.8 ± 5.4 $\times 10^{-6}$

Table 6.1: Fit coefficients for sidereal signal. Errors reported include those from both statistical and systematic uncertainties

where (B, C),(D, E) are the sine and cosine amplitudes from the sidereal and half-sidereal fit. The results of this fit confirm null values, within our level of uncertainty, for both the sidereal and half-sidereal signal and are given in table 6.

The $\delta G/G_0$ value can be used to set limits on the $\bar{a}_J^\omega$ SME parameters, equation 1.3, re-written here without the orbital term since we are only interested in the sidereal term

$$\frac{\delta \mathbf{G}}{G} \simeq -2\alpha \left(\sum_w \frac{N_w^T \overline{a}_J^w}{M_T} + \sum_w \frac{N_w^S \overline{a}_J^w}{M_S} \right) \left(\beta_L \left(-sin\omega_\oplus T_\oplus, cos\omega_\oplus T_\oplus \right) \right). \tag{6.2}$$

The first experimental data point, referenced as time zero, was at 00:10 on 21st December 2011, approximately 285 days since the sun-centred T_0, i.e. the vernal equinox in 2011, 20th March at 23:21. The definition of $T_\oplus$, as given in [19], is the time at which the Earth's y axis coincides with the sun-centred Y axis which at the vernal equinox is equal to T_0. However each day there is a lag of approximately 4 minutes, the difference between a sidereal and solar day. Thus on 21st December 2011 the time $T_\oplus$ was at 04:02 giving a phase shift between our experimental start time and the defined start time of -1.02 radians. Equation 6.2 can be expanded separating out the fermions as

$$\frac{\delta G}{G} \simeq -4\alpha\beta_L \frac{N_n}{M_{atom}} \left[\left(\bar{a}_X^n + \frac{N_p}{N_n}\bar{a}_X^p + \frac{N_e}{N_n}\bar{a}_X^e \right) \sin\omega_\oplus T_\oplus \right. \\ \left. - \left(\bar{a}_Y^n + \frac{N_p}{N_n}\bar{a}_Y^p + \frac{N_e}{N_n}\bar{a}_Y^e \right) \cos\omega_\oplus T_\oplus \right], \tag{6.3}$$

where $_L$ as before is the rotational speed of the Earth at our latitude, 52°N, N_w is the number of particles of particular species and M_{atom} is the mass of a copper atom, ignoring the Te within our test mass since its mass is negligible. The addition of the phase shift can be considered using standard trigonometric identities. Let

$$S = a\cos(\omega_\oplus t) + b\sin(\omega_\oplus t), \tag{6.4}$$

where a and b are the sidereal signals obtained from experimental data. The signal in the Sun-centred reference frame is

$$S' = a'\cos(\omega_\oplus T_\oplus) + b'\sin(\omega_\oplus T_\oplus) = a'\cos(\omega_\oplus t + \Phi) + b\sin(\omega_\oplus t + \psi) \tag{6.5}$$

$$S' = a'(\cos(\omega_\oplus t)\cos(\psi) - \sin(\omega_\oplus t)\sin(\psi) + b'(\sin(\omega_\oplus t)\cos(\psi) + \cos(\omega_\oplus t)\sin(\psi)). \tag{6.6}$$

and can be equated to the experimental signal

$$a' = \frac{a(\cos(\psi)) - b(\sin(\psi))}{(\cos(\psi)^2 + \sin(\psi)^2)} \tag{6.7}$$

$$a' = \frac{a(\sin(\psi)) + b(\cos(\psi))}{(\cos(\psi)^2 + \sin(\psi)^2)}. \tag{6.8}$$

With our experimental results we obtain

$$
\begin{aligned}
|\alpha\,[\bar{a}_X^n + 0.83(\bar{a}_X^p + \bar{a}_X^e)]\,| &\leq 1.3 \text{ GeV}, \\
|\alpha\,[\bar{a}_Y^n + 0.83(\bar{a}_Y^p + \bar{a}_Y^e)]\,| &\leq 1.6 \text{ GeV}.
\end{aligned} \tag{6.9}
$$

This limit is higher than that achieved in our previous experimental run as presented in [21] which gave constraints that were several times smaller. However it must be noted that the current results were obtained from 55 days worth of data as opposed to almost 80 days for the previous set and in a noisier environment as confirmed by a comparison of torsion balance spectra. Our current data also contained the spurious signals around 10^{-5}Hz which are yet to be understood.

Chapter 7

Conclusion and Discussion

7.1 $\delta G/G$ Results

Although we have rejected any sidereal variation of magnitude greater than 5×10^{-6} the origin of the two spurious signals were still unknown. For the current experiment we used two source masses positioned along the short-axis of the optical bench. We therefore considered the effect of rotating these masses so they would oscillate around the long-axis of the table which was tilt controlled by the piezo device. There was no discernible difference between a 5 day run with the source masses in this position against a previous 5 day run with the 10^{-5}Hz signal still appearing in the data. The source of the signal was also not an aliasing effect since changing the modulation period of the masses to 1000 seconds and filtering out the pendulum resonance did not eliminate the signal. The difference in frequencies of the two peaks in the spectrum is also peculiar suggesting a shift in the periodicity between December and February. During the experimental run there were major building works being carried out a few hundred metres away however the signal was still apparent during the Christmas and new year break where building works would have stopped. We have therefore yet to determine the origin of this spurious signal.

A possible source of noise in the system could be due to non perfect movement of the

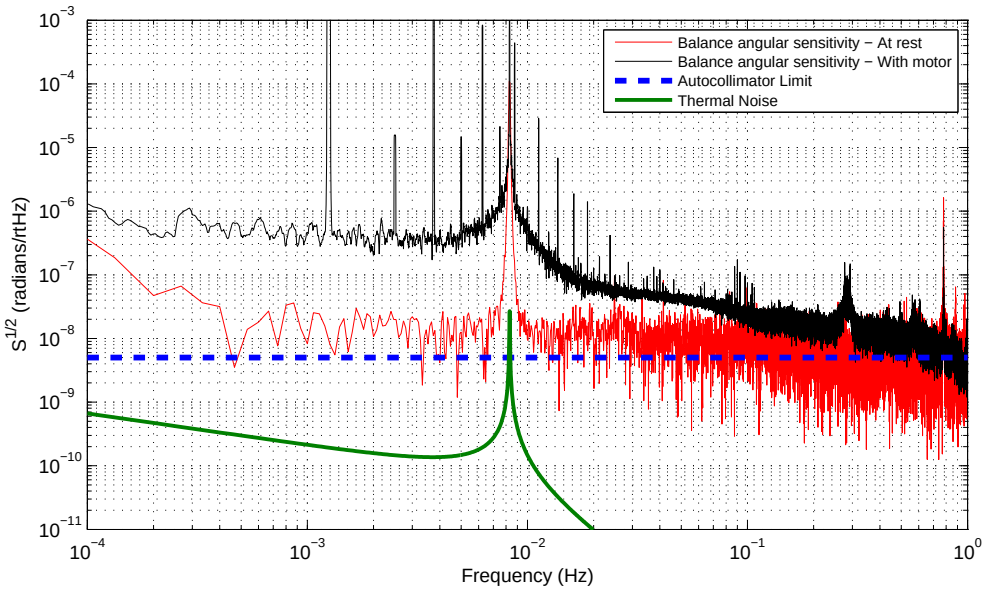

Figure 7.1: Torsion Balance angular sensitivity when motor running (red) and when it was not (black). The noise at the 800 second signal frequency is more than an order of magnitude higher when the motor is modulating the source masses.

source masses. Currently these are being moved by a stepper motor driven by a computer programme. There is no absolute measurement of the source mass position and rather only a reading of where it has been instructed to move to by the computer. Subtle effects within the motor system maybe cause the source masses to move to a position different to that which is expected and for which our data analysis relies on. As an estimate moving the motor by 1° resulted in a change in torque of approximately $1\pm0.8 \times 10^{-11}$Nm. Thus a future step to upgrade the apparatus would be to install a sensor which independently monitors the position of the source masses. Secondly the motor induced noise into the balance of more than an order of magnitude as shown in figure 7.1. Any future experiments would benefit from a quieter motor system to drive the source masses.

7.2 Summary

This thesis has described the development of a laboratory apparatus used to undertake experiments searching for weak interactions which could give insights into the validity of new theoretical frameworks. The first experiment undertaken in this new setup was to search for variations in the Newtonian Gravitational constant which obtained a null result for a sidereal signal at the few ppm level. Along with a previous similar test set the first limits on one of the parameters of the Standard Model Extension.

The work carried out on assembling and characterising a new interferometric readout has also been reported. This readout, Iliad, which can measure angles accurately to $\pm$ 1°, is also immune to orthogonal tilts and thus is ideal for use in a torsion balance system. Its current measured sensitivity, 5×10^{-11} radians/$\sqrt{Hz}$ between 10^{-1}Hz and 10Hz, is more than an order of magnitude better than the current state of the art autocollimator device and its compactness, an overall cube shape measuring about 5cm^3 in volume, allows it to be fitted inside the vacuum system giving it immunity from environmental noise that affects the autocollimator.

Finally the design and manufacture of a new spin test mass has been described. Using a nested arrangement of rare-earth magnets it has been shown that the external magnetic field can be compensated while still keeping a net spin moment. These test masses, although not complete at the time of writing, have been designed so they can directly replace the current CuTe test masses and new spin-coupling experiments can be undertaken. The number of polarised electrons per kilogram in this design equals that used by Heckel et al. [6, 49] to achieve the best current limits on some of the spin interactions. With the use of a torsion strip our balance can potentially carry 50 times more spin than on The University of Washington design [6, 49]. Although there is much further work to be carried out on the torsion balance apparatus to reduce the noise and establish the origin of spurious signals, and on the test masses to calibrate and prepare them for installation

into the torsion balance the feasibility of running new and exciting experiments in our laboratory has been shown.

References

[1] T.J. Quinn et al. A New Determination of G Using Two Methods. *Phys. Rev. Lett.*, 87(11):111101, 2001.

[2] V. A. Kostelecký and J. Tasson. Matter gravity couplings and Lorentz violation. *Phys. Rev. D*, 83:016013, 2011.

[3] Q.G. Bailey and V.A. Kostelecký. Signals for Lorentz violation in post-newtonian gravity. *Phys. Rev. D*, 74:045001, 2006.

[4] K.H. Buschow and F.R. De Boer. *Physics of Magnetism and Magnetic Materials*. Kluwer Academic Publishers, New York, 2004.

[5] C. Kittel. *Introduction to Solid State Physics*. John Wiley and Sons, London, seventh edition, 1995.

[6] B.R. Heckel et al. Preferred-frame and CP-violation tests with polarized electrons. *Phys. Rev. D*, 78:092006, Nov 2008.

[7] ANSYS$^{(TM)}$. `http://www.ansys.com`.

[8] P. Larson et al. Calculation of magnetic anisotropy energy in $SmCo_5$. *Phys. Rev. B*, 67:214405, 2003.

[9] Magnet-Physik GmbH USA. Indianapolis, Indiana, US.

[10] G.T. Gillies and R.C. Ritter. Torsion balances, torsion pendulums, and related devices. *Rev. Sci. Instrum.*, 64:283, 1993.

[11] E.G. Adelberger et al. Torsion balance experiments: A low-energy frontier of particle physics. *Prog. Part. Nucl. Phys.*, 62:102, 2009.

[12] V.A. Kostelecký and S. Samuel. Spontaneous breaking of lorentz symmetry in string

theory. *Phys. Rev. D*, 39:683, 1989.

[13] V.A. Kostelecký and R. Potting. CPT and strings. *Nucl. Phys. B.*, 359:545, 1991.

[14] V.A. Kostelecký and D. Colloday. Lorentz-violating extension of the standard model. *Phys. Rev. D*, 58:116002, 1998.

[15] V.A.Kostelecký and N. Russell. Data tables for Lorentz and CPT violation. *Rev. Mod. Phys.*, 83:11, 2011.

[16] J.M. Brown et al. New limit on lorentz- and cpt-violating neutron spin interactions. *Phys. Rev. Lett.*, 105(15):151604, 2010.

[17] M.A. Hohensee et al. Improved constraints on isotropic shift and anisotropies of the speed of light using rotating cryogenic sapphire oscillators. *Phys. Rev. D*, 82(7):076001, 2010.

[18] V.A. Kostelecký. Private Communication.

[19] V.A. Kostelecký and M. Mewes. Signals for Lorentz violation in electrodynamics. *Phys. Rev. D*, 66:056005, 2002.

[20] L. Carbone et al. A Torsion Balance Search for Temporal Variations in the Newtonian Constant. In R.T. Jantzen T. Damour and eds. R. Ruffini, editors, *Proceedings of the Twelfth Marcel Grossmann Meeting on General Relativity*. World Scientific, Singapore, 2010.

[21] H. Panjwani et al. Laboratory searches for preferred frame effects: Ongoing work and results at birmingham. In V. Alan Kostelecký ed., editor, *Proceedings of the Fifth Meeting on CPT and Lorentz Symmetry*. World Scientific, Singapore, 2010.

[22] L-S Hou et al. Test of cosmic spatial isotropy for polarized electrons using a rotatable torsion balance. *Phys. Rev. Lett.*, 90:201101, 2003.

[23] W-T. Ni. Searches for the role of spin and polarization in gravity. *Rep. Prog. Phys*, 73:056901, 2010.

[24] J.E. Moody and F. Wilczek. New macroscopic forces? *Phys. Rev. D*, 30:130, 1984.

[25] B.A. Dobrescu and I. Mocioiu. Spin-dependent macroscopic forces from new particle exchange. *J. High Energy Phys.*, 5:0611, 2006.

[26] R.C. Ritter et al. Search for anomalous spin-dependent forces with a polarized-mass torsion pendulum. *Phys. Rev. Lett.*, 70:701, 1993.

[27] W-T. Ni et al. Search for an axionlike spin coupling using a paramagnetic salt with a dc squid. *Phys. Rev. Lett.*, 82:2439, 1999.

[28] G.D. Hammond et al. New constraints on short-range forces coupling mass to intrinsic spin. *Phys. Rev. Lett.*, 98:081101, 2007.

[29] G.D. Hammond et al. Development of a second generation torsion balance based on a spherical superconducting suspension. *Rev. Sci. Instrum.*, 79(2):025103, 2008.

[30] P. Saulson. Thermal noise in mechanical experiments. *Phys. Rev. D*, 42(8):2437, 1990.

[31] K. Kuroda. Anelasticity in G experiments. *Meas. Sci. Technol.*, 10:435, 1999.

[32] C. Zenar. Internal friction in solids. *Phys. Rev.*, 53:90, 1938.

[33] C.C. Speake et al. Experiment and theory in anelasticity. *Meas. Sci. Technol.*, 10:430, 1999.

[34] A.L. Kimball and D.E. Lovell. Internal friction in solids. *Phys. Rev.*, 30:948, 1927.

[35] S.J. Richman et al. Preliminary determination of G using BIPM torsion strip balance. *Meas. Sci. Technol.*, 10:430, 1999.

[36] T.J. Quinn et al. Novel torsion balance for the measurement of the Newtonian gravitational constant. *Metrologia*, 34:245, 1997.

[37] T.J. Quinn et al. The restoring torque and damping in wide Cu-Be torsion strips. *Phys. Lett. A*, 238:36, 1997.

[38] P.R. Saulson. *Fundamentals of interferometric gravitational wave detectors*. World Scientific Publishing Co, Singapore, 1994.

[39] T.J. Quinn et al. Stress-dependent damping in Cu-Be torsion and flexure suspensions at stresses up to 1.1 GPa. *Phys. Lett. A*, 197(3):197, 1995.

[40] Möller-Wedel Optical. `http://www.moeller-wedel-optical.com/`.

[41] Julabo. F33-EH. `http://www.julabo.de/`.

[42] B. Odom et al. New measurement of the electron magnetic moment using a one-electron quantum cyclotron. *Phys. Rev. Lett.*, 97(3), 2006.

[43] J.M.D. Coey. *Magnetism and Magnetic Materials*. Cambridge University Press, Cambridge, 2010.

[44] M. McCaig. *Permanent magnets in theory and in practice*. Pentech, London, second edition, 1987.

[45] K.J Strnat. Modern Permanent Magnets for Applications in Electro-Technology. *Proceedings of the IEEE*, 78(6):923, 1990.

[46] Material Technologies Inc. Singapore.

[47] P. Phillips and D. Woolum. A test of Lorentz invariance using a torsion pendulum. *Nuovo. Cimento.*, 64B:28, 1969.

[48] P. Phillips. Test of Spatial Isotropy Using a Cryogenic Torsion Balance. *Phys. Rev.*

Lett., 59(15):1784, 1987.

[49] C.E. Cramer. *A Torsion Balance Search for Spin-Coupled Forces.* PhD thesis, University of Washington, 2007.

[50] L.C. Carbone et al. Design of high-density electron spin-polarized test masses. *Class. Quantum Grav.*, 26, 2009.

[51] J.D. Jackson. *Classical Electrodynamics.* Wiley, New York; London, second edition, 1975.

[52] J.B. Bronzan. The magnetic scalar potential. *American Journal of Physics*, 39:1359, 1971.

[53] C.G. Gray. Magnetic multipole expantion using the scalar potential. *American Journal of Physics*, 47(5):457, 1979.

[54] D.C. Meeker. Finite element method magnetics (femm), Version 4.2 (23-05-2008). `http://femm.foster-miller.net/wiki`.

[55] First4Mag. `http://www.first4magnets.co.uk`.

[56] MagsUK. `http://www.magnetsukonline.co.uk`.

[57] Magnetic Applications LTD. `http://www.magnetapplications.com`.

[58] Quadrant Magnetics LLC. Louisville, Kentucky, US.

[59] F.L. Pratt et al. Ferromagnetism with zero intrinsic magnetization: μSR on Gd-doped $SmAl_2$. *Physica B*, 34:374, 2006.

[60] H. Adachi and H. Ino. A ferromagnet having no net magnetic moment. *Nature*, 401:148, 1999.

[61] K.J. Strnat and A. Tauber. Internal temperature compensation of rare earth-cobalt

permanent magnets for microwave devices by adding heavy lanthanides. *Journal of the Less-Common Metals*, 93:269, 1983.

[62] Mike Guthrie. Quadrant Magnetics LLC, Private Communication.

[63] P. Tils et al. Crystal and exchange fields in $SmCo_5$ studied by inelastic neutron scattering. *Journal of Alloys and Compounds*, 289:28, 1999.

[64] A. Koizumi et al. X-ray magnetic Compton-profile measurements on $SmCo_5$ by using pulsed high magnetic field. *J. Phys. Soc. Japan*, 66(2):318, 1997.

[65] D. Givord et al. Temperature dependence of the samarium magnetic form factor in $SmCo_5$. *J. App. Phys.*, 50(3):2008, 1979.

[66] J. Schweizer et al. Polarised neutron study of the RCo_5 intermetallic compounds: I. the cobalt magnetisation in YCo_5. *J. Phys. F: Metal Phys.*, 10:2799, 1980.

[67] D. Givord et al. Different contributions of the two cobalt sites to the magnetocrystalline anisotropy of YCo_5 and related compounds. *IEEE Transactions on Magnetics*, Mag-12(6):1000, 1976.

[68] L. Nordstöm et al. Calculation of orbital magnetism and magnetocrystalline anisotropy energy in YCo_5. *J. Phys. Condens. Matter*, 4:3261, 1992.

[69] H. Yoshie et al. Nuclear magnetic resonance of RCo_5. iii. R=Ce and Sm. *J. Phys. Soc. Japan*, 57:2525, 1988.

[70] D. Givord et al. Magnetic properties of Y_2Fe_14B and Nd_2Fe_14B single crystals. *Solid State Communications*, 51(11):857–860, 1984.

[71] K. Tokuhara et al. Magnetization and torque measurements on $Nd_2Fe_{14}B$ single crystals. *Solid State Communications*, 56(4):333–336, 1985.

[72] D. Givord et al. Polarized neutron study of the compounds Y_2Fe_14B and Nd_2Fe_14B.

J. Appl. Phys, 57(1), 1985.

[73] H. Onodera et al. Mssbauer study of the intermetallic compound $Nd_2Fe_{14}B$. II. Temperature dependence and spin reorientation. *Journal of Magnetism and Magnetic Materials*, 68(1):15, 1987.

[74] N.C. Koon et al. Magnetic properties of $R_2Fe_{14}B$ single crystals. *J. Appl. Phys*, 57(1), 1985.

[75] D. Givord et al. Private Communication.

[76] M. Sagawa et al. Permanent magnet materials based on the rare earth-iron-boron tetragonal compounds. *IEEE Trans. Mag.*, Mag-20(5):1584, 1984.

[77] S. Hirosawa et al. Magnetisation and magnetic anisotropy of $R_2Fe_{14}B$ measured on single crystals. *J. App. Phys.*, 59(3):873, 1986.

[78] J.F. Herbst et al. Relationships between crystal structure and magnetic properties in $Nd_2Fe_{14}B$. *Phys. Rev. B*, 29:4176, 1984.

[79] J. Chaboy et al. 57Fe Mössbauer and x-ray magnetic circular dichroism study of magnetic compensation of the rare-earth sublattice in Nd_2-xHox$Fe_{14}B$ compounds. *Phys. Rev. B*, 79:134408, 2007.

[80] L.M Garcia et al. Soft x-ray magnetic circular dichroism investigation of the spin reorientation transition in $Nd_2Fe_{14}B$. *J. Appl. Phys.*, 87:6567, 2000.

[81] R.A Reck and D.L. Fry. Orbital and spin magnetization in Fe-Co, Fe-Ni and Ni-Co. *Phys. Rev.*, 184(2), 1969.

[82] L.M Garcia, J. Chaboy, and F.Bartolome. Orbital magnetic moment instability at the spin reorientation transition of $Nd_2Fe_{14}B$. *Phys. Rev. Lett.*, 85(2), 2000.

[83] E. R. Peck and S. Wendell Obetz. Wavelength or Length Measurement by Reversible

Fringe Counting. *J. Opt. Soc. Am.*, 43(6):505, 1953.

[84] M.J. Downs and K.W. Raines. Beam-splitter coatings for producing phase quadrature interferometer outputs. *J. Mod. Opt.*, 25(7), 1978.

[85] V. Greco et al. Multiphase homodyne interferometry: analysis of some error sources. *App. Opt.*, 34(13):2207, 1995.

[86] E.R. Peck. Theory of the cube-corner interferometer. *J. Opt. Soc. Am*, 38:1015, 1948.

[87] J.J. Snyder. Paraxial ray analysis of a cat's-eye retroreflector. *Appl. Opt.*, 14(8):1825, 1975.

[88] M.L. Biermann et al. Design and analysis of a diffraction-limited cat's eye retroreflector. *Opt. Eng.*, 41:1655, 2002.

[89] R.F. Chang et al. Far-field diffraction pattern for corner reflectors with complex reflection coefficients. *J. Opt. Soc. Am.*, 61(4):432, 1971.

[90] H.D. Eckhardt. Simple model of corner reflector phenomena. *App. Opt*, 10(1):1559, 1971.

[91] M.A. Player. Polarization properties of a cube-corner reflector. *J. Mod. Opt*, 35:1813, 1988.

[92] F.E. Peña-Arellano and C.C. Speake. Mirror tilt immunity interferometry with a cat's eye retroreflector. *App. Opt.*, 50(7):981, 2011.

[93] N. Bobroff. Recent advances in displacement measuring interferometry. *Meas. Sci. Tech.*, 4:907, 1953.

[94] F.E. Peña-Arellano et al. An interferometer for measuring angular motion. In Preparation.

[95] C.C. Speake and S.M. Aston. An interferometric seonsor for satellite drag-free control. *Class. Quantum Grav.*, 22:S269, 2005.

[96] F.E. Peña-Arellano. *Characterisation of polarization homodyne interferometers.* PhD thesis, University of Birmingham, 2008.

[97] Laser 2000. `http://http://www.laser2000.co.uk/`.

[98] Thorlabs Inc. `http://www.thorlabs.com`.

[99] Norland Products. `http://www.norlandprod.com/adhesives/noa`$_2$`065.`*html*.

[100] S.M. Aston. *Optical Read-out Techniques for the Control of Test-masses in Gravitational Wave Observatories.* PhD thesis, University of Birmingham, 2011.

[101] R. Halir and J. Flusser. Numerically stable direct least squares fitting of ellipses. In *Proceedings of the 6th International Conference in Central Europe on Computer Graphics and Visualization.* WSCG, 1998.

[102] S.B. Alexander. *Optical Communication Receiver Design.* SPIE - The International Society for Optical Engineering, Washington, 1997.

[103] D.K. Owens and R. Weiss. Measurement of the phase fluctuations in a He-Ne Zeeman laser. *Rev. Sci. Instrum.*, 45:1060, 1974.

[104] L. Carbone et al. Upper limits to surface-force disturbances on lisa proof masses and the possibility of observing galactic binaries. *Phys. Rev. D*, 75:042001, 2007.

[105] L. Ferraioli et al. Discrete derivative estimation in lisa pathfinder data reduction. *Class. Quantum Grav.*, 26:094013, 2009.

[106] W.H. Press et al. *Numerical Recipes: The Art of Scientific Computing.* Cambridge University Press, Cambridge, 1986.

Appendix A

Magnetic Properties for $SmCo_5$ and Nd_2Fe_14B final pieces

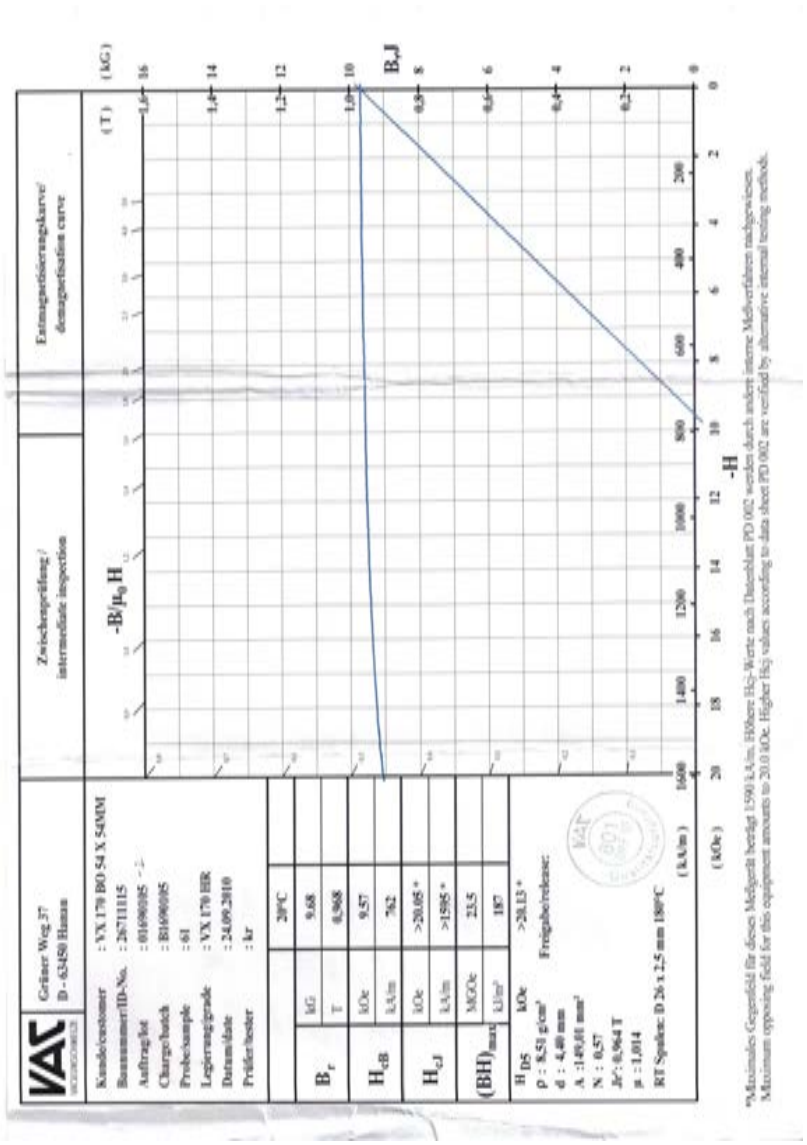

Figure A.1: Demagnetisation Curve for $SmCo_5$ material used for the inner sphere.

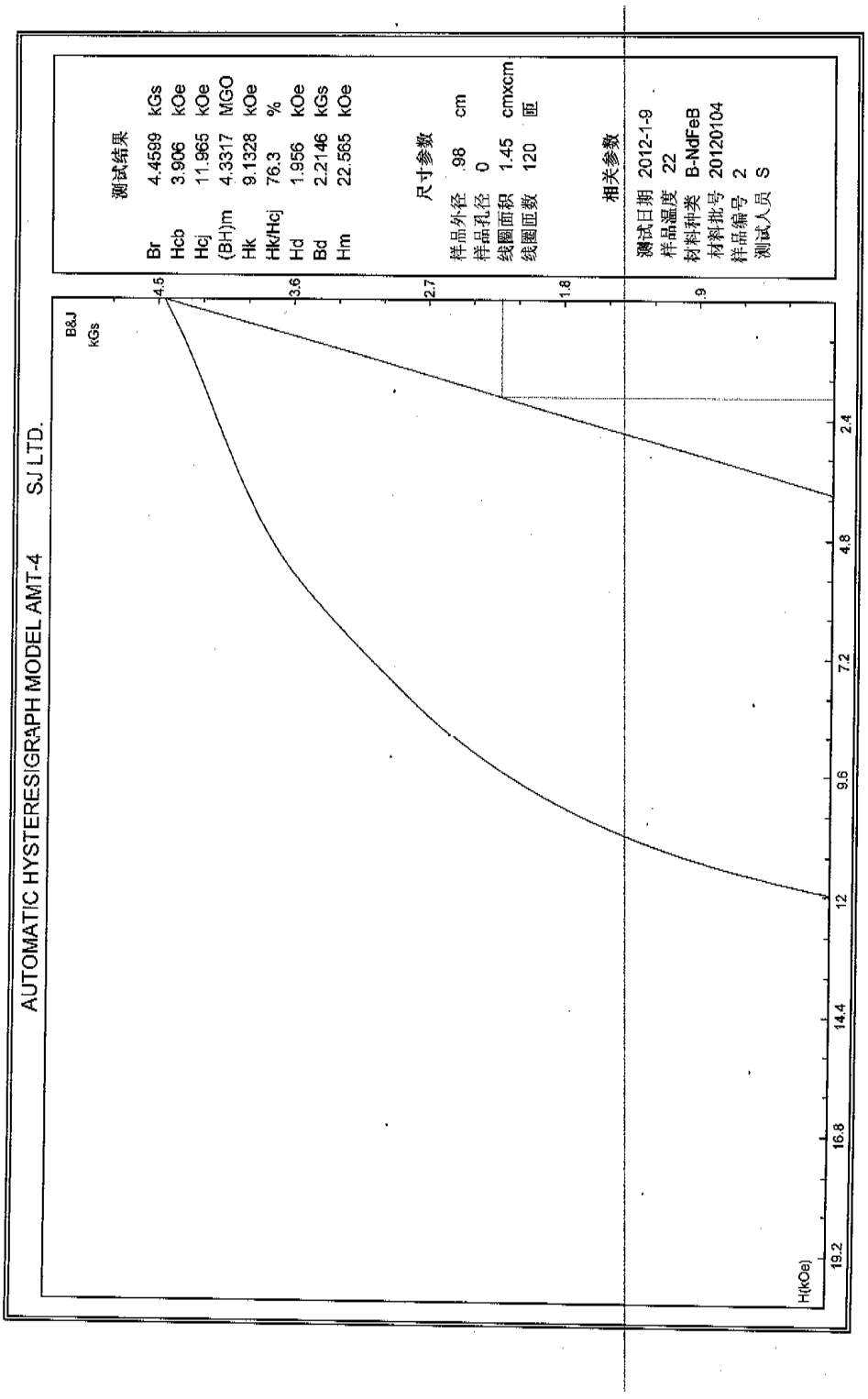

Figure A.2: Demagnetisation Curve for bonded Nd_2Fe_14B material, MQP-14-12, used for the outer shells.

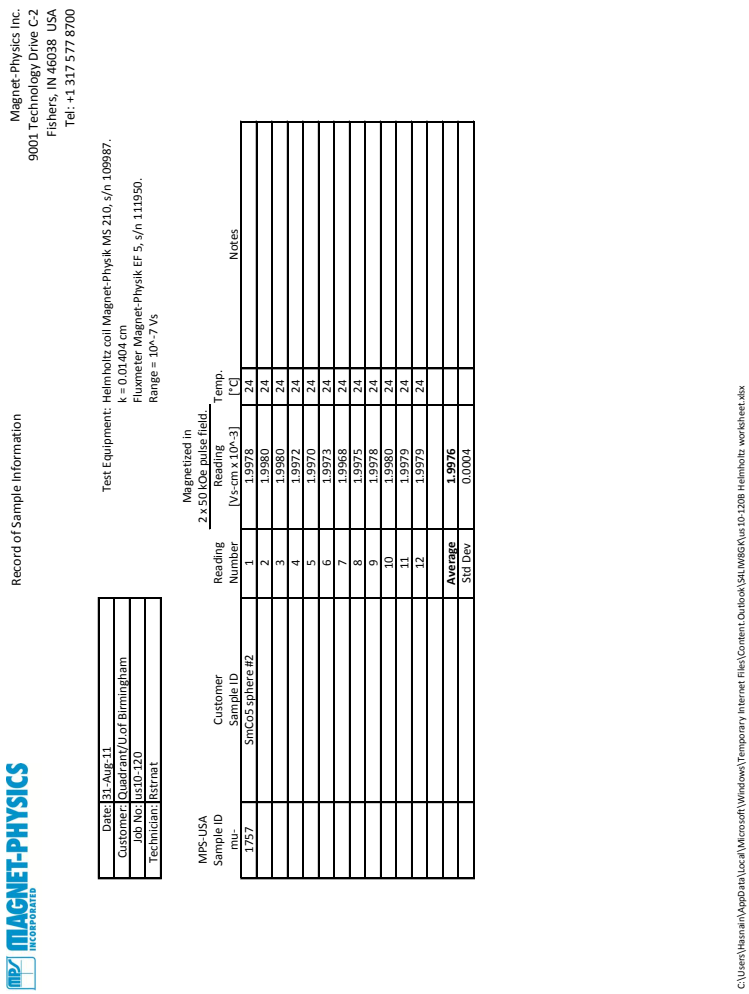

MAGNET-PHYSICS INCORPORATED

Record of Sample Information

Magnet-Physics Inc.
9001 Technology Drive C-2
Fishers, IN 46038 USA
Tel: +1 317 577 8700

Date:	31-Aug-11
Customer:	Quadrant/U.of Birmingham
Job No:	us10-120
Technician:	Rstrnat

Test Equipment: Helmholtz coil Magnet-Physik MS 210, s/n 109987.
k = 0.01404 cm
Fluxmeter Magnet-Physik EF 5, s/n 111950.
Range = 10^-7 Vs

MPS-USA Sample ID mu-	Customer Sample ID	Reading Number	Magnetized in 2 x 50 kOe pulse field. Reading [Vs-cm x 10^-3]	Temp. [°C]	Notes
1757	SmCo5 sphere #2	1	1.9978	24	
		2	1.9980	24	
		3	1.9980	24	
		4	1.9972	24	
		5	1.9970	24	
		6	1.9973	24	
		7	1.9968	24	
		8	1.9975	24	
		9	1.9978	24	
		10	1.9980	24	
		11	1.9979	24	
		12	1.9979	24	
		Average	**1.9976**		
		Std Dev	0.0004		

C:\Users\Hasnain\AppData\Local\Microsoft\Windows\Temporary Internet Files\Content.Outlook\34LIW8GK\us-10-120B Helmholtz worksheet.xlsx

Figure A.3: Magnetic Moment measurements of final $SmCo_5$ sphere made by MPUSA[9].

MAGNET-PHYSICS INCORPORATED

Record of Sample Information

Magnet-Physics Inc.
9001 Technology Drive C-2
Fishers, IN 46038 USA
Tel: +1 317 577 8700

Test Equipment:

Helmholtz coil Magnet-Physik MS 210, s/n 109987.
k = 0.01404 cm
Fluxmeter Magnet-Physik EF5, s/n 111950
Range = 10^6 Vs

Date:	30-Mar-12
Customer:	Quadrant
Job No:	us10-120
Technician:	RStrnat

Magnetized in 4 x 50 kOe pulse field.

	MPS-USA Sample ID mu-	Customer Sample ID	Rdg 1 [uVs-cm]	Rdg 2 [uVs-cm]	Rdg 3 [uVs-cm]	Avg. [uVs-cm]	Temp. [°C]	Weight
1	02315	Half sphere #1 N up	1082	1082	1082	**1082**	23	117.14 g
2	02316	Half sphere #2 N up	1081	1081	1081	**1081**	23	116.94 g
3	02317	Half sphere #3 S up	1082	1082	1082	**1082**	23	116.97 g
4	01318	Half sphere #4 S up	1082	1083	1083	**1083**	23	117.08 g
5								
6								
7								
8								
11								
12								
13								
14								
15								
16								
17								
18								
19								
20								

C:\Users\Hasnain\AppData\Local\Microsoft\Windows\Temporary Internet Files\Content.Outlook\34LIW8GK\us-10-120C Quadrant half spheres.xls

Figure A.4: Magnetic Moment measurements of final bonded Nd_2Fe_14B half shells made by MPUSA[9].

Appendix B

CAD Drawings of Iliad mechanical holder

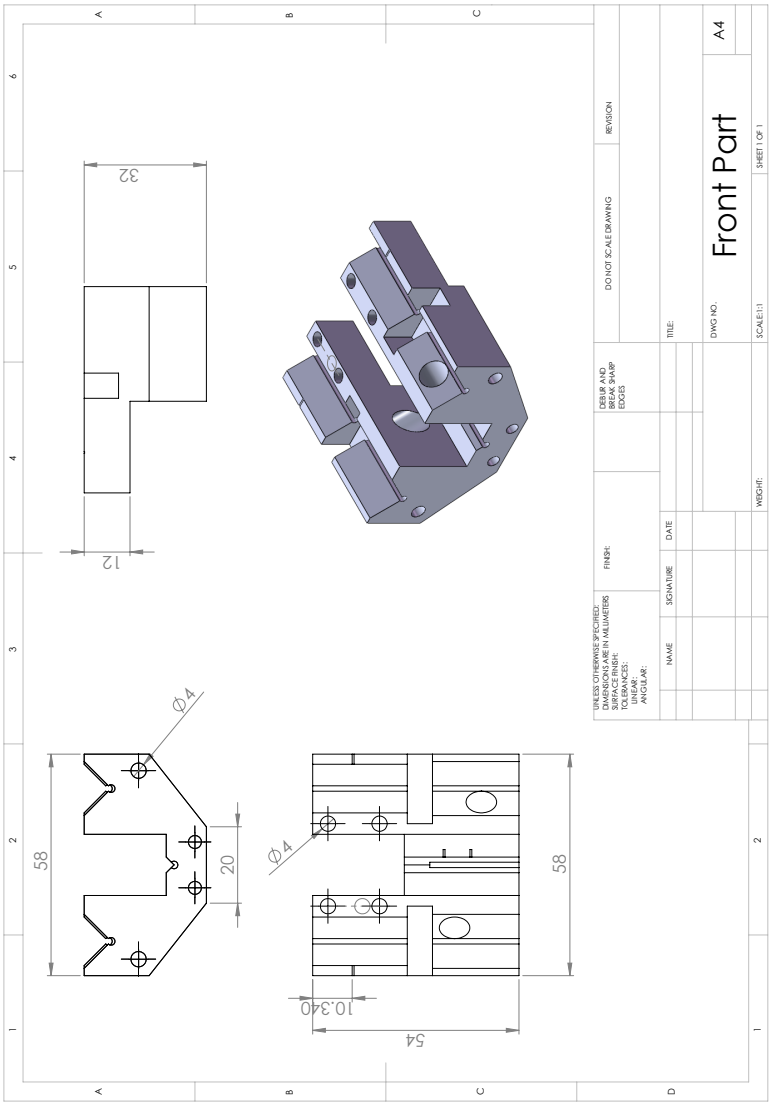

Figure B.1: CAD drawing of front piece housing two 45° beam splitters and cat's eyes.

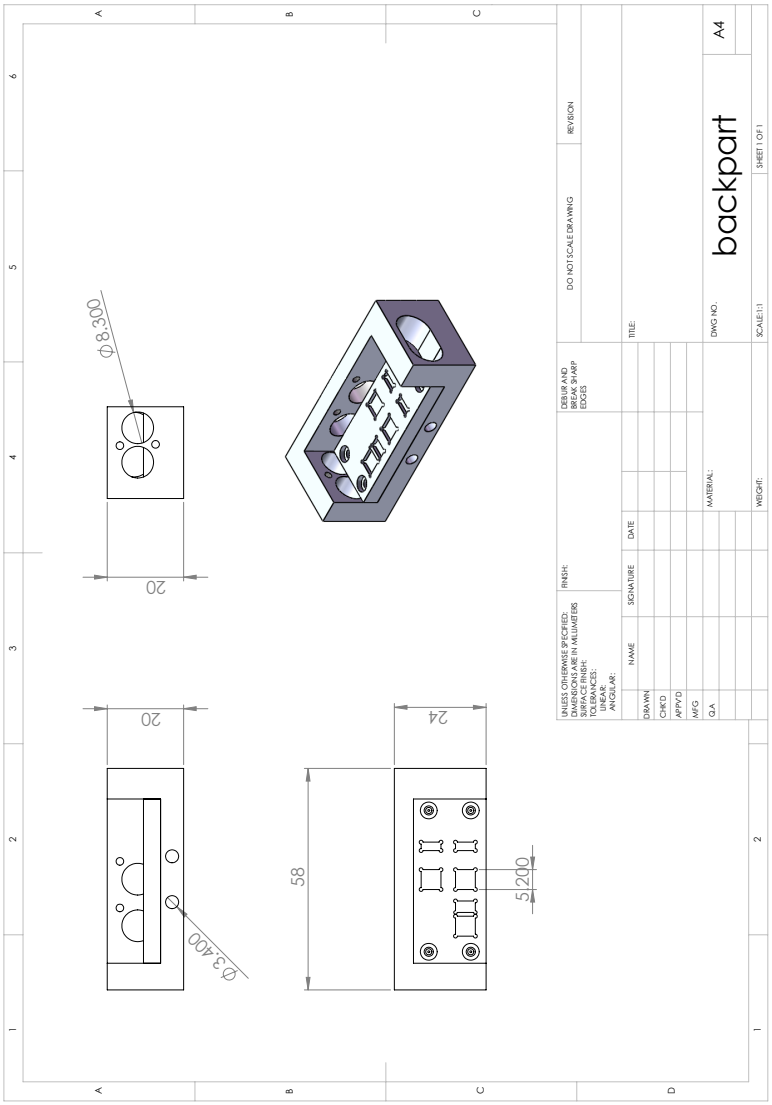

Figure B.2: CAD drawing of back piece housing the interfering optics and the photodiodes. The template with grooves to position optics is a separate piece fixed onto the back part.

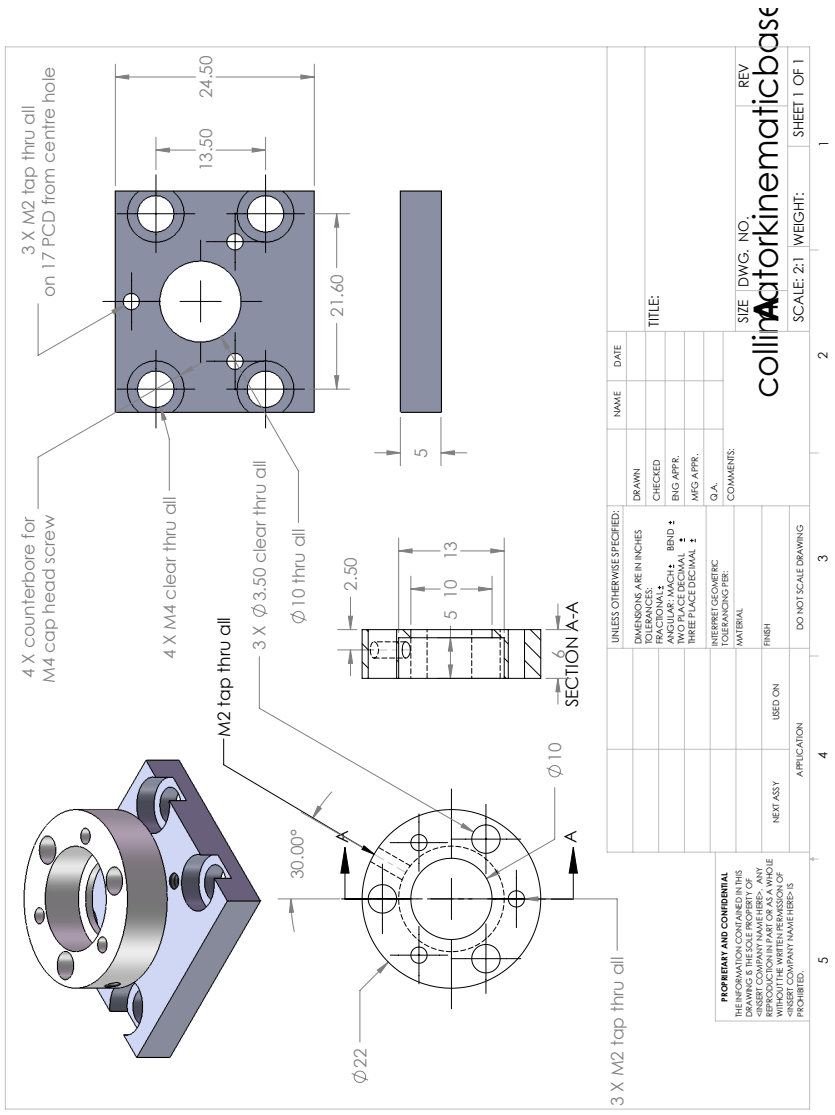

Figure B.3: CAD drawing of collimator kinematic mount which screws onto the top of the front part.